
Wind turbine load dynamics in the context of intermittent atmospheric turbulence

Carl Michael Schwarz

Von der Fakultät für Mathematik und Naturwissenschaften
der Carl von Ossietzky Universität Oldenburg
zur Erlangung des Grades und Titels eines

**DOKTORS DER INGENIEURWISSENSCHAFTEN
DR.-ING.**

angenommene Dissertation

von Herrn Carl Michael Schwarz
geboren am 18.11.1987 in Kiel

Erstgutachter: Prof. Dr. rer. nat. Joachim Peinke
Zweitgutachterin: Prof. Dr.-Ing. Laura Lukassen
Tag der Disputation: 02.06.2020

Contents

Abstract / Zusammenfassung	v
1 Introduction	1
1.1 Intermittency – A missing aspect in wind models?	2
1.2 State of research	3
1.3 Scope of this work	6
2 Fundamentals of the utilized models	7
2.1 Intermittency and wind modeling	7
2.1.1 Introduction to turbulence intermittency	7
2.1.2 Review of common wind models	11
2.1.3 Generation of intermittent wind fields: The CTRW model	13
2.2 Wind turbine modeling	14
2.2.1 Blade-Element/Momentum theory	15
2.2.2 Turbine model specifications	23
2.3 Load analysis	25
2.3.1 Introduction of design load cases	25
2.3.2 Selection of a design load case	25
2.3.3 Fatigue load calculation	28
2.3.4 Selection of load sensors	31
3 Wind field generation	33
3.1 Wind time series	34
3.1.1 One Point (1P) statistics	34
3.1.2 Two Point (2P) statistics	36
3.2 Assembly of wind fields	39
3.2.1 Full correlation and delta correlation	39
3.2.2 Subdivided fully correlated fields	40
3.2.3 Stationary coherent structures	41
4 The intermittency effect for fully correlated wind fields	45
4.1 Equivalent fatigue loads	45
4.2 A closer look at load ranges	51
4.3 Evidence of intermittency in the load signal	54
4.4 Aero-Servo-Elasticity	56

4.5	Summary	62
5	The impact of spatial variability on the intermittency effect	63
5.1	Delta correlated fields	63
5.2	Subdivided fully correlated fields	65
5.3	Stationary coherent structures	70
5.4	Summary	72
6	Conclusions	73
	Bibliography	75
	List of publications	81
	Acknowledgements	83
	Curriculum vitae	85
	Erklärung	87

Abstract

In this work the impact of higher order statistics of wind on wind turbine loads, especially fatigue loads, is discussed.

Non-Gaussian distributed wind velocity increments, which are related to the concept of turbulence intermittency, are the focal point of this thesis. Within this study, synthetic wind fields featuring Gaussian and non-Gaussian increment statistics are generated, utilizing a wind model based on Continuous-Time-Random-Walks. Subsequently, these fields are used as an input in a common wind turbine simulation. The resulting load responses are compared and analyzed with respect to the accumulated fatigue damage. In doing so, an increase in fatigue loading by approx. 5-10% for extreme coherent wind fields and selected load sensors is found. Additionally the dependency of this load enhancement on the coherence of the wind field is discussed. It is demonstrated that the intermittency effect decreases with the coherence.

This work is structured as follows: Firstly a broader introduction into this topic is given. This includes a comprehensive literature review of related works and the state of the current scientific knowledge is discussed. Subsequently, fundamental concepts of turbulence, intermittency, wind modeling, wind turbine simulations and fatigue load calculation are discussed. In doing so, common wind modeling approaches and their implications for higher order wind statistics are described. Afterwards the wind field generation approach is outlined. It is also discussed which conditions need to be met in order for the effect of intermittency to be isolated from other wind field features. The results of wind turbine simulations with these wind fields are presented and discussed. At first the discussion is limited to wind fields with extreme coherence. Here, a clear intermittency effect on fatigue loads is evident. Subsequently, results obtained for wind fields featuring different coherence properties are considered. From these results it becomes clear that the intermittency effect is highly dependent on the coherence of the field. Finally, the conclusions of this work are presented and compared against the previous state of research.

Zusammenfassung

In der vorliegenden Arbeit wird der Einfluss höherer Wind-Statistik auf die Dynamik von Windkraft-Anlagen, speziell Ermüdungslasten, diskutiert.

Dabei liegt der Fokus auf nicht Gauss-verteilten Wind-Geschwindigkeits-Inkrementen, die im Zusammenhang mit der Intermittenz von Turbulenz auftreten. Im Rahmen dieser Arbeit werden synthetische Windfelder mit Gauss'scher und nicht-Gauss'scher Inkrement-Statistik auf Basis eines sog. Continuous-Time-Random-Walk Ansatzes erstellt. Die auf diese Weise generierten Windfelder werden in einer fachüblichen Windturbinen-Simulation prozessiert. Die resultierenden Systemantworten werden verglichen und hinsichtlich der Ermüdungslasten ausgewertet. Für extrem kohärente Windfelder kann auf diese Weise eine erhöhte Ermüdungsbelastung von etwa 5-10% für einige Lastsensoren gezeigt werden. Des Weiteren wird die starke Abhängigkeit dieser Lasterhöhung von der Kohärenz des Windfeldes beleuchtet. Hierbei kann gezeigt werden, dass der Intermittenz-Effekt mit der Kohärenz des Windes abnimmt.

Diese Arbeit ist wie folgt strukturiert: Zunächst wird das Thema genauer eingeführt und abgegrenzt. In einer Literatur-Übersicht werden verwandte Arbeiten beleuchtet und der derzeitige Wissensstand beschrieben. Anschließend werden grundlegende Konzepte von Turbulenz, Intermittenz, Wind-Modellierung, sowie Wind-Turbinen-Simulationen und Ermüdungslast-Berechnungen diskutiert. Dabei werden fachübliche Wind-Modelle diskutiert, die grundsätzlich Gauss'sche Inkrement-Statistik annehmen. Nachfolgend wird die Windfeld-Genese detailliert beschrieben. Dabei wird insbesondere darauf eingegangen, welche Bedingungen die Windfelder erfüllen müssen, um den Effekt der Inkrement-Statistiken von anderen Windfeld-Effekten zu isolieren. Im Folgenden werden die Ergebnisse aus den mit den generierten Windfeldern durchgeführten Simulationen vorgestellt und ausgewertet. Zunächst beschränkt sich die Auswertung auf Ergebnisse, die mit extrem kohärenten Windfeldern gewonnen wurden, in denen ein deutlicher Intermittenz-Effekt auf die Lasten erkennbar wird. Anschließend werden Ergebnisse auf Basis von Windfelder anderer Kohärenzen präsentiert. Aus den Ergebnissen ist ersichtlich, dass der Intermittenz-Effekt stark von der Kohärenz des Windes abhängt. In der abschließenden Zusammenfassung werden die aus dieser Arbeit gewonnenen Erkenntnisse zusammengefasst und in Kontext zum vorherigen Forschungsstand gesetzt.

Nomenclature

Latin symbols

A	Area
a_{ax}	Axial induction factor
a_{tang}	Tangential induction factor
B	Number of blades
c	Chord length
c_p	Power coefficient
D	Rotor diameter; Diffusion parameter in Ornstein-Uhlenbeck process
d_r	Range (variogram parameter)
$E(k)$	Energy spectrum as a function of k
$E[X]$	Expectancy value of X
$F(X)$	Flatness of X
f_s	Sampling frequency
f	Frequency
k	Wave number
L	Spatial distance
u	(Wind) Velocity
u_r	Reference velocity in CTRW model, see [1]
u_η	Kolmogorov velocity scale
u_τ	Wind velocity increment on scale τ
$\langle U \rangle$	Mean velocity
u'	Velocity fluctuations
m	Stress Cycle slope coefficient (germ. Wöhler Exponent)
\dot{m}	Mass flow
N	Number of load cycles
n	Order (e.g. of a Moment)
\tilde{n}	Nugget (variogram parameter)
P	Power
p	Pressure; Probability
Q	Rotor torque
r	Radius, radial position
r_{XX}	Auto-correlation function of X
R	Full blade radius

S_{uu}	Power spectral density of the velocity signal u
S_i	Vector of stress ranges
\hat{S}	Absolute damage accumulation
\tilde{S}	Relative damage contribution
$S(\tau)$	Stress ranges on the scale τ
S_τ^n	Structure function in dependency of time lag τ
S_L^n	Structure function in dependency of spatial distance L
s	Model intrinsic time scale of CTRW model [1]
\tilde{s}	Sill (variogram parameter)
T	Thrust
t	Time
W	Inflow

Greek Symbols

α	Angle of attack; Parameter of Lévy distribution
ε	Energy dissipation
η	Kolmogorov length scale
λ^2	Castaing shape parameter
Γ	Wiener process
$-\gamma$	Drift parameter in Ornstein-Uhlenbeck process
γ	Semi-variance in variogram
$\mu_n(X)$	n -th centralized moment of X
$\mu_n(X)$	n -th standardized moment of X
ρ	Density (of air)
$\sigma(X)$	Standard deviation of X
τ	Time lag value
τ_η	Kolmogorov time scale
ϕ	Flow angle
ζ_n	Scaling exponent for structure functions, see [2]
Ω	Angular frequency of the rotor
ω	Angular velocity

Abbreviations

<i>1P</i>	One Point (statistics)
<i>2P</i>	Two Point (statistics)
<i>ABL</i>	Atmospheric Boundary Layer
<i>AERO</i>	Aerodynamic wind turbine model (no servo-dynamics or elasticity)
<i>AOA</i>	Angle of attack
<i>ASE</i>	Aero-servo-elastic wind turbine model
<i>BEM</i>	Blade Element Momentum (theory)
<i>CFD</i>	Computational Fluid Dynamics
<i>CTRW</i>	Continuous Time Random Walk
<i>DLC</i>	Design Load Case
<i>DNS</i>	Direct Numerical Simulation
<i>DOF</i>	Degree of Freedom
<i>EDC</i>	Extreme Direction Change
<i>ECD</i>	Extreme Coherent gust with Direction change
<i>EFL</i>	Equivalent Fatigue Load
<i>ETM</i>	Extreme Turbulence Model
<i>EWS</i>	Extreme Wind Shear
<i>FINO</i>	Research Platform in the North and Baltic Seas
<i>GROWIAN</i>	German "Large wind turbine" test wind turbine
<i>HCF</i>	High Cycle Fatigue
<i>HF</i>	High Frequent
<i>IEC</i>	International Electrotechnical Commission
<i>K41</i>	Kolmogorov's Theory of Turbulence from 1941 [3]
<i>K62</i>	Kolmogorov's Theory of Turbulence from 1962 [2]
<i>LCF</i>	Low Cycle Fatigue
<i>LF</i>	Low Frequent
<i>LES</i>	Large Eddy Simulation
<i>MF</i>	Medium Frequent
<i>NTM</i>	Normal Turbulence Model
<i>POD</i>	Proper Orthogonal Decomposition
<i>PSD</i>	Power Spectral Density
<i>RANS</i>	Reynolds-Averaged Navier Stokes
<i>RBMOP</i>	Root Bending Moment Out of Plane

<i>RFC</i>	Rain Flow Counting
<i>SN</i>	Stress Cycle (histogram / curve / slope)
<i>TI</i>	Turbulence Intensity
<i>TBMFA</i>	Tower-base Bending Moment Fore-Aft
<i>VAR</i>	Variance
<i>WT</i>	Wind Turbine

Chapter 1

Introduction

In modern energy supply wind energy constitutes an important building block. This statement holds true on a global, continental scale and national scale. The following examples stem from published statistics by Working Group on Renewable Energy Statistics (AGEE-Stat) founded by the department of Federal Ministry for Economic Affairs and Energy (BMWi) [4] and the International Renewable Energy Agency (IRENA) [5]:

As of 2018, a global wind power capacity of more than 500GW has been installed, constituting roughly a quarter of worldwide renewable capacities. Europe commands an installed capacity of roughly 500GW of renewable energy sources, approx. 170GW of which come from wind power. In Germany, the overall energy capacity is approx. 200GW, 113GW of which are renewable with 55.9GW of them being wind energy. In terms of energy production, Germany currently obtains roughly a third of its energy demand from renewable, about 15% from on- and offshore wind.

The main advantages of wind energy are well-known: It constitutes an energy form that does not rely on the emission of greenhouse gases. Facing the man-made climate change, such energy forms are urgently needed. In contrast to fossil energy forms, wind power relies on a quasi-limitless source: Wind systems are driven by pressure gradients stemming for example from thermic effects, which again are caused by solar radiation. Thus, wind is a quasi-limitless source of energy.

However, there is a constant demand to drive prices and increase the economic efficiency of wind energy in order to lower the cost of energy and become more and more competitive with other energy sources. One way towards this aim, is to increase the accuracy of models that are inevitably needed in the design and forecasting of wind turbines or in other words: To decrease the uncertainty in those models. In this study so called ‘wind models’ are in the focus, which are used to represent the dynamics of the wind. Wind is a highly complex system whose behavior needs to be represented as complete as possible in order to ensure a safe design.

More specifically, this work focuses on a specific aspect of wind, namely the intermittency of turbulence, which is not considered in common wind models. Whether or not intermittency should be considered in the design process of wind turbines and be included in wind models is unknown and the main goal of this work. A more detailed introduction into this problem is given in Sec. 1.1.

This issue has been addressed by other studies which are reviewed in Sec. 1.2. However

these studies leave some open questions and are partly in contradiction with one another. Therefore, this work aims to answer the most important open questions and add new aspects to the discussion. The outline and the specific contribution of this work are presented in Sec. 1.3.

1.1 Intermittency – A missing aspect in wind models?

So called wind models are used to represent the dynamics of wind in both technical and economic predictions about wind turbines. In wind modeling, one has to distinguish between different aspects of wind dynamics: For instance, the distribution of mean wind speeds, which are typically averaged over ten minutes, a wind distribution model is commonly used. Commonly, this is done with a Weibull distribution. In order to resolve the wind dynamics on time scales $< 10\text{min}$ other models are commonly used and proposed by guidelines such as the IEC 61400 [6]. They represent the fluctuations of atmospheric turbulence. This work focuses on this latter type of wind models.

Turbulence in general constitute an obstacle: Due to its immense complexity no fully comprehensive model exists that includes all of its dynamics. For this reason, modeling efforts often focus on specific properties of wind dynamics and resemble them. Common models focus on reproducing the spectral properties of the wind velocity fluctuations. Different spectra have been proposed e.g. by von Kármán [7] or Kaimal [8]. A modern example based on the reproduction of an-isotropic spectral properties has been developed by Mann [9]. An important feature to go along with the spectra is the coherence of wind, which describes the correlation between two points in space in dependence of distance and frequency. Coherence essentially connects the spatial with the temporal dynamics in the wind field. A common model based on exponentially decaying correlation has been proposed by Frost [10].

However, there are known features of wind, which are commonly not included in the aforementioned models, as they are believed to be of minor importance. This work focuses on such a feature, namely the intermittency of turbulence, which is introduced comprehensively in Section 2.1. It can be understood as the non-Gaussian distribution of wind velocity changes or ‘increments’ u_τ . Increments are by definition a two-point property and contain additional information to one-point statistics like the mean value of a process. They can easily be obtained from a given wind velocity time series $u(t)$ for a time scale τ as

$$u_\tau = u(t + \tau) - u(t). \quad (1.1)$$

Common wind models implicitly model these increments as Gaussian processes, which is a simplification since their non-Gaussianity is neglected. In doing so, wrong predictions about the occurrence of these increments can be made. As pointed out by Böttcher et al. [11], increments with large amplitudes are modeled with the biggest error, which might be relevant with respect to the longevity of wind turbines.

Therefore this work aims to analyze the importance of intermittency for wind turbine loads. In doing so, this work pushes the boundary on state-of-the-art wind modeling.

1.2 State of research

Other studies investigated intermittency in the context of wind energy. In this section, related investigations on the impact of intermittency on wind energy systems are presented.

The intermittency of turbulence and more so the non-Gaussian increment statistics of wind are known in the wind energy community since a long time, as for example discussed by Dutton and Højstrup already 1979 [12].

The recent discussion of non-Gaussian increments in the context of wind energy has been started by Böttcher et al. [13, 11]. The authors compare measured atmospheric data [14] against laboratory turbulence. The authors were able to describe scaling process of both flows with the same model, as proposed by Castaing [15], indicating both processes are governed by the same super statistics. In order to have a more consistent comparison against the stationary laboratory data, only the atmospheric measurements in a velocity range between $4.5 - 5.6 \frac{m}{s}$ were considered, as atmospheric measurement data is generally unsteady. Due to intermittency, the histograms of velocity increments u_τ of the measured data sets exhibit a strong non-Gaussianity. Fig. 1.1, taken from Ref. [11], shows a histogram of u_τ for $\tau = 4$ sec of a wind measurement. Additionally, a Gaussian fit is shown. Note that the ordinate is scaled logarithmically, wherefore the Gaussian fit in the figure does not show the typical bell shaped form of the normal distribution. In the logarithmic scaling however, the strong discrepancy between u_τ and a Gaussian process become evident: The occurrence of a velocity increment with of seven standard deviations occurs approx. 10^6 times more often than predicted by a Gaussian process. As stated by Böttcher et al., this corresponds to an event occurring five times a day, while is expected only every 500 years. Considering increments u_τ describe the gustiness of wind, it is imaginable that these wind dynamics have an impact on the dynamics and loads of wind turbines.

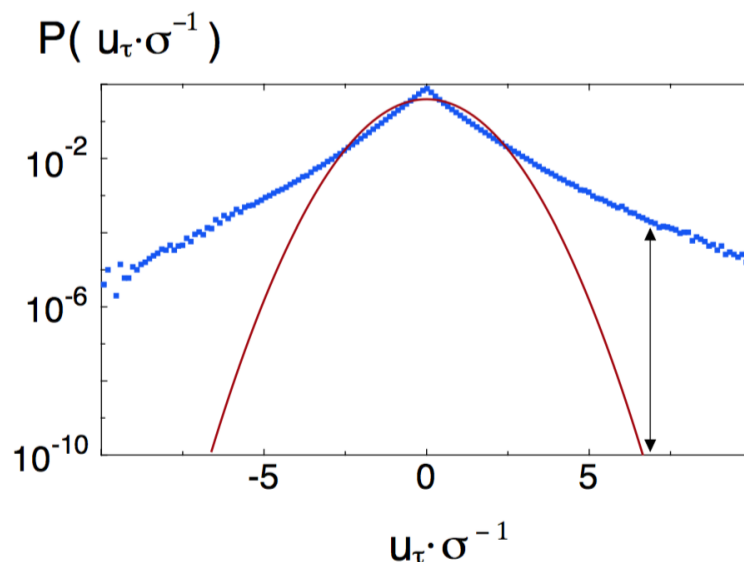


Figure 1.1: Histogram of measured velocity increments u_τ for $\tau = 4$ sec and Gaussian fit. Taken from Ref. [11], modified.

Motivated by the work of Böttcher et al. different efforts focusing on non-Gaussian power

increment statistics of single wind turbines and entire wind parks were made [16, 17, 18] within the last years. These can be interpreted as a footprint of the statistics of interest in the power grid. Milan et al. [17] fit a non-linear model to the scaling behavior of both the wind and power output data, relating both of these dynamics. Hähne et al. [18] conduct measurements of the power in the electric grid. The authors could show a signification relation between the non-Gaussianity of power increments and the amount of wind energy in the grid. The work by Milan et al. [17] and Hähne et al. [18] must be understood as strong evidence that intermittent dynamics are present within wind turbine systems. However in these studies wind turbines are treated as a black box and details on how intermittent dynamics propagate in the energy conversion process are not discussed. In order to advance the current understanding, this work analyses intermittency within the wind turbine system.

Other researchers investigated the issue of intermittency on the level of rotor aerodynamics. Many of these works rely on wind turbine simulation utilizing an intermittent wind model. Kleinhans et al. [19, 1] developed a wind model in order to generate non-Gaussian wind speed increments dynamics. It relies on Continuous-Time Random Walks (CTRW) and has been applied in related studies presented in the following. The so called ‘CTRW model’ is also utilized in this work. It is described in greater detail in Section 2.1.3.

Pioneering work with respect to intermittency and wind turbine loads was conducted by Gontier et al. [20]. The authors test two standard wind models (Kaimal [8], Mann [9]) and the intermittent CTRW wind model [1] with respect to their impact on fatigue loading of different sensors. Blade-Element-Momentum (BEM) theory based wind turbine computations were conducted. The authors drew conclusions to relevant load sensors, such as e.g. blade root bending moments and the tilt moment at the tower top. Differences in the fatigue loads for the different models were detected and described, but could not be embedded into a clear overall trend. Although the direct comparison of different wind models is interesting, the models feature fundamental differences that will affect the wind turbine loads, for instance different spectral properties. In other words: Intermittency is not isolated as the main difference between these wind fields. This represents an obstacle in drawing further conclusions from the presented study, as the reason for the deviations in the results obtained for different wind fields could also be a consequence of other statistical differences. The isolation of intermittency is a key aspect of this work and is discussed in Ch. 3.

Mücke et al. [21] adopted aspects of the methodology applied by Gontier et al. and added a comparison against measured wind data. Three types of wind field data were used: A measured data set from the GROWIAN experiment [22], a common Kaimal model [8, 6] and the CTRW model [1]. All types of wind fields are processed with an aerodynamic BEM based wind turbine model, neglecting servo-dynamic and elastic effects. The CTRW fields were designed in order to have comparable increment statistics as the GROWIAN fields. For all types of fields a high correlation between the wind increments statistics and the resulting torque increment statistics was found. Thus the authors showed that non-Gaussian wind statistics can lead to non-Gaussian torque statistics. A Rainflow-Counting (RFC) analysis [23] was conducted on the resulting torque data both of the GROWIAN measurement field and the Kaimal field. The authors conclude that the RFC method is not sensitive to the intermittent dynamics, as a certain amount of temporal information is lost within a RFC procedure. In general, the comparison against measured wind data is of high interest, but also challenging: When comparing wind

fields with respect to their impact on wind turbines, several wind characteristics need to be equivalent before conclusions with respect to intermittency can be drawn. This again relates to the isolation of intermittency, discussed in Ch. 3.

A different approach to obtain intermittent wind fields was utilized in the study presented by Berg et al. [24]. The authors investigate wind fields derived from Large-Eddy-Simulations (LES) of the Atmospheric Boundary Layer (ABL). Snapshots of ‘frozen’, three-dimensional velocity fields, exhibiting the intermittent dynamics, were extracted from the simulation result. The three spatial dimensions are converted into an unsteady, two dimensional velocity plane via Taylor’s Hypothesis of frozen turbulence and processed through a common aero-servo-elastic model of a wind turbine. Gaussian fields were obtained by deriving surrogate fields based on Proper Orthogonal Decomposition (POD) of the original data. In doing so, the exact same second-order statistics were obtained for the surrogate, non-intermittent fields. Twenty fields of each type were processed through a BEM based aero-elastic wind turbine model in order to evaluate the impact of intermittency on wind turbine loads. Both ultimate and fatigue loads resulting from these simulations were compared. The authors do not find any significant evidence that intermittency alters any of the two types of loads. It is therefore concluded that the relevant dynamics are low-pass filtered by the turbine, as they are mainly found in small structures below the rotor scale. However, the authors do not discuss the sizes of wind structures further. The work by Berg et al. successfully delivers an approach that respects other statistics of wind fields and aims at the isolation of intermittency: The approach of generating a pair of wind fields with highly comparable statistics – aside from the distribution of velocity increments. In the author’s opinion this is the preferable approach to analyze the impact of intermittency on wind turbine loads wherefore this work follows this approach.

In addition to the studies mentioned above, experimental work has been conducted on this subject, as well. Schottler et al. [25] compared Gaussian and non-Gaussian wind fields in an experimental campaign featuring a model wind turbine and an active grid. The authors compare the response of the model wind turbine to two different kinds of inflows: One with Gaussian, the other with non-Gaussian increment statistics. The authors demonstrate that the turbines response (e.g. the rotor thrust) still contains the non-Gaussian dynamics, demonstrating that intermittent wind dynamics are not filtered by the rotor, as brought forward by Berg et al. [24]. The two types of wind fields are constrained to have similar first and second statistical moments, however their wind fluctuations u' might be differently behaved. The comparability of the distribution of velocity fluctuations is important to this problem, which is further discussed in Sec. 3.1.

In a recent national project [26] the effect of intermittent wind dynamics on fatigue loads was tested. Synthetic Kaimal [8], Mann [9] and CTRW [1] wind fields were processed in a BEM-based wind turbine model. The resulting load time series were applied experimentally to material probes until failure. Significant differences between the field types were evident. However due to differences in the fields with respect to their spectral properties and coherence, these findings cannot be attributed to the non-Gaussian increment statistics exclusively. However the approach of testing material probes directly is innovative and interesting, as one does not rely on load models since these have limitations. For instance, it is commonly not taken into account over which time span a load change occurs.

In summary, many studies with respect to the question if intermittency affects the wind turbine system have been conducted. However there exist contradictions in their conclusions: It remains unclear whether intermittency is filtered by the rotor or not and whether it is an important effect in the context of wind turbine loads.

1.3 Scope of this work

This work aims to investigate the impact of intermittency on wind turbine systems. For this purpose two types of highly similar wind fields, which vary only in the fourth moment of their increment statistics (and even more advanced statistics) are generated. In doing so, the intermittency effect can be investigated in isolation. The resulting fields are used as an inflow in several wind turbine simulations based on Blade-Element-Momentum theory. The load time histories resulting from these simulations are evaluated by Rainflow-Counting algorithm. Both the wind turbine simulations as well as the load analysis are industry standards.

It is aimed to add the following specific contributions to the discussion:

- The importance and implementation of the proper isolation of intermittency is presented. It will be discussed why and how intermittency can be isolated. The resulting wind dynamics are discussed in this work.
- An intermittency effect for idealized wind fields with large flow structures is reported. This work shows that fatigue loads of wind turbines can change in a relevant order of magnitude when intermittency is considered.
- The dependency of the intermittency effect on model parameters, mainly the size of wind structures, is addressed. It will be shown that the intermittency effect is changing for differently sized coherent structures in the wind field.

This work is structured as follows:

- Ch. 2 provides a general, theoretical foundation about wind models, intermittency, wind turbine simulation and analysis of dynamic loads.
- Ch. 3 discussed the specific parametrization and set-up of all utilized models for wind, turbine and loads in this work and gives further relevant details.
- In Ch. 4 results of the conducted study are presented. An intermittency effect for large, idealized flow structures is reported.
- In Ch. 5 further results are presented, which show the dependency of the intermittency effect on different parameters, mainly on the size of coherent wind structures.
- Conclusions and an outlook are given in Ch. 6.

Chapter 2

Fundamentals of the utilized models

In order to investigate the intermittency effect on wind turbines, synthetic wind fields are generated and fed to a common turbine simulation tool. The resulting load response is investigated with a standard fatigue analysis approach. This chapter aims to provide a theoretical foundation for all the steps of this procedure. An introduction into intermittency and wind modeling is given in the following section, Sec. 2.1. The underlying theory and specifics of the utilized wind turbine model are discussed in Sec. 2.2. Lastly the load analysis approach is presented in Sec. 2.3.

2.1 Intermittency and wind modeling

This section aims to provide the reader with a basic understanding of the wind fields used in this study. In doing so, the intermittency of turbulence is introduced in Sec. 2.1.1. Subsequently, an overview over common wind models is given in Sec. 2.1.2. Lastly the intermittent wind model utilized in this work, the CTRW model, is discussed in Sec. 2.1.3

2.1.1 Introduction to turbulence intermittency

As a starting point for the intermittency of turbulence the work of Kolmogorov in 1941 is discussed. Subsequently a brief introduction into increment statistics is given, leading to Kolmogorov's and Obhukov's work from 1962. Lastly, an overview over the quantification of intermittency in this work is given. More general and comprehensive information on this topic are found in Nelkin [27] or Pope [28].

K41: The $\frac{5}{3}$ - spectrum

Turbulence is commonly regarded as a process on multiple scales and more so, as a cascade of energy from large to small scales, as summarized in the popular poem by Richardson [29].

Kolmogorov in 1941 [3] presented a scale analysis based on these ideas, from which several relations of different physical quantities could be formulated. This work is nowadays referred to as *K41*. A key aspect of *K41* is the dimensional analysis of the energy cascade process. Kolmogorov derived the universal, quantitative scaling law

$$E(k) \propto k^{-\frac{5}{3}}, \quad (2.1)$$

that describes how energy is transferred down from larger to smaller scales. Here E represents the energy density on the scale with the wave-number k . Eq. (2.1) holds true in a range between the largest and smallest scales of the flow. In this range of scales dissipation can be neglected. Therefore this regime is driven by inertial forces and referred to as the *inertial sub-range*. The $-\frac{5}{3}$ -trend in the inertial sub-range has been confirmed experimentally [28, 30]. It constitutes a quantitative description of the transfer of energy from the largest scales the *energy containing range* through the *inertial sub-range* down to the *dissipation range*. A schematic energy spectrum of turbulent flow according to K41 is shown in Fig. 2.1.

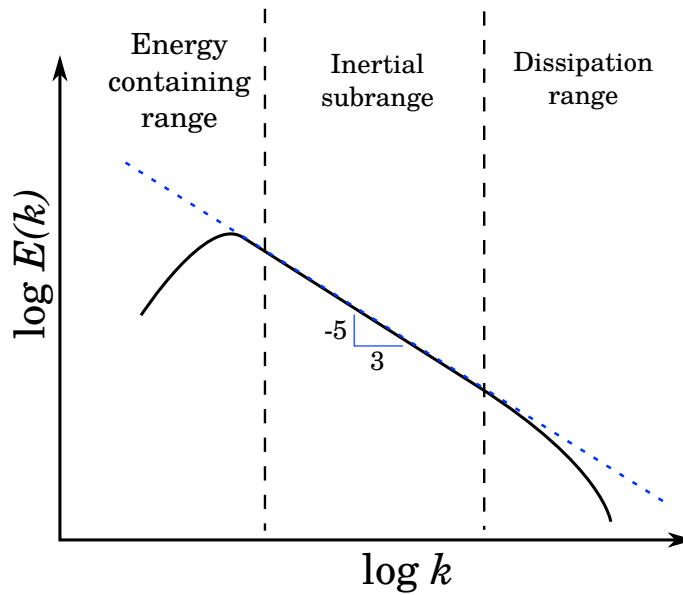


Figure 2.1: Schematic energy spectrum according to K41

Further expressions and relations can be derived. Another noteworthy result of Kolmogorov's work are micro-scales at unit Reynolds number $Re = 1$, which describe the smallest time and length scales in a turbulent flows, on which energy is dissipated. These are

$$\text{the Kolmogorov length scale } \eta = \left(\frac{\nu^3}{\varepsilon}\right)^{\frac{1}{4}}, \quad (2.2)$$

$$\text{the Kolmogorov time scale } \tau_\eta = \left(\frac{\nu}{\varepsilon}\right)^{\frac{1}{2}} \quad (2.3)$$

$$\text{and the Kolmogorov velocity scale } u_\eta = (\nu\varepsilon)^{\frac{1}{4}}. \quad (2.4)$$

Increment statistics

Before we can discuss further aspects of *K41* a brief introduction into the characterization of turbulence by velocity increments is necessary. As mentioned in Sec. 1.1, velocity increments, sometimes also referred to as accelerations or differential fluctuations, can be obtained from a given velocity time series $u(t)$ as differences under consideration of a time lag τ

$$u_\tau = u(t + \tau) - u(t). \quad (2.5)$$

By applying Taylor's Hypothesis [31] spatial and temporal dynamics of turbulent flows can be associated with another. The assumption of so called *frozen turbulence* can be expressed mathematically as

$$t = \frac{x}{\langle U \rangle}, \quad (2.6)$$

where $\langle U \rangle$ denotes the mean velocity (in the direction of x). Taylor's Hypothesis holds when the velocity fluctuations u' are much smaller than the so that $\frac{u'}{\langle U \rangle} \ll 1$. Applying Eq. (2.6) to the definition of temporal velocity increments in Eq. (2.5) allows us to derive spatial velocity dynamics $u(\vec{x})$ with a distance L as

$$u_L = u(\vec{x} + \vec{L}) - u(\vec{x}). \quad (2.7)$$

Commonly, the (statistical) moments of velocity increments are referred to as 'structure functions'. Accordingly, the structure function of the order n is given by

$$S_\tau^{(n)} = E[u_\tau^n] \quad (2.8)$$

and analogously for spatial dynamics

$$S_L^{(n)} = E[u_L^n]. \quad (2.9)$$

In Eqs. (2.8) and (2.9), $E[X]$ denotes the expectancy value of the process X .

K41: The $\frac{4}{5}$ - law

Now that increment statistics have been introduced, another important aspect of *K41*, the $\frac{4}{5}$ - law, can be discussed. It targets the third structure function $S_L^{(3)}$ of turbulent flows. Note that it can be derived from the Navier-Stokes Equations (NSE) directly through the *von Kármán-Howarth Equation*, c.f. Pope [28]. For the inertial sub-range the $\frac{4}{5}$ -law derives as

$$S_L^{(3)} = E[u_L^3] = -\frac{4}{5}\varepsilon L, \quad (2.10)$$

where ε represents the energy dissipation rate per unit mass with the unit $[\varepsilon] = \frac{m^2}{s^3}$. From Eq. (2.10) it follows that velocity increment distributions are skewed as their third moment is

non-zero, which agrees with the physical idea energy transfer between different scales. Additionally, from the postulated scaling behavior in K41 it can be derived that structure functions are expected to scale

$$S_L^{(n)} \propto (\varepsilon L)^{\frac{n}{3}}. \quad (2.11)$$

However, experiments have shown that this scaling behavior does not hold [32]. Especially for high order statistics $n > 3$ Eq. (2.11) is not valid. The aspect that K41 does not hold in the aforementioned context is associated with the phenomenon of *internal intermittency*. Essentially, intermittency is the non-linear scaling of structure functions, which can further be understood as the breaking of the mono-fractal trend, which is postulated by self similarity hypothesis of K41. It also leads to non-Gaussian distributed velocity increment statistics.

K62

Based on prior work of Obukhov, Kolmogorov in 1962 [2] aimed to add the incorporate the intermittency of turbulence into the present theoretical understanding of K41. Based on an analysis of spatial averages of the energy dissipation ε and its dependence on the scale L the authors propose a log-normal distribution for this problem. This addition is nowadays known as the refined similarity hypothesis and simply referred to as K62. From K62, a correction to the structure function scaling in Eq. (2.11) can be formulated, cf. Pope [28], as

$$S_L^{(n)} \propto (\varepsilon L)^{\zeta_n} \quad (2.12)$$

with

$$\zeta_n = \frac{1}{3}n \left(1 - \frac{1}{6}\mu(n-3) \right). \quad (2.13)$$

The constant μ in Eq. (2.13) is experimentally found to be $\mu \approx 0.29$. Note that the non-linear structure function scaling of K62 is still in agreement with the $\frac{4}{5}$ -law of K41.

Quantifying intermittency

In order to investigate the impact of intermittency on wind turbines, we must clarify how intermittency can be quantified and formulated mathematically. In this work, intermittency is discussed in the context of the non-Gaussian scaling of velocity increments u_τ . The non-Gaussianity is evident in so-called *leptokurtic* (also *super-Gaussian*) Probability Density Functions (PDF) of u_τ , cf. Fig. 1.1. The deviation from a Gaussian PDF is well captured by the kurtosis or flatness $F(X)$ of a process X , where $F(X)$ is also the fourth standardized moment $F(X) = \tilde{\mu}_{n=4}$

$$\tilde{\mu}_{n=4} = \frac{\mu_{n=4}}{(\mu_{n=2})^2}, \quad (2.14)$$

which can be calculated from the centralized moments

$$\mu_n(X) = E[(X - E[X])^n]. \quad (2.15)$$

Here, E denotes the expectation operator. For an ideal Gaussian process it can be shown that $F(X_{\text{Gau}}) = 3$.

Since intermittency is a scale dependent process, the flatness of velocity increments becomes a function of the lag value τ so that $F(u_\tau) = F(\tau)$.

The flatness can further be related to the λ^2 parameter in the Castaing model [15], as applied by Böttcher et al. [11]. The formalism proposed by Castaing, models a process as a superposition of Gaussian processes with log-normally behaved variances σ . In doing so, the parameter λ (and thus λ^2) describes the variety of the Gaussian processes, as λ is the variance of the variances σ . Following the characterization approach by Castaing, it is popular to quantify the dependency of the non-Gaussianity on τ with $\lambda^2(\tau)$. As worked out by Chillà et al. [33] both quantifications based on the flatness $F(\tau)$ and the shape parameter $\lambda^2(\tau)$ can be related with one another as

$$\lambda^2(\tau) \approx \frac{\ln\left(\frac{1}{3}F(\tau)\right)}{4}. \quad (2.16)$$

This work uses Eq. (2.16) as an exact equation to translate between $F(\tau)$ and $\lambda^2(\tau)$.

An example for this scaling behavior is shown is given in Fig. 2.2 by Morales et al. [34]. It shows a comparison between measured and synthetic wind dynamics. The authors are able to show that $\lambda^2 \propto \ln \tau$, which follows from the scaling proposed in K62 in Eqs. (2.12) and (2.13) and the fact that the structure functions $S_\tau^{(n)}$ are essentially the central moments of the increments $S_\tau^{(n)} = \mu_n(u_\tau)$, cf. Eq. (2.8), because the mean value of the increments tends to zero.

2.1.2 Review of common wind models

Sometimes, for instance in the early rotor blade design process, it might be useful to assume that wind turbines are exposed to steady, non-varying inflow conditions, as a crude simplification. However at some point, more precise representations of wind are needed in order to make turbines safe and cost efficient.

Modeling the complex dynamics of wind is challenging. A common and successful approach is to represent the dynamics in the frequency domain. A spectral representation can be utilized to generate wind velocity time series by a Fourier transform. Different spectra have been proposed by e.g. von Kármán [7], Frost [10] and Kaimal [8]. Aside the spectrum, the phase information is required in order to transfer from frequency to real space. It is typically modeled as an uncorrelated random variable. In doing so, resulting time series will not be identical, but have the same features in the frequency domain. A comprehensive overview about spectral methods is given by Powell and Connell [37].

In addition to the spectral properties, the relationship of wind velocities at different points in space must be included. This aspect is commonly described by the ‘coherence’ of the wind.

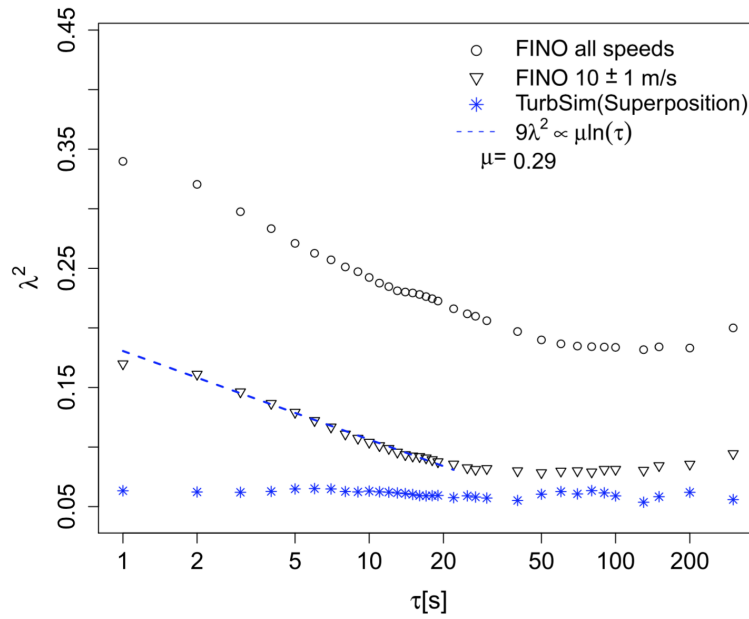


Figure 2.2: Castaing shape parameter λ^2 against lag value τ . *Circles*: Unconditioned wind measurements at FINO platform [35]. *Triangles*: Conditioned FINO data. *Blue asterisks*: Data originating from a common wind model [36] based on spectral representation. Taken from Ref. [34]

Commonly, this coherence is mathematically described by correlation between velocity fluctuations in the frequency domain at two different points in space (say the rotor plane) at a given frequency f . Generally, the correlation decreases exponentially both with the distance between the two points Δr and f , incorporating that high frequencies are connected to small structures and vice versa. In doing so, a relation between spatial and temporal dynamics is achieved.

Based on fundamental work of Shinozuka and Jan [38], Veers formulated a method based on the combination of a spectrum and a coherence model, which is known as the *Sandia method* [39]. Nowadays the Mann model [9], an advanced spectral-based approach, is widely regarded as the most accurate representation of wind dynamics and also recommended in the relevant guidelines for WT, such as Ref. [6].

However, there is a downside to the spectral definition of wind and randomized phase information. Note that the aforementioned power spectrum S_{xx} is related to the correlation function r_{xx} by the *Wiener–Khinchin theorem*

$$S_{xx}(f) = \int_{-\infty}^{\infty} r_{xx}(\tau) e^{-i2\pi f\tau} d\tau. \quad (2.17)$$

Correlation functions can be categorized as a second order, two-point statistic. Higher order statistics, say of the fourth order two-point statistics, related to the kurtosis of increments statistics, are not considered in the standard, spectral-based wind modeling approach. This is also evident, when we come back to Fig. 2.2. As pointed out e.g. by Powell and Connell [37] and Mücke et al. [21], the spectral based modeling approach implicitly models the wind dynamics as purely Gaussian, wherefore non-Gaussian dynamics of atmospheric turbulence are not included in the synthetic wind data.

2.1.3 Generation of intermittent wind fields: The CTRW model

For this work intermittent wind fields are required. They which cannot be generated with standard wind models, as discussed in the previous section. In this work, all wind fields have been generated with the CTRW model. Its properties are explained in this section.

Due to intermittency, all higher order statistics of atmospheric turbulence will differ from the ones of standard wind models. However, designing a stochastic process that takes into account the entire scaling behavior of turbulence is an extremely complex (if not impossible) challenge. Therefore in this work we focus on moderately higher order statistics. In the context of wind turbine loads, the fourth order two point (2P) statistics are especially interesting: When intermittency is considered, the fourth order two point statistics alias the kurtosis of the wind velocity increments become non-Gaussian. In fact, they become leptokurtic or heavy-tailed, meaning that the occurrence of extreme wind velocity increments is increased compared to the Gaussian behaved standard wind models. In order to investigate the intermittency effect on wind turbines it is thus in the focus of our approach to incorporate a realistic scaling of the fourth order two point statistics into the wind fields, represented by $F(\tau)$. Note that the statistics of the one point (1P) wind fluctuations

$$u'(t) := u(t) - E[u(t)] \neq u_\tau \quad (2.18)$$

are commonly assumed to be stationary and Gaussian behaved [6]. It is thus the challenge to generate wind data with Gaussian 1P statistics and non-Gaussian 2P statistics.

Böttcher et al. [11] introduced the discussion of wind and intermittency based on waiting time scales for extreme events, depending on the magnitude of these events. Following this train of thought, Kleinhans and Friedrich [1, 19] proposed a model for wind time series generation based on a waiting time process, a so called Continuous-Time-Random-Walk (CTRW) method. Therefore this model is referred to as the *CTRW model*. It has been applied in previous studies related to the presented issue [20, 21]. The models' main building blocks are two coupled Ornstein-Uhlenbeck processes and a stochastic mapping process, which are discussed in the following. Velocity signals $u(s)$ are generated as coupled Ornstein-Uhlenbeck (OU) processes on a model-intrinsic time scale s . The OU processes are

$$\frac{d\vec{u}_r(s)}{ds} = -\gamma_r(\vec{u}_r(s) - \vec{u}_0) + \sqrt{D_r}\vec{\Gamma}_r(s) \quad (2.19)$$

and

$$\frac{d\vec{u}_i(s)}{ds} = -\gamma(\vec{u}_i(s) - \vec{u}_r(s)) + \sqrt{D_i}\vec{\Gamma}(s). \quad (2.20)$$

In the previous Equations

$$\vec{u}_r(s) = \begin{pmatrix} u_r^{(x)}(s) \\ u_r^{(y)}(s) \\ u_r^{(z)}(s) \end{pmatrix}, \quad \vec{u}_0 = \begin{pmatrix} u_0^{(x)} \\ u_0^{(y)} \\ u_0^{(z)} \end{pmatrix} \quad \text{and} \quad \vec{\Gamma}_r(s) = \begin{pmatrix} \Gamma_r^{(x)}(s) \\ \Gamma_r^{(y)}(s) \\ \Gamma_r^{(z)}(s) \end{pmatrix}. \quad (2.21)$$

Γ represents a Wiener process. The reference process $u_r(s)$ aims to model low frequent fluctuations, and can be interpreted as a varying mean value of the the process $u_i(s)$. It is also

scales the fluctuations of $u_i(s)$ accordingly. Furthermore, \vec{u}_0 represents the mean value of the reference process $u_r(s)$.

The key feature of the model is the stochastic time mapping process, which allows for the generation of intermittent dynamics. A mapping of the intrinsic time scale s to the physical time scale $s \rightarrow t$ is realized as

$$\frac{dt(s)}{ds} = \tau_{\alpha,C}(s), \quad (2.22)$$

where $\tau_{\alpha,C}$ is essentially a waiting time distribution. This idea is based on the concept of Continuous Time-Random Walks (CTRW), cf. e.g. Ref. [40]. Kleinhans [1] proposes a stochastic Lévy process for τ_α . For $0 < \alpha < 1$, τ_α yields Lévy distributed random numbers larger than zero. In case of $\alpha = 1$ the mapping is identical so that $\tau_1 = 1$ and $s = t$ and in return $u(s) = u(t)$. As pointed out by Kleinhans [1], an implementation of such a Lévy distributed random numbers can be achieved as

$$\tau_\alpha = \frac{\sin\left(\alpha\left(V + \frac{\pi}{s}\right)\right)}{\cos(V)^{\frac{1}{\alpha}}} \left(\frac{\cos\left(V - \alpha\left(V + \frac{\pi}{s}\right)\right)}{W}\right)^{\frac{1-\alpha}{\alpha}}, \quad (2.23)$$

with V being uniformly distributed random variable between $[-\frac{\pi}{2}, \frac{\pi}{2}]$ and W being an exponential distribution with unit mean. In order to avoid waiting times $\tau_\alpha \rightarrow \infty$ the Lévy process is bounded to yield a maximum waiting time C .

2.2 Wind turbine modeling

In order to predict the loads and performance of wind turbines, it is necessary to rely on suitable simulations models representing the physical and technical aspects of the entire wind turbine system.

A central part is the aerodynamic modeling Navier-Stokes based models, so called Computational Fluid Dynamics (CFD) simulations, can be regarded as the most physical computational models, as the physics of flow are fully described by the Navier-Stokes Equations (NSE). Several computationally CFD variants exist, such as Direct Numerical Simulation (DNS), Large Eddy Simulation (LES) or Reynolds-Averaged Navier-Stokes (RANS) methods. Nowadays it is possible to conduct CFD simulations of fully resolved wind turbine geometries, even including elastic and servo-dynamic effects. Due to the immense computational effort however, such methods are only deployed if the expenses can be justified.

However for the sake of cost efficiency, industrial developers and researchers often rely on models containing much less physics. In doing so, the computational effort can be decreased drastically. The most widely used kind of model in wind turbine rotor aerodynamics is the Blade-Element / Momentum (BEM) theory. It is based on a momentum balance of the stream tube containing the rotor, which then is modeled based on independent rotor segments, so called blade elements. Due the high demand for simulation data in order to resolve the statistical features of interest and its relevance in wind energy industry, BEM theory is utilized as an aerodynamics model in this work. In the following Sec. 2.2.1 the BEM theory is described. Subsequently, the specifications of the utilized wind turbine model are given in Sec. 2.2.2.

2.2.1 Blade-Element/Momentum theory

The Blade-Element/Momentum (BEM) theory combines the concept of independent Blade Elements (BE theory) with a momentum balance of the flow. This section aims to outline its derivation. More comprehensive literature are e.g. Refs. [41, 42].

In order to introduce BEM theory, in the following the underlying actuator disc model is introduced, from which conservation formulations of axial momentum in the flow can be derived. Subsequently, the rotational velocity induction will be discussed. Afterwards some basic aspects of BE theory are presented. Finally, those derived ideas are merged together resulting in the BEM algorithm. Modern BEM simulation include a number of correction models for different kind effects. An overview about these is given as well.

Actuator disc model and conservation of mass and axial momentum

Consider an actuator disc representation of the rotor within a stream tube as shown in Fig. 2.3, also known as a Rankine-Froude model.

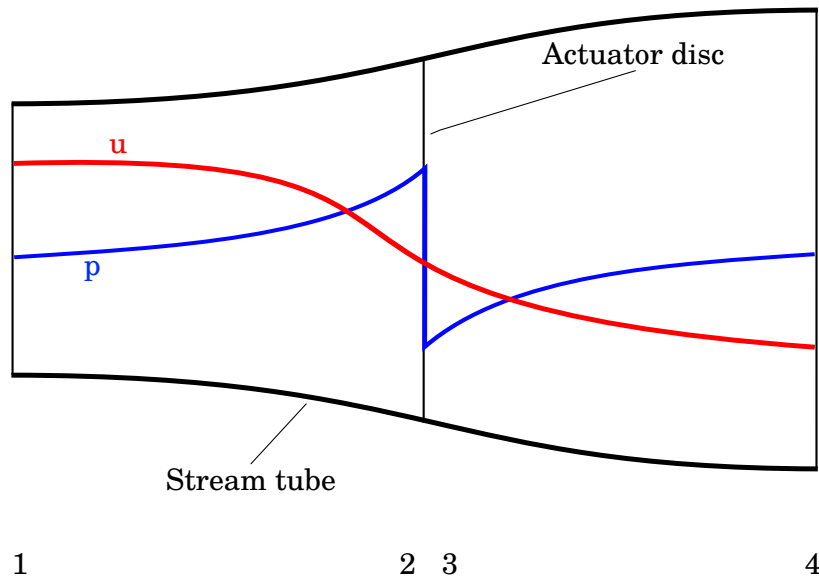


Figure 2.3: Actuator disc model within a stream tube. Schematic trends of axial flow velocity and pressure.

The actuator disc leads to an increased pressure p due to stagnation upstream of the rotor plane. The pressure drops across the disc due to the extraction of energy. Far up- and downstream, the pressure will recover so that $p_1 = p_4 = p_{amb}$. On the contrary, the flow velocity u gradually decreases from the inflow velocity u_1 to u_4 .

Assuming an adiabatic flow, the thrust force T acting between the flow and the fluid can be expressed as the change in the flow's momentum, which again is equal to the change in velocity times the mass flow rate so that

$$T = \dot{m}(u_1 - u_4). \quad (2.24)$$

Due to conservation of mass, the mass flow $\dot{m} = \rho u A$ is constant over the entire stream tube, where ρ represent the fluid's density and A the cross-sectional area of the stream tube. In incompressible flow $\rho = \text{const.}$, so that

$$T = \rho u_D A_D (u_1 - u_4) \quad (2.25)$$

with $u_D = u_2 = u_3$ represents the flow velocity at the actuator disc and $A_D = A_2 = A_3$ the rotor disc area. Now, the Bernoulli equation is considered

$$\frac{1}{2}\rho u^2 + p + \rho gh = \text{const.} \quad (2.26)$$

Applying Eq. (2.26) to the upstream and downstream part of the stream tube yields

$$\frac{1}{2}\rho u_1^2 + p_1 = \frac{1}{2}\rho u_2^2 + p_2 \quad \text{and} \quad (2.27)$$

$$\frac{1}{2}\rho u_3^2 + p_3 = \frac{1}{2}\rho u_4^2 + p_4. \quad (2.28)$$

Using the identities $p_1 = p_4$ and $u_2 = u_3$ and rearranging yields a relation between the pressure drop over the rotor disc and the net change in the velocity field far up- and downstream

$$p_2 - p_3 = \frac{1}{2}\rho(u_1^2 - u_4^2). \quad (2.29)$$

From basic hydro-statics it is known that the force between disc and fluid is related to the pressure acting on a disc's cross-sectional area, so that

$$T = \Delta p A_D = (p_2 - p_3) A_D = \frac{1}{2}\rho(u_1^2 - u_4^2) A_D. \quad (2.30)$$

Now, combining Eqs. (2.25) and (2.30) yields

$$\rho u_D A_D (u_1 - u_4) = \frac{1}{2}\rho(u_1^2 - u_4^2) A_D, \quad (2.31)$$

which can be rearranged to obtain an expression for the velocity at the disc $u_2 = u_3 = u_D$

$$u_D = \frac{1}{2}(u_1 + u_4). \quad (2.32)$$

Eq. (2.32) implies that the velocity deficit at the disc is half of the overall velocity deficit in the far wake. It is common to represent the velocities by means of induction factors. The axial induction factor a_{ax} represents the offset in wind velocity between the free, incoming stream and the slowed-down stream at the rotor disc, normalized by the free incoming, wind velocity. It is defined as

$$a_{ax} := \frac{u_{ind}}{u_1} = \frac{u_1 - u_2}{u_1} = \frac{u_1 - u_D}{u_1} \quad (2.33)$$

Using Eqs. (2.33) and (2.32), it is possible to express the thrust force as

$$T = 2\rho A_D a(1 - a)u_1^2 \quad (2.34)$$

Analogously, one can equate the power extracted from the fluid by the disc as the product of the flow velocity at the disc and the force between fluid and disc as

$$P = Tu_D = 2\rho A_D u_1^3 a(1-a)^2. \quad (2.35)$$

It is evident that there is an optimal induction for power extraction, which can be equated as $a_{ax,Betz} = \frac{1}{3}$, which is also referred to as *Betz induction*, resulting in a maximal power factor of $c_{P,Betz} = \frac{16}{27}$, also known as the *Betz limit*.

Wake rotation and angular momentum

Analogously to the axial momentum, it is common to consider the angular moment as well. Due to the conservation of angular momentum, the wake behind a rotor will rotated in the opposite direction. As for the axial velocities, it is assumed that the change in rotational velocity at the disc is 50% of the entire angular velocity change, cf. Eq. (2.32), so that the angular frequency in the far wake is $2a_{tang}\Omega r$, where a_{tang} represents the tangential induction factor, analogous to Eq. 2.33 and Ω is the angular frequency of the rotor.

As in the previous chapter, the change in angular momentum is equated as the product of mass flow rate and change in angular velocity. We need to multiply by the radius, since a rotational movement is considered in contrast to the translational kinematics for the case of the axial momentum.

Due of the dependence of the rotational speed on the radius, instead of considering the entire rotor disc, annular rings with an area of δA_D are regarded. In doing so, the torque δQ acting on an annulus ring with the cross-sectional area δA_D is equated as

$$\delta Q = \rho \delta A_D u_1 (1-a) \Omega 2a_{tang} r^2. \quad (2.36)$$

Now, the power extraction of an annulus can be expressed as the product of torque and the relative angular frequency between rotor and fluid $\Omega(1+a_{tang})$ and combined with the axial momentum consideration of Eq. 2.35

$$\delta P = \delta Q \Omega (1+a_{tang}) = 2\rho \delta A_D u_1 (1-a) \Omega^2 r^2 a_{tang} (1+a_{tang}) \quad (2.37)$$

Blade Element theory and two-dimensional aerodynamics

The considerations of axial and angular momentum discussed above can be combined with Blade Element theory. The merging of both yields the so called Blade Element Momentum (BEM) theory. Blade element theory regards the blade as the assembly of aerodynamically independent blade segments, for which a two-dimensional flow situation is assumed. A blade element with a given flow situation is presented in Fig. 2.4.

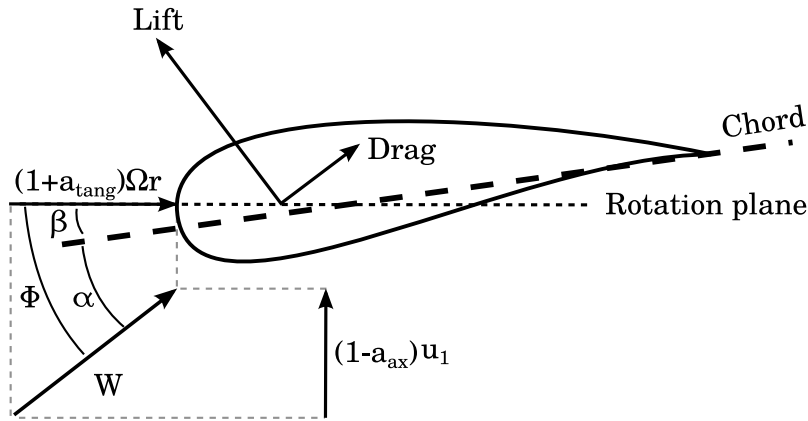


Figure 2.4: Two-dimensional flow in the vicinity of a blade element.

The relative inflow W can be expressed by the axial flow component at the disc $(1 - a_{ax})u_1$ and the rotational flow component $(1 + a_{tang})\Omega r$. The angle between the rotation plane and the inflow velocity is known as the flow angle ϕ . The angle between the chord line and the rotation plane β is the sum of the twist and pitch angle. Further, the Angle Of Attack (AOA) α represents the misalignment between the inflow W and the chord line. The inflow W at the AOA α induces two forces on the the airfoil section, namely lift and drag. By definition, the drag force is collinear with W and the lift force is orthogonal to it. The lift force experienced by a blade element is depending on the dynamic pressure, $\frac{1}{2}\rho W^2$, the plan-form of the element $dA = cdr$ (assuming the chord length c to be constant over dr) and the geometry of the airfoil, which affects how much lift is generated. This characteristic performance is summarized in the lift coefficient c_L , which strongly depends on the AOA, $c_L = f(\alpha)$. Hence, the lift dL experienced by a blade segment of span dr can be equated as

$$dL = \frac{1}{2}\rho W^2 c_L(\alpha) cdr, \quad (2.38)$$

and analogously for the drag

$$dD = \frac{1}{2}\rho W^2 c_D(\alpha) cdr, \quad (2.39)$$

where $c_D(\alpha)$ is the drag coefficient.

The airfoil properties $c_L(\alpha)$ and $c_D(\alpha)$ are typically evaluated by wind tunnel measurements and fluid dynamic computations. Both of these force components can easily be transferred with knowledge of the flow angle ϕ into a normal (to the rotation plane) force coefficient c_{norm} and a in plane or tangential force coefficient c_{tang} . This again allows to evaluate the contribution of each element to the thrust and torque.

Basic Blade Element Momentum (BEM) theory

Using the previously derived expressions and relations and combining the momentum balances with BE theory, results in the Blade Element Momentum (BEM) theory. It can be utilized to estimate the induction and hence the local flow situations and local forces along with the overall turbine thrust, torque and power. Equating the different formulations for the thrust of one blade element, using one relation derived from the momentum balance and one from Blade Element theory yields

$$T_{Momentum} = \rho c d r u_1 (1 - a_{ax}) 2 a u_1 \quad (2.40)$$

$$= T_{BladeElement} = B \frac{1}{2} \rho W^2 c d r c_{norm}, \quad (2.41)$$

where B denotes the number of rotor blades. The expression above can be rearranged further using $W = \frac{u_1(1-a)}{\sin \phi}$ (cf. Fig 2.4) into

$$\frac{a_{ax}}{1 - a_{ax}} = \frac{B c c_{norm}}{8 \pi r \sin^2 \phi}, \quad (2.42)$$

so that

$$a_{ax} = \frac{K_1}{1 + K_1} \quad \text{with} \quad K_1 = \frac{B c c_{norm}}{8 \pi r \sin^2 \phi}. \quad (2.43)$$

A similar expression for a_{tang} can be derived in the same manner as

$$\frac{a_{tang}}{1 + a_{tang}} = \frac{B c c_{tang}}{4 \pi \sin(2\phi)} \quad (2.44)$$

and

$$a_{tang} = \frac{K_2}{1 - K_2} \quad \text{with} \quad K_2 = \frac{B c c_{tang}}{4 \pi \sin(2\phi)}. \quad (2.45)$$

A basic formulation of an algorithm is given in Fig. 2.5.

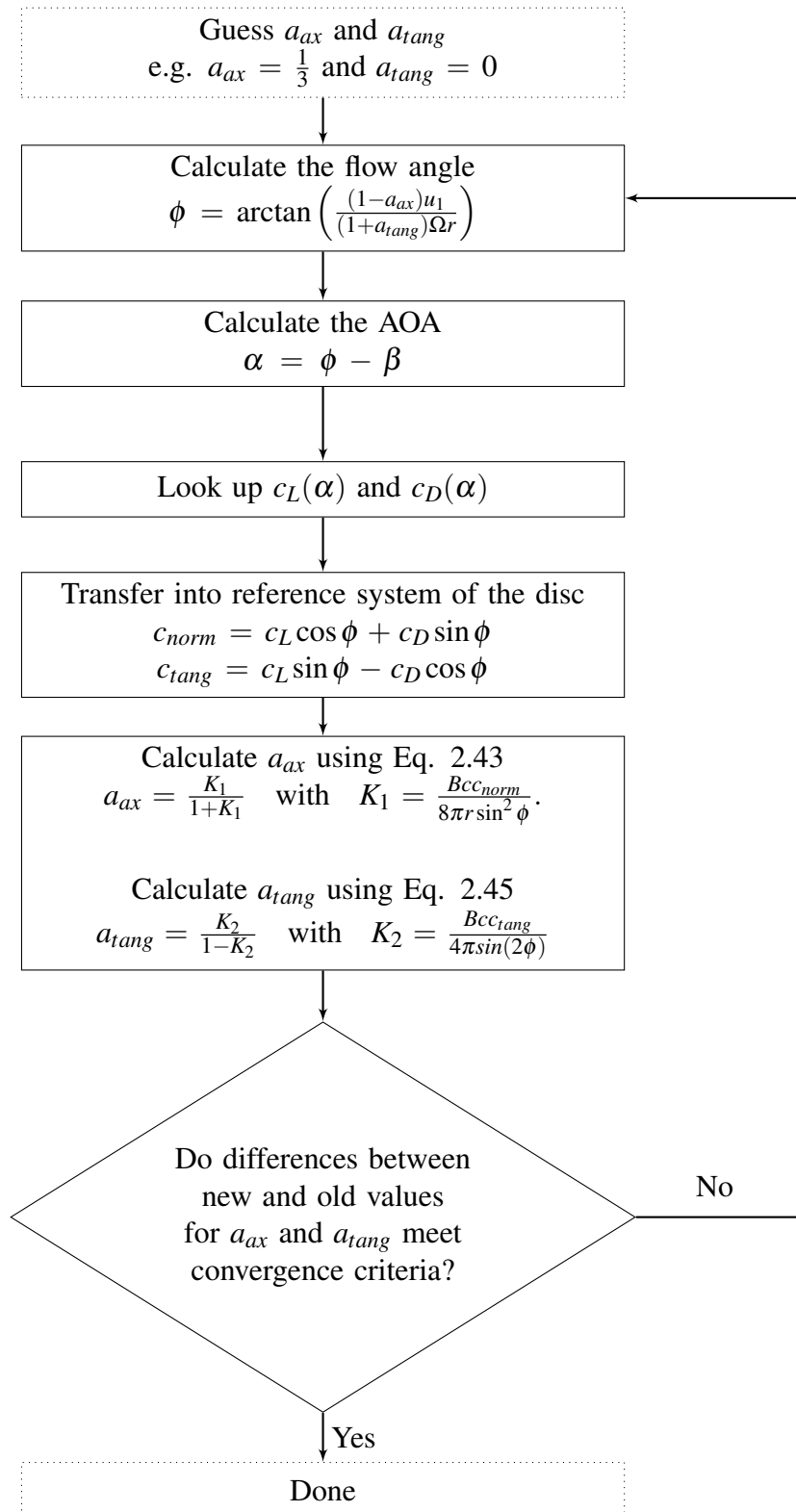


Figure 2.5: Basic BEM algorithm

Notable Additions

The basic BEM theory as outlined above is usually combined with a number of additions and correction models. A comprehensive index of correction models is given by Schepers [41]. A brief overview is given in the following:

- **Finite number of blades**

BEM theory relies on an actuator disc model, which can be interpreted as a rotor with an infinite number of blades. In contrast to this simplification, wind turbine rotors feature a finite number of blades. Towards the blade tip, the assumption of a disc is violated most dramatically, as local solidity is the smallest. Two statements can be made about the induction near the blade tip: On the one hand, a lot of air can pass through the rotor disc without any interaction of a rotor blade. Therefore, the deceleration of the air flow through the disc in an annulus near the tip is relatively low. On the other hand, the vortex that is shed from the blade tip, which is a natural consequence of the bound circulation along the rotor blade (comparable to the vortices shed by an air plane), blocks the flow drastically but only in the vicinity of the blade. Summarizing both statements, there is a discrepancy between local induction at the blade (relevant to blade element theory) and the azimuthally averaged induction (relevant to the momentum equations). This discrepancy is commonly covered by a so called tip-loss factor F , which essentially describes the ratio between local induction and azimuthally averaged induction. A common model for F has been formulated by Prandtl, cf. Glauert [43]. An analogous model for the root vortex can be derived and applied in a similar manner.

- **Turbulent wake state correction**

When the turbine decelerates the flow too much, the wake becomes turbulent so that basic assumptions of BEM theory are not valid anymore. The momentum equations do not hold in case the induction factor is larger than $a_{ax} \approx 0.4$, as the stream tube model implies only positive velocities in axial direction (corresponding to flow from left to right in Fig. 2.3). Momentum theory predicts a parabolic trend for the thrust $T(a_{ax})$ with a max. thrust coefficient at $a_{ax} = 0.5$, implying for larger values a decreasing thrust and further, negative velocities for u_4 . In a real application, the thrust continues to increase with a_{ax} . This operation mode is referred to as the turbulent wake state. It is common practice to correct for this behavior with empirical models, e.g. Glauert [43].

- **Tower passage**

Aside from the rotor, the wind turbine tower poses another obstacle for the wind. Due to the tower, the flow is decelerated and deflected. Hence, a rotor blade passing a tower, will be subjected to a different inflow than at other azimuthal positions. This effect is commonly corrected for by modifying the inflow velocity components according to a simple potential flow solution around a cylinder, representing a tubular tower.

- **Rotational boundary layer behaviour**

BEM commonly relies on two-dimensional (2D) aerodynamic data, while the flow situation in a real application is three-dimensional (3D). In a 3D case, separated flows near the root are accelerated radially towards the tip due to centrifugal forces and a radial pressure gradient. The outboard movement results in a curved trajectory over the blade surface due

to a Coriolis effect. Hence, there is an additional component of motion along the chord, which works against the adverse pressure gradient. This in return, generally results in thinner boundary layers and thus higher aerodynamic efficiency, wherefore 3D blade segments generally produce higher lift than 2D segments. The effect is most dominant in the root region. The phenomena is also referred to as Himmelskamp effect, stall delay or stall augmentation. It is common practice to modify the 2D input data before carrying out BEM simulations. A model commonly used has been proposed by Du and Selig [44].

- **Skewed wake correction**

In case of misaligned inflow (also *yawed* inflow), two effects need to be considered. Firstly, the relative velocity between the blade and the inflow vector changes over the course of a rotation, as the blade goes "in and out" of the wind. This effect is referred to as *advance and retreat* and can be incorporated by the use of a rotation matrix. The second effect is the skewed wake. For example the shed vorticity near the tip will not be convected axially downstream, but will also move with a lateral component, which is not captured in basic BEM, as the blade elements are assumed to be independent. The effect of the skewed wake is usually captured by semi-empirical correction models such as e.g. [45, 46].

- **Dynamic wake**

A basic BEM formulation relies on a steady equilibrium of momentum far up- and downstream of the rotor disc. This aspect is referred to as the equilibrium wake assumption. However in practical applications this assumption is violated when the induction of the turbine changes e.g. due to varying inflow or a pitch action. In such a scenario the flow velocity in the wake of the turbine does not change instantaneously, but with a certain lag and so does the induction of the turbine. This concept is sometimes referred to as the dynamic wake. It can be modeled with an inclusion of a time derivative of the induction calculation [41].

- **Unsteady airfoil dynamics**

The airfoil data used in BEM theory, is based on a steady flow condition. As for the dynamic wake, such conditions are not always representative for practical applications. The aerodynamic behavior of an airfoil exposed to an unsteady, dynamic inflow can vary strongly from its steady airfoil characteristics. These effects are commonly accounted for by dedicated model, as the Beddoes-Leishman model [47]. Other examples are the ON-ERA and Oye model. A detailed overview is given by Björck [48]. A rough outline over the effects modeled by a Beddoes-Leishman type model is given in the following, as it is relevant to the presented work. During attached flow the effect of shed vorticity resulting from a change in bound circulation on the net flow around the airfoil is modeled. Additionally, impulsive load effects encountered in association with e.g. plunging and fast changes of the flow angle are taken into account. In separated flow the changing position of the boundary layer separation point is modeled. Lastly, in case of leading edge separation the effects associated with dynamic stall, namely the vortex formation and roll up over the suction side are accounted for.

2.2.2 Turbine model specifications

Generally, it is an open question how well load dynamics resulting from turbulent inflow are captured by a BEM based method. A recent study [49] showed that BEM codes are capturing general trends well. Additionally, the BEM method remains relevant due to its unquestioned importance in the industry. Thus, all wind turbine simulations were carried out using *FAST* (v8.15) [50, 51], including its BEM code *AeroDyn15* (v15.02) [52].

As a generic test wind turbine the well known National Renewable Energy Laboratory (NREL) 5-MW Reference Wind Turbine [53], with a rated wind speed of $11.4 \frac{m}{s}$ is used. The turbine is a horizontal axis, three bladed upwind turbine with a diameter of 126m, a tower height of 90m. The cut-in and cut-out wind speeds are $3 \frac{m}{sec}$ and $25 \frac{m}{sec}$, respectively. It is a well documented test case in the wind energy research community and one of the few comprehensive and public turbine models, including not only aerodynamic but also structural and controller data. The selected wind turbine model is representative for modern pitch-regulated wind turbines. Therefore the fundamental observations made in this work are expected to hold true for modern turbines in general.

The time step for the in-stationary simulations has been set to 0.01sec or 100Hz, respectively. It ensures numerical stability and also covers an adequate range of frequencies of the wind turbine system. The output frequency is set to 20Hz as it needs to be synchronous with the wind field time discretization, since the statistics of interest are otherwise distorted by numerical effects. The wind field discretization is discussed in Chapter 3.

Two BEM theory based models of the NREL 5-MW turbine with different complexity have been derived: Firstly a purely AERodynamic (AERO) model is considered. This is done in order to simplify the complex dynamics of the turbine system, in order to gain a deeper understanding of the intermittency effect. Secondly, in order to mimic the dynamics of a real application case, a common, comprehensive Aero-Servo-Elastic (ASE) model, is utilized. The ASE model represents elastic structural deformations of the rotor blades and turbine tower by a linear modal representation. Mode shapes are prescribed by the user as 6th order polynomials. The implemented turbine controller allows for variable rotor speed, aiming for optimal tip speed ratio in the pre-rated regime and constant rotor rotation in the post-rated regime. The pitch-controller is used as a collective pitch-to-feather regulation, utilizing a proportional-integral (PI) controller with scheduled gains. This control system represents the basic control principles of a modern wind turbine. A detailed comparison of both AERO and the ASE model is given in Tab. 2.1.

	ASE	AERO
Aerodynamics		
Polars	Experimental [53]	see ASE
3D Correction	Du & Selig [44, 53]	see ASE
Extrapolation	Viterna & Corrigan [54, 53]	see ASE
Tip & hub loss	Prandtl [52]	see ASE
Dynamic airfoil response	Modified Beddoes & Leishman [52, 47]	see ASE
Tower passage	Potential flow [52]	no, turned off
Turbulent wake	Glauert [55]	see ASE
Dynamic wake	no, not available	no, not available
Skewed wake	no, turned off	no, turned off
Structural DOF		
Blade bending	yes	no, turned off
Tower bending	yes	no, turned off
Torsional	no, not available	no
Servodynamics		
Active pitch control	yes, collective	no, fixed
Variable rotor speed	yes	no, fixed
Geometry		
Pre-bend	2.5°	no, turned off
Rotor axis tilt	5°	no, turned off

Table 2.1: Overview over the different wind turbine model set-ups utilized in this work

2.3 Load analysis

Load calculations for Wind Turbines (WT) are a fundamental and necessary phase in the planning, design and certification process. During this phase it is estimated which forces a given design will face during its life-time operation, but also during construction, maintenance and assembly. This section aims to give an insight into the load assessment of wind turbines. It is structured as follows: In Sec. 2.3.1 it is discussed how loads are dealt with in the wind energy industry and guidelines. Afterwards, we focus in on the aspects that are relevant to the scope of this work in Sec. 2.3.2. Subsequently in Sec. 2.3.3 the load calculation methodology that is applied in this work, is presented in greater details. Lastly a selection of load sensors is conducted and discussed in Sec. 2.3.4.

2.3.1 Introduction of design load cases

Commonly, loads can be distinguished from another and divided into subgroups. For instance, one might be interested in only a certain type of load that originates from a specific source, e.g. gravitational forces or aerodynamic forces. A different consideration might focus on how often a specific load or load pattern will be encountered during the lifetime of a design.

For wind turbine designs, loads are classified by the IEC 61400-1 standard [6], shown in Table 2.2. It divides the WT's lifetime into different scenarios, so called 'design situations'. These cover specific events as e.g. the start-up of a turbine, its shut-down, as well as normal operation mode. Even scenarios in which failures, for instance to the control system, occur are considered as well. For a given design situation different loads may be relevant. Therefore the design situations are again subdivided into the 'Design Load Cases' (DLC). For example, different wind events might occur, which obviously will result in different loads. The specification of the wind is given in the column *Wind condition*. Deterministic gust profiles like the Extreme Coherent gust with Direction change (ECD) or turbulence models like the Normal Turbulence Model (NTM) are prescribed. For details please be referred to Ref. [6]. The cases can be further categorized based on how often it is estimated to occur and thus which type of analysis is required. Two categories exist: The Ultimate (U) loads, which are expected to occur once or only very few times and Fatigue (F) load, which are expected to occur many times over and over again.

2.3.2 Selection of a design load case

This section elaborates on the load cases that are relevant to this work. In doing so, the difference between Ultimate and Fatigue loads is discussed in greater details.

For the scope of this work it is important to understand the concept of fatigue loads and its differences to ultimate loads. Machine components can fail due to fatigue because of a damage accumulation over time. Some examples for fatigue are:

- bending a paper clip by the force of hand repeatedly until failure,
- breaking of bicycle pedals due to cyclic loading or
- failures of mechanical springs due to repeated loading, e.g. in a garage gate.

Design situation	DL C	Wind condition	Other conditions	Type of analysis	Partial safety factors
1) Power production	1.1	NTM $V_{in} < V_{hub} < V_{out}$	For extrapolation of extreme events	U	N
	1.2	NTM $V_{in} < V_{hub} < V_{out}$		F	*
	1.3	ETM $V_{in} < V_{hub} < V_{out}$		U	N
	1.4	ECD $V_{hub} = V_r - 2 \text{ m/s}, V_r, V_r + 2 \text{ m/s}$		U	N
	1.5	EWS $V_{in} < V_{hub} < V_{out}$		U	N
2) Power production plus occurrence of fault	2.1	NTM $V_{in} < V_{hub} < V_{out}$	Control system fault or loss of electrical network	U	N
	2.2	NTM $V_{in} < V_{hub} < V_{out}$	Protection system or preceding internal electrical fault	U	A
	2.3	EOG $V_{hub} = V_r \pm 2 \text{ m/s}$ and V_{out}	External or internal electrical fault including loss of electrical network	U	A
	2.4	NTM $V_{in} < V_{hub} < V_{out}$	Control, protection, or electrical system faults including loss of electrical network	F	*
3) Start up	3.1	NWP $V_{in} < V_{hub} < V_{out}$		F	*
	3.2	EOG $V_{hub} = V_{in}, V_r \pm 2 \text{ m/s}$ and V_{out}		U	N
	3.3	EDC $V_{hub} = V_{in}, V_r \pm 2 \text{ m/s}$ and V_{out}		U	N
4) Normal shut down	4.1	NWP $V_{in} < V_{hub} < V_{out}$		F	*
	4.2	EOG $V_{hub} = V_r \pm 2 \text{ m/s}$ and V_{out}		U	N
5) Emergency shut down	5.1	NTM $V_{hub} = V_r \pm 2 \text{ m/s}$ and V_{out}		U	N
6) Parked (standing still or idling)	6.1	EWM 50-year recurrence period		U	N
	6.2	EWM 50-year recurrence period	Loss of electrical network connection	U	A
	6.3	EWM 1-year recurrence period	Extreme yaw misalignment	U	N
	6.4	NTM $V_{hub} < 0,7 V_{ref}$		F	*
7) Parked and fault conditions	7.1	EWM 1-year recurrence period		U	A
8) Transport, assembly, maintenance and repair	8.1	NTM V_{maint} to be stated by the manufacturer		U	T
	8.2	EWM 1-year recurrence period		U	A

Table 2.2: Design load cases according to the IEC 61400-1 standard for wind turbines [6].

A components failure due to fatigue occurs because of the progression of micro-fractures as shown exemplary in Fig. 2.6.

Failure due to fatigue happens when a component is exposed to a load pattern repeatedly. Therefore, the load cycle amplitudes that can cause fatigue failure are often significantly smaller than the maximum load that the material can withstand. With respect to wind turbines,

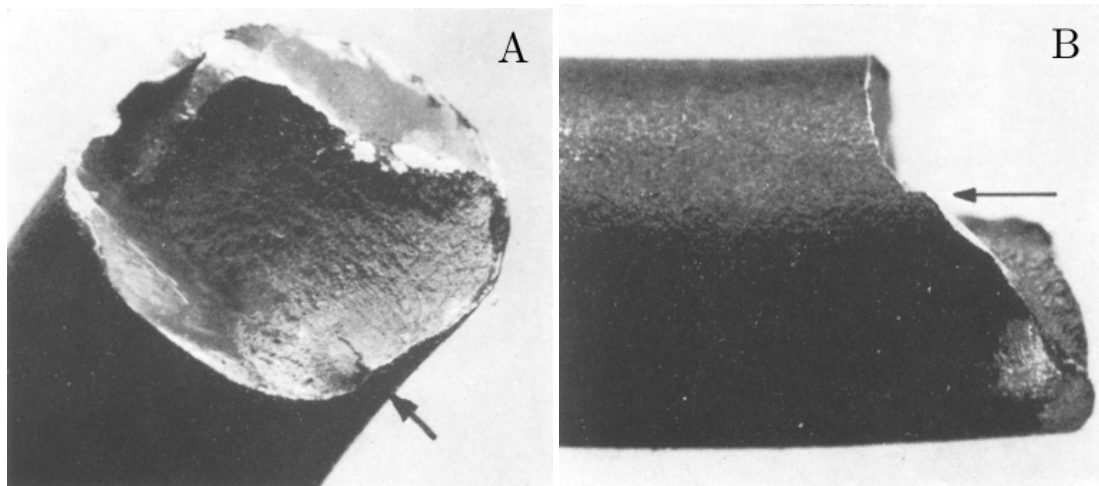


Figure 2.6: Crack growth and Failure of a metal spring due to fatigue. The arrows highlight the initial micro-fracture. Taken from Ref. [56]

fatigue loads are encountered due to the dynamic excitation of the machine by the wind that leads to the bending of the blades and tower, but also due to the rotation of the drive train components. Considering Table 2.2, the DLCs considering fatigue are DLC 1.2, 2.4, 4.1 and 6.4.

In contrast to fatigue loads, ultimate loads are related to single events and are evaluated against the maximal load resistance of a component or material. An example for wind turbines is the occurrence of an extreme gust, as for instance considered in DLC 1.4. The wind dynamics that are in the focus of this work are related to the probability distribution of wind speed changes. While this includes the occurrence of extreme wind speed changes, which potentially can lead to a local maximum in a related load time series. These are unlikely to exceed the ultimate loads encountered for deterministic gusts in DLC 1.4 or in design situation 6, in which so called *50-year gusts* are considered. While it is unquestioned that the ultimate load estimation in normal operation (cf. DLC 1.1 and 1.3) is driven by wind dynamics, it is not necessarily driven by the dynamics of *increments*. In other words, global load extrema can stem from a high wind speed change, but also from a high wind speed itself. In conclusion, an impact of intermittency on ultimate loads is possible.

However the estimation of fatigue loads strongly depends on the statistical nature of a load time series, which in DLC 1.2 is strongly related to the wind dynamics, including wind speed changes. A change in probability distribution of those changes can intuitively be related to a changed damage accumulation over time. Conclusively, the wind dynamics of interested are relevant in the context of fatigue loads rather than ultimate loads. While a detailed look into DLC 1.1 under consideration of intermittency is interesting as well, the biggest impact of intermittency is expected to occur in DLC 1.2, wherefore this work aims to investigate this scenario in detail. DLC 1.2 can be a design driver.

2.3.3 Fatigue load calculation

For the fatigue load calculation a specific routine, the RainFlow-Counting (RFC) procedure, is proposed by design guidelines and introduced in the following. Fatigue is a highly complex phenomenon and difficult to predict. Its occurrence and progression are depend on a multitude of initial conditions like the crystal texture of materials. Since information about these conditions practically cannot be captured and processed into a deterministic prediction, fatigue is commonly calculated as the statistical behavior of a given material or component. A characterization of material fatigue can be represented in an SN curve or Wöhler curve, shown idealized in Fig. 2.7. The data of the SN-curve is obtained from a Wöhler fatigue test: In such an experiment, a material probe is exposed to repeating load cycles of a constant amplitude until it fails. The number of cycles to failure N is plotted against the stress cycle amplitude S . A Wöhler test has to be conducted for multiple stress amplitudes and also repeated due to stochastic nature of fatigue, in order to gain statistical convergence for the resulting SN curve.

As can be seen from Fig. 2.7, the SN curve can be divided into three regimes: Material probes fail already after a few cycles $N \ll 10^4$, if the load cycle amplitude is in the order of the ultimate stress. This regime is referred to as Low Cycle Fatigue (LCF). Very small stress amplitudes that do not lead to failure after e.g. $N \simeq 10^7$ for steel are considered to be beyond the endurance limit. In this regime the component is fatigue endurable. The regime between LCF and the endurance limit is referred to as High Cycle Fatigue (HCF). For this regime, a double logarithmic plot exhibits a linear range cf. Fig. 2.7. The slope of this range, known as the SN slope coefficient m , is an important material constant in fatigue estimation. Typical values for wind turbine components are $m = 4$ for the steel tower, $m = 8$ for the steel-made drive train components and $m = 12$ for the blades, which are made from composite materials. The usage of these values implies that the fatigue behavior of interest categorizes as HCF.

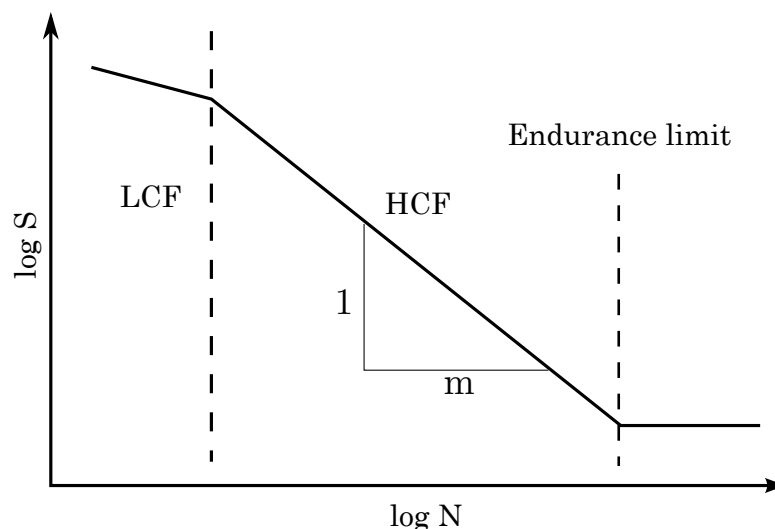


Figure 2.7: Idealized SN curve (germ. *Wöhlerlinie*). Between the Low Cycle Fatigue (LCF) regime and the endurance limit, the double logarithmic plot shows a linear behavior, which is represented by the slope coefficient m (germ. *Wöhlerexponent*)

Now, in order to estimate the fatigue damage accumulation one must count the load cycles that the object has been exposed to and compare these with the SN curve. If information about the load exposure is available by means of a load cycle histogram, the damage fraction C can be estimated as

$$C = \sum_{i=1}^k \frac{n_i}{N_i}, \quad (2.46)$$

where k denotes the number of amplitude bins, n_i represents the number of cycles of the i -th amplitude experienced by the probe and N_i is the number of cycles of the i -th amplitude that lead to failure. The probe is estimated to fail when $C = 1$. Eq. (2.46) is known as Miner's Rule [57]. In conclusion, the load cycle history is the key piece of information when estimating fatigue loads.

However, in technical applications often feature highly dynamic loading. For example, a wind turbine is excited by the wind loads, which are highly dynamic and irregular. In order to simplify a dynamic load time series into a load cycle histogram, a Rain-Flow-Counting (RFC) algorithm [23] is used. The purpose of load cycle counting methods is to provide information about how many load cycles of which amplitude are contained in a given load time series. Note that the load time series should feature a reasonable sampling frequency in order to resolve all load cycles and that it should be representative for a normal operation and therefore not include unusual behavior

The most common counting method is the RFC algorithm [23]. This work follows the methodology as described in Ref. [58] and is summarized in the following: Firstly, a given load time series is simplified into a sequence of local maxima and minima as shown in Fig. 2.8. Peaks can easily be identified by a comparison of the signs of the slopes surrounding the point of interest. Note that besides the order of the peaks and time span covered by the time series, all time information and all data between peaks is neglected in the remainder of the procedure.

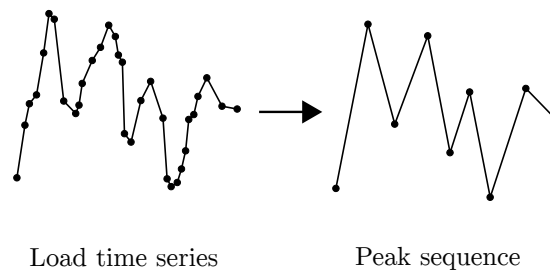


Figure 2.8: Exemplary load time series and a corresponding sequence of peaks

Successively, the sequence of peaks is re-interpreted by means of load or stress ranges. A load range is calculated as the difference between two peaks and can be understood as the peak-to-peak amplitude of a load cycle. Firstly, load range pairs are identified. A load range pair is evident, in case two successive peaks are framed by two peaks, which are either smaller or

larger than both of the two peaks in their middle, while the three slopes between all four peaks are of varying sign. An example for a decomposition of a peak sequence into a range pair and a single range is shown in Fig. 2.9. The range value for a range pair or a single range is calculated

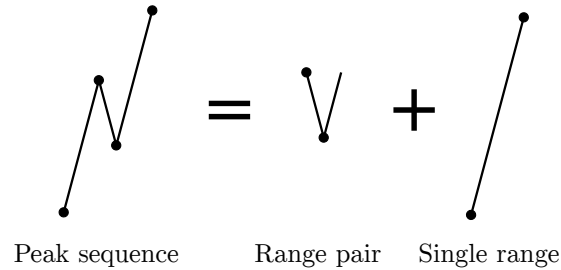


Figure 2.9: Decomposition of a sequence of peaks into load range pairs and single load ranges

by the difference between two peaks. Depending whether or not two peaks form a range pair or a single range, either two or one ranges are counted. With the information from an RFC algorithm, a load range histogram can be compiled.

Sometimes the bearable number of cycles N_i in Eq. (2.46) is unknown, as it depends not only on the material, but e.g. also on the actual design and geometry of a given component. In such a case it is still possible to give quantitative estimates about a given load time series. This is often done by means of an Equivalent Fatigue Load (EFL):

$$\text{EFL} = \left(\frac{1}{T} \sum_{i=1}^k S_i^m \right)^{\frac{1}{m}}, \quad (2.47)$$

where T represents the number of seconds covered by the load history, S_i is the i -th load ranges and m denotes the SN slope coefficient. Intuitively, the EFL can be understood as the peak-to-peak amplitude of a hypothetical load cycle with the period of 1s, which leads to the same damage accumulation as the input load history over the time T

2.3.4 Selection of load sensors

A wind turbine system has many components, each of which is exposed to a multitude of forces and moments. All of these can be seen as loads. Since this study constitutes a fundamental research, only a limited number of so called load sensors can be evaluated due to the limited scope of this work. It is not the aim of this work to conduct a comprehensive load evaluation of an entire wind turbine system, but to focus on aspects in which intermittency of wind can be of importance. Since longitudinal wind dynamics are in the focus of this work, the selected load sensors should be sensitive to these dynamics. As a counterexample, sensors like the in-plane (or strongly related edge-wise) blade root bending moment are dominated by gravitational forces in normal operation. A second requirement for the select load sensors is that they should target the main structural components of a turbine, namely the rotor including the blades and the tower. Thus the load sensors in the focus work are the

- Rotor Thrust,
- Rotor Torque,
- Blade **R**oot **B**ending **M**oment **O**ut **O**f **P**lane (RBMOP) and
- **T**ower **B**ase **B**ending **M**oment **F**ore-**A**ft (TBMFA).

In the fatigue calculation, the rotor thrust and torque where treated as drive train loads and associated with a Wöhler exponent $m_{\text{DrvTrn}} = 8$. For the RBMOP and TBMFA coefficients of $m_{\text{BlD}} = 12$ and $m_{\text{Tow}} = 4$ were used, respectively.

Chapter 3

Wind field generation

In this chapter the wind field generation process and its underlying strategy are presented. A central point of this work is the isolation of the intermittency effect, which requires a method to generate wind fields with and without intermittency. Aside intermittency, these fields have the same features. By the measures of the IEC standard [6], all wind fields are equivalent. These properties are achieved by the utilization of the CTRW model proposed by Kleinhans [1], introduced in Sec 2.1.3.

The requirements for the isolation of intermittency as well as the utilized parametrization of the CTRW model and the resulting temporal dynamics are discussed in detail in Sec. 3.1. Since the isolation of intermittency puts challenging requirements on the wind fields, the fields were assembled from individual time series, for which these requirements could be achieved (they could not be achieved for entire fields directly from the CTRW model). In order to compose entire wind fields from those time series, simplified spatial correlations in the yz -plane are considered. These presented in Sec. 3.2.

In order to investigate the impact on a model wind turbine profoundly, multiple mean wind speeds within the operation range of the turbine have been tested. These are $6\frac{m}{s}$, $9\frac{m}{s}$, $12.5\frac{m}{s}$, $15\frac{m}{s}$, $18\frac{m}{s}$, $22.5\frac{m}{s}$ and $25\frac{m}{s}$. In order to obtain results independent from Turbulence Intensity (TI), TI is 10% in all cases. In the rotor plane a spatial discretization of 31×31 equidistant grid points is used, spanning an area of $135m \times 135m$ covering the rotor area. This results in a mesh size of $dy = dz = 4.5m$, which is approx. the size of a discretized blade segment dr in the utilized wind turbine model. Commonly ten minute wind samples are considered as the mean wind speed is assumed to be approx. stationary over this time span. However due to the high demand for data in order to resolve the intermittent statistics reasonably, stationary time series of the length of one hour are considered in this study. The sampling frequency of each data set is $f_s = 20\text{Hz}$. We assume the most relevant time scales of wind dynamics to the wind turbine system to be captured with this sampling frequency. As a consequence the smallest increment lag value within this study is $\tau_{\min} = \frac{1}{f_s} = 0.05\text{sec}$. For each type of field, ten realizations have been generated for each wind speed tested in this study. For the sake of simplicity the fields are uniform meaning they do not feature a shear profile.

3.1 Wind time series

In this section the temporal statistics of the wind fields are discussed. They are the result from a close collaboration with Sebastian Ehrich. In order to evaluate the impact of different wind velocity increment statistics, time series $\vec{u}(t)$ with Gaussian and non-Gaussian (intermittent) increment statistics are generated and compared. In order to investigate the impact of increment statistics exclusively one must isolate them: The wind time series need to be highly comparable with respect to other, lower order statistics. The following parametrization of the CTRW model, which has been found in an extensive parameter study, have been used:

$$u_0^{(x)} = \{6, 9, 12.5, 15, 18, 22.5, 25\} \frac{m}{\text{sec}} \quad (3.1)$$

$$u_0^{(y)} = u_0^{(z)} = 0 \frac{m}{\text{sec}} \quad (3.2)$$

$$\gamma \approx 1.6595 \omega_S \quad (3.3)$$

$$\gamma_r \approx 0.2150 \omega_S \quad (3.4)$$

$$D_r = 0.1921 \omega_S \sigma^2 \quad (3.5)$$

$$D_i = 0.3468 \omega_S \sigma^2 \quad (3.6)$$

$$\omega_S = 1.8 \frac{1}{\text{sec}} \quad (3.7)$$

$$\sigma = 0.1 u_0^{(x)} \quad (3.8)$$

$$C = 350 \text{ sec} \quad (3.9)$$

$$\alpha_{\text{Gau.}} = 1 \quad (3.10)$$

$$\alpha_{\text{int.}} = 0.65 \quad (3.11)$$

$$\alpha_{\text{mod.}} = 0.8 \quad (3.12)$$

Note that between the intermittent and Gaussian wind type, only the parameter α changes, which is critical for the mapping process, see Sec. 2.1.3. As a consequence, the resulting fields are highly comparable. In the following, the properties of the resulting time series are discussed in detail and step-by-step.

3.1.1 One Point (1P) statistics

The amplitude of wind fluctuations $u' = u - \bar{u}$ is scaled by the wind's variance, which normalized by the mean wind speed is the TI, wherefore these have to be equivalent between both types of wind fields. Examples of time series for the main flow component $u(t)$ are given in Figs. 3.1a for the Gaussian type and 3.2a the intermittent type, respectively. It has assured that the mean wind speed and TI are equivalent between both types. Furthermore, as shown in Figs. 3.1b and 3.2b, we achieve Gaussian velocity fluctuations $u'(t)$ for both types.

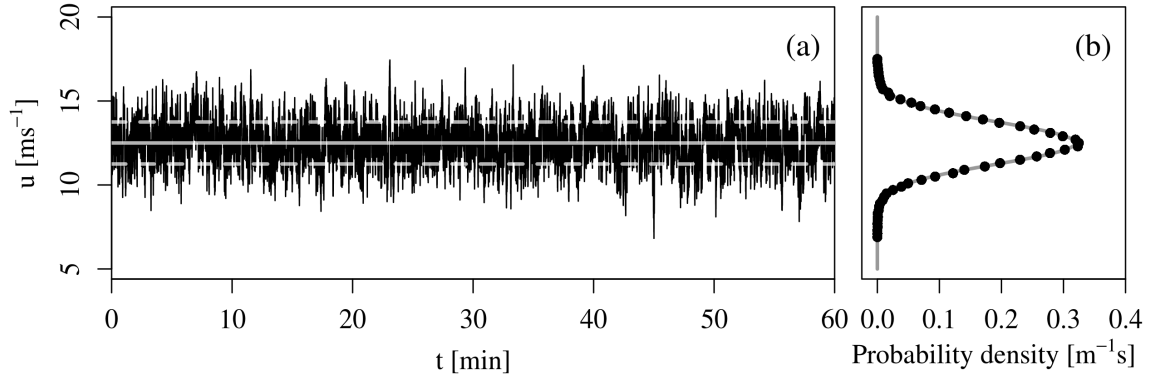


Figure 3.1: Exemplary *Gaussian* wind time series. (a) Main wind velocity component $u(t)$, including mean ± 1 standard deviation (dashed lines). (b) Corresponding histogram and Gaussian fit.

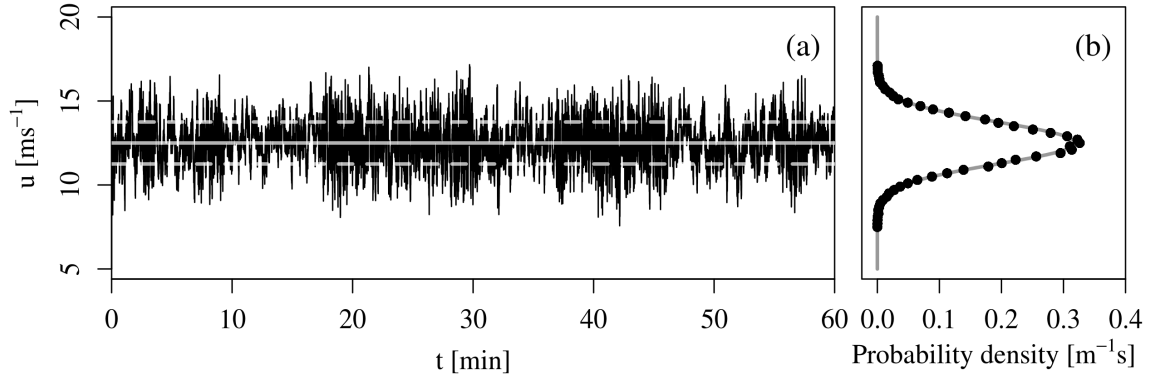


Figure 3.2: Exemplary *intermittent* wind time series. Analogous to Fig. 3.1.

In order to quantify the agreement between in the 1P statistics, the error ε

$$\varepsilon_n = \mu_n(X_{Gauss}) - \mu_n(u(t)) \quad (3.13)$$

is considered. It quantifies the difference in the central moments between the generated velocity signal $u(t)$ and a pure Gaussian process. It is shown in Fig. 3.3. As can be seen, all realizations (Gaussian and intermittent) deviate in all central moments with less than $\varepsilon < 10^{-3}$, which documents the high comparability between all types of wind time series with respect to their 1P statistics.

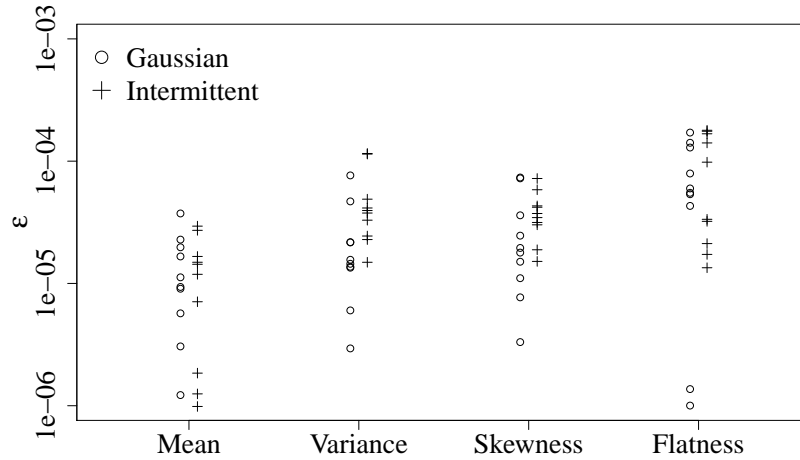


Figure 3.3: Error ε_n cf. Eq. (3.13) in ten intermittent and ten Gaussian realizations of wind time series obtained with the CTRW.

3.1.2 Two Point (2P) statistics

In this section the 2P statistics of the generated velocity signals are considered. As discussed before the differences between both types of wind fields due to intermittency, are evident only in the fourth (and higher) moments of the 2P statistics.

The first statistical moment of the increments is approx. zero for all time series. This lies in the nature of a stationary process. The second moment needs to be discussed in greater detail. It essentially carries the same information as the the Auto Correlation Function (ACF)

$$\rho(\tau) = \frac{r_{u'u'}(\tau)}{\text{VAR}[u']} = \frac{E[u'(t)u'(t+\tau)]}{\text{VAR}[u']}. \quad (3.14)$$

The ACF represents how far wind structures extend in a given dimension, wherefore it is an important property. Fig. 3.4 shows $\rho(\tau)$ for both, all intermittent and all Gaussian realizations. Aside from some scattering in the weakly correlated regime, a high agreement among all realizations is evident.

Via the *Wiener-Khinchin Theorem*, see Eq. (2.17), the ACF is related to the power spectrum

$$S_{xx}(f) = |\hat{x}(f)|^2 \quad \text{with} \quad \hat{x}(f) = \int_{-\infty}^{+\infty} e^{-2\pi ift} x(t) dt. \quad (3.15)$$

As mentioned in Section 2.1.2, is often focused on to model wind fields. Fig. 3.5 shows the power spectral density of $u'(t)$ for both types of fields. Note that the intermittent spectrum has been shifted vertically for the sake of better representation. As expected from the auto-correlations both types are described by highly comparable spectra. Also, within the frequency range $10^{-1} < f < 10^0$ the spectra roughly follow a $-\frac{5}{3}$ -trend, as postulated by Kolmogorov in 1941 (K41) [3].

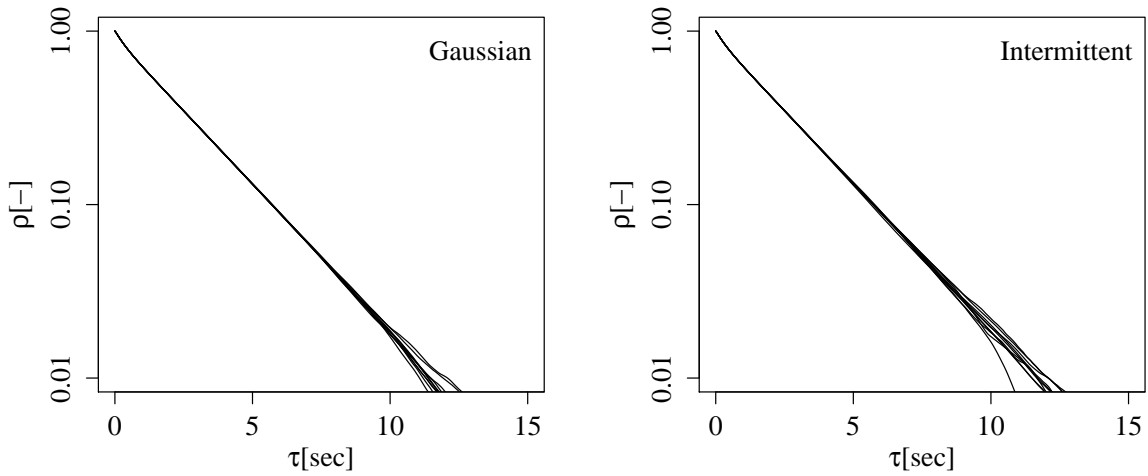


Figure 3.4: Correlation coefficient ρ over lag value τ for ten Gaussian and ten intermittent realizations.

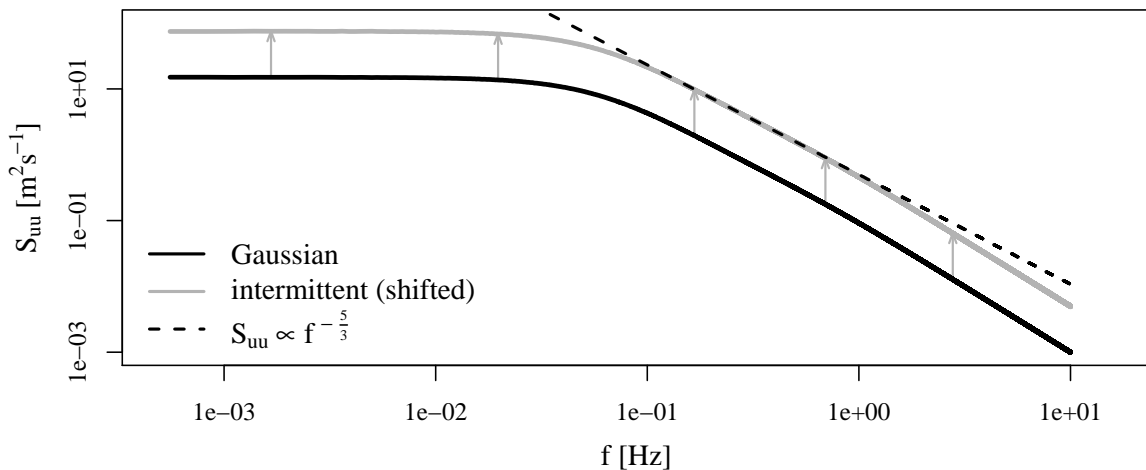


Figure 3.5: Power Spectral Density (PSD) S_{uu} for the main wind velocity component $u(t)$ for the *Gaussian* and *intermittent* field type. Note that the intermittent spectra is shifted by a factor of five for better representation. The length of the arrows correspond to the distance of the shift. The dashed line represents a $-\frac{5}{3}$ slope relevant to K41.

Since the second order 2P statistics (and lower statistics) are equivalent for all time series used in this work, these time series – according to standard guidelines – should not lead to significantly different wind turbine loads. However the time series become distinguishable when higher order statistics are considered. A starting point are the PDFs of the 2P statistics, which are displayed in Fig. 3.6. The histograms of wind velocity increments δu_τ for $\tau = \{0.05, 0.1, 2\}$ are shown in Fig. 3.6a. A deviation from an ideal Gaussian process is evident for the *intermittent* data set obtained with $\alpha_{\text{int.}}$. The deviation is dependent on the time lag τ between the two

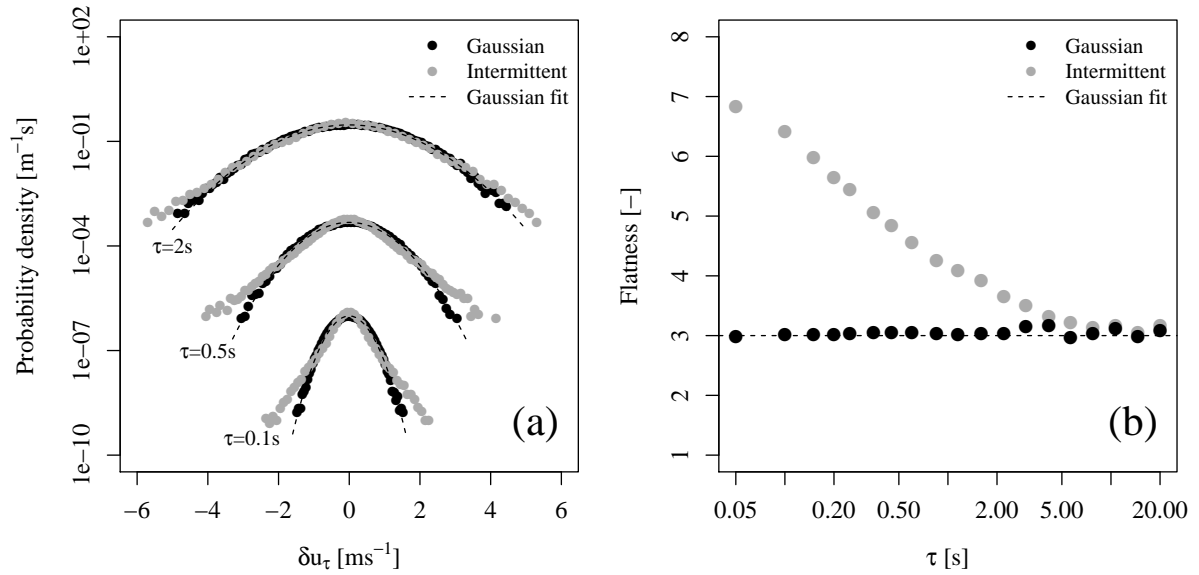


Figure 3.6: Comparison of the two-point statistics for the *Gaussian* and *intermittent* fields. (a) Histograms of velocity increment time series for $\tau = 0.1s, 0.5s, 2s$. (b) Flatness of increment PDFs in the range $0.05s \leq \tau \leq 15s$.

points considered. In order to describe the scale dependency and the deviation from an ideal Gaussian PDF, Fig. 3.6b represents the fourth moment (alias flatness or kurtosis) of increment PDFs in dependence of τ . As can be seen, the increment statistics of the *intermittent* data sets deviate from a Gaussian process in the range $\tau < 10s$. In conclusion, the frequency range of interest $0.2\text{Hz} < f < 5\text{Hz}$ features a reasonable intermittency.

The fourth moment of the 2P statistics is the lowest order statistic in which differences between the two types of fields are evident. In order to quantify the non-Gaussianity of the presented time series a comparison of ten intermittent realizations against measurement data is displayed in Fig. 3.7. It can be seen that the generated, synthetic wind data has fourth order two-point statistics similar to stationary wind measurements. Note that these $F(\tau)$ is not known a priori the generation process. The current parametrization was obtained from experience with the model extensive parameter testing. It yields a convincingly non-Gaussian trend of $F(\tau)$ over a wide range of τ . The utilized reference measurements are:

- Unconditioned offshore wind measurement data from FINO1 [35] in the month of January 2006, sampled with 1Hz , so that the smallest value for $\tau_{\text{Fino, min.}} = 1 \text{ sec}$ [35, 34]
- Conditioned FINO data. Only wind speeds in the range $6 \pm 0.5 \frac{m}{s}$ from the aforementioned data set are considered in order to achieve stationary conditions [34]
- Measurement of y cylinder wake under laboratory conditions [59, 11]
- Conditioned measurement of atmospheric turbulence near the shore in North-Western Germany. Only velocities in the range $4.5 - 5.6 \frac{m}{s}$ are considered [14, 11]

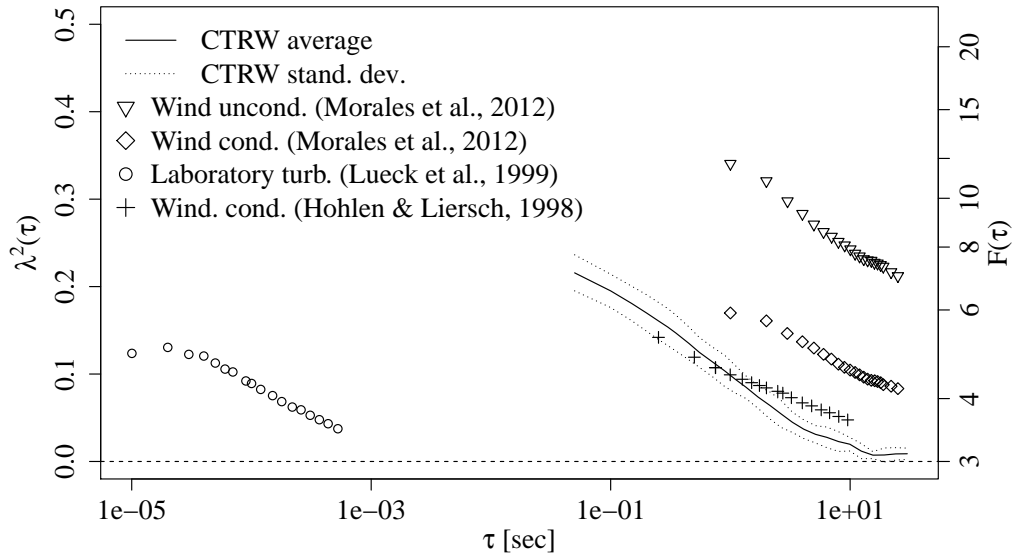


Figure 3.7: Scaling behavior of 2P statistics of different sources. *Lines*: Ensemble of ten CTRW realizations. *Triangles*: Unconditioned Wind data from FINO platform, taken from Ref. [34]. *Diamond*: Conditioned wind, taken from Ref. [34]. *Circles*: Laboratory turbulence obtained in measurement [59], taken from Ref. [11]. *Crosses*: Conditioned wind measurements [14], taken from Ref. [11].

3.2 Assembly of wind fields

The isolation of intermittency could be achieved for individual time series $u(t)$. However, a proper load simulation requires spatially resolved wind velocity vector fields $\vec{u} = \vec{f}(y, z, t)$. In common wind field generation algorithms like the Sandia Method [39], these fields are constructed from a spectrum and a coherence models. The velocity time series at a given grid point will feature correlated power spectral densities with randomized phase information. However this approach is not suitable for the task at hand, since the postulated requirements for the wind time series are not explicitly constrained within this method. Therefore, other approaches for the construction of wind fields need to be explored. They are presented in this section. Three approaches have been utilized, which aim to represent three different levels of complexity.

3.2.1 Full correlation and delta correlation

As a first simple approach, two very simple cases are considered: They are referred to as the *fully correlated* and the *delta correlated* case. For the fully correlated case, each of the 31×31 grid points will have the exact same time series. This corresponds to a stationary, complete correlation in space over the entire rotor area. On the the contrary, the delta correlated case will feature completely uncorrelated time series in each of the grid points. Examples for the resulting fields are given in Fig. 3.8.

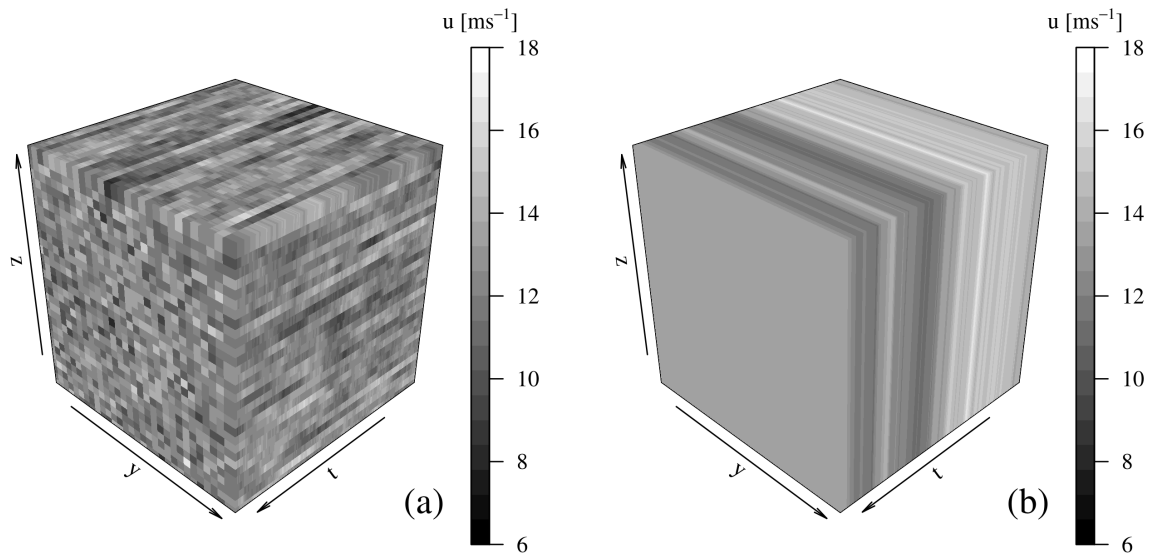


Figure 3.8: Exemplary visualization of the flow field excerpts for a mean velocity in main flow direction of $u = 12.5 \frac{m}{s}$. (a) *Gaussian* type, delta correlated in space. (b) *Gaussian* type, fully correlated in space.

Both types of fields can be assembled from Gaussian or intermittent time series. The motivation to consider these simplified scenarios is the following: The fully correlated case is the most sensitive to the longitudinal wind dynamics, as no other dynamics will distort them. All the dynamics can be considered as synchronized and thus their impact on the wind turbine should be the strongest. In conclusion, if an impact of the intermittent temporal dynamics is not evident in the fully correlated case, it is unlikely to be found in any wind field. The delta-correlated case represents the other extreme. Here, all longitudinal wind dynamics are de-synchronized. If an impact of intermittency would be evident in this case, this means it would be evident in all types of wind fields. Obviously, both cases are highly idealized scenarios. A realistic wind field will feature neither fully, nor a delta-correlated dynamics, but have a finite correlation length and will therefore be ‘in between’ both of these extreme cases. As an example, common integral length scales of atmospheric boundary layer flows can be in the order of several hundred meters [60].

3.2.2 Subdivided fully correlated fields

Since the two extreme scenarios introduced in the previous section In order to fill the gap between the two extreme scenarios introduced in the previous section, an intermediate approach is considered. A simplistic attempt to incorporate the concept of finite spatial correlations is to subdivide the wind field’s spatial 31×31 yz -grid into an $n \times m$ grid with $\frac{31}{n}$ or $\frac{31}{m}$ grid points, respectively. In all of the sub-grid’s points, fully correlated fields are prescribed. In doing so, one achieves unrealistically regular structures, whose length scales can be easily quantified by n and m and the given mesh size. Practical examples are $n = m = \{2, 3, 4, \dots\}$. Exemplary fields are shown in Fig. 3.9.

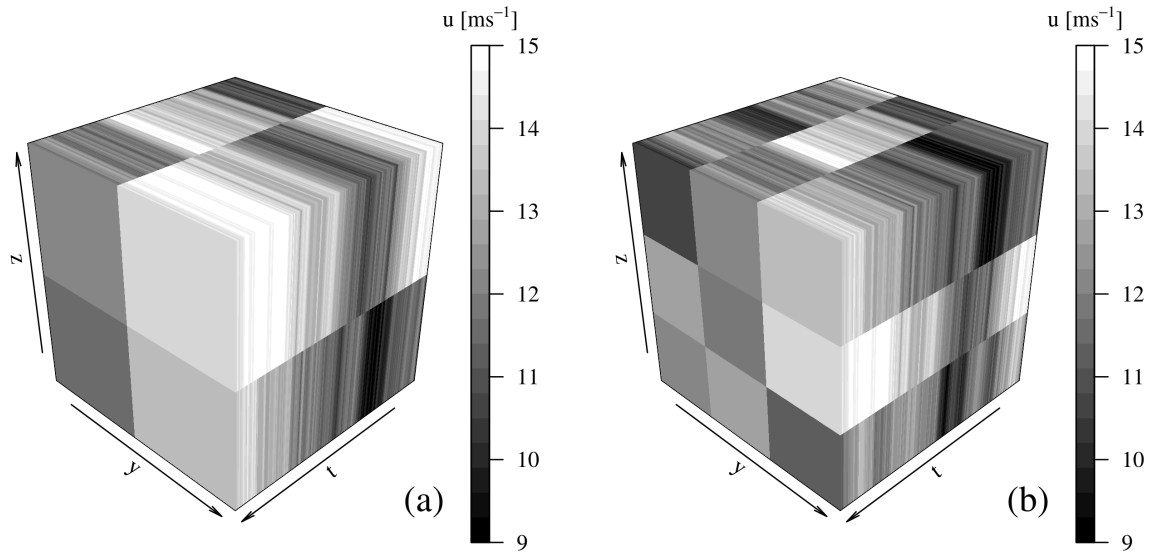


Figure 3.9: Exemplary visualization of subdivided fully correlated fields at $u = 12.5 \frac{\text{m}}{\text{s}}$. (a) Sub-division into 2×2 . (b) Sub-division into 3×3 .

3.2.3 Stationary coherent structures

While the aforementioned approaches are relatively easy to implement, they have the drawback that the resulting structures are regularized and of the same size, which can lead to unrealistic periodicities in the wind turbine response. This however disagrees with the classic representation of turbulence as a process on multiple scales, cf. Sec. 2.1.1. In order to obtain more realistic, randomly shaped and sized structures, representations of a geostatistical model is utilized. Field realizations of of this model are then utilized to shift the time series of a fully correlated grid against each other. Depending on the size of structures and the amplitude of the shift, a multitude of coherent structures are generated. For prescribing the dynamics in a spatial, two-dimensional space, a so called variogram (sometimes semivariogram) [61] is considered.

A variogram is the representation of the semi-variance γ of a spatially varying quantity z between two points in dependence of the lag value d , so that the semi-variance γ

$$\gamma(d) = \frac{1}{2} \frac{1}{n} \sum_{i=1}^n (u(x_i) - u(x_i + d))^2. \quad (3.16)$$

As can be seen from Eq. (3.16) the semivariance classifies as 2P statistic and is of second order (like the ACF). In this work realizations of a two-dimensional field with different Gaussian variograms are considered. A variogram is characterized by three numerical parameters and a type description, the

- Nugget $\tilde{n} = \gamma(d = 0)$,
- Sill $\tilde{s} = \gamma(d \rightarrow \infty)$,
- Range d_r with $\gamma(d_r) \approx \tilde{s}$ or $\gamma(d_r) = \tilde{s}$ (depending on type) and
- Type: The distribution of γ between $0 < d < d_r$. Examples of typical types are Gaussian, linear or exponential.

In this work a Gaussian type is selected. The selection of a Gaussian type may be arguable, however on the coarse grid this type yielded the most physical results. An exponential model was tested as well, but lead to highly decorrelated dynamics. The corresponding Gaussian variogram is described by

$$\gamma(d) = (\tilde{s} - \tilde{n}) \left(1 - \exp\left(\frac{-3d^2}{d_r^2}\right) \right) + \tilde{n} \quad (3.17)$$

so that a semi-variance of approx. 95% of \tilde{s} is reached at d_r for $\tilde{n} \ll \tilde{s}$

$$\gamma(d_r) \approx 0.95(\tilde{s} - \tilde{n}) + \tilde{n}. \quad (3.18)$$

Further testing lead to the following parametrisation: The nugget is aimed to be $\tilde{n} = 0$. However, due to technical details $\tilde{n} = 10^{-4} \approx 0$. It was found that $\tilde{s} = 10$ gives a convenient amount of variation in the field. The range value d_r takes different fractions of the rotor radius R in order to obtain fields with differently sized structures. Some of the utilized variograms are shown in Fig. 3.10.

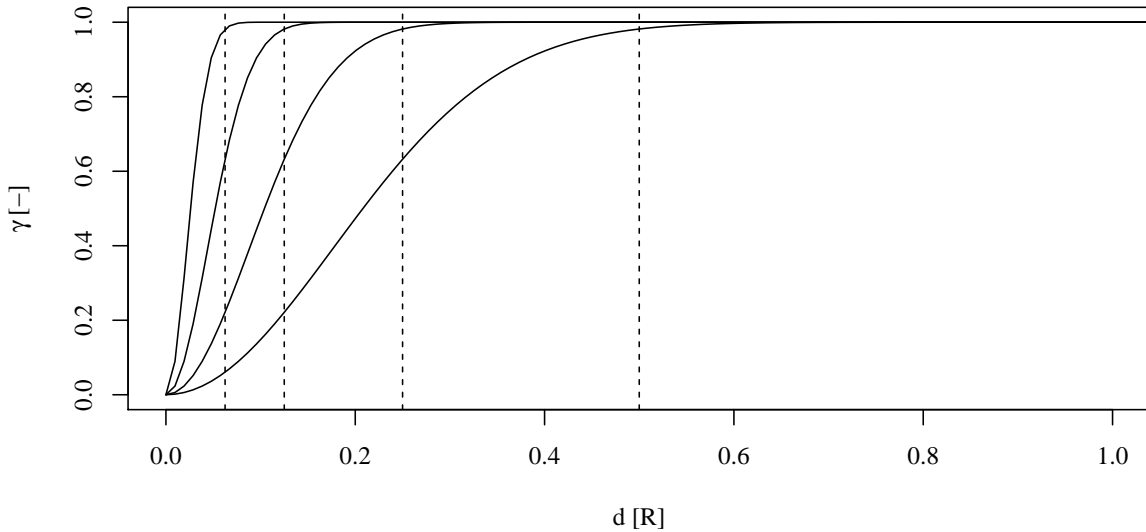


Figure 3.10: Exemplary semivariance γ for $\tilde{s} = 1$ and $\tilde{n} = 0$ against lag in rotor radius R for $d_r = \{\frac{1}{2}, \frac{1}{4}, \frac{1}{8}, \frac{1}{16}\}R$

Field realizations governed by these variograms are used as discrete two-dimensional 31×31 field in order to shift all 31×31 time series of a fully correlated grid in the domain. In conclusion the shift values $\tilde{t}(y, z)$ are in the unit of time. An important scaling parameter is the overall magnitude of the shift. It needs to be put into context with the correlation time t_{corr} , which quantifies for how long a velocity signal $u(t)$ is correlated with itself. As shown in Fig. 3.4 we can approximate $t_{\text{corr}} \approx 12$ sec. In conclusion a shift of $\tilde{t}(y_n, z_m) > 12$ sec would decorrelate two neighboring velocity signals $u(t, y = y_n, z = z_m)$ and $u(t, y = y_{n+1}, z = z_m)$ entirely.

In order to remain correlation, the ensemble mean of $\tilde{t}(y_n, z_m)$ was set to $\langle \tilde{t} \rangle = \frac{t_{\text{corr}}}{4}$. Since all time series were generated with additional buffer lengths due to technical requirements of the wind turbine simulation tool, the shift could be realized without creating discontinuities at the beginning or ending in the resulting time series. Examples of the so generated patches are shown in Fig. 3.11. The resulting picture exhibits coherent spots that are not moving in the yz -plane. Therefore this approach is referred to as the approach of *stationary coherent structures*. Visualizations of the resulting fields are shown in Fig. 3.12.

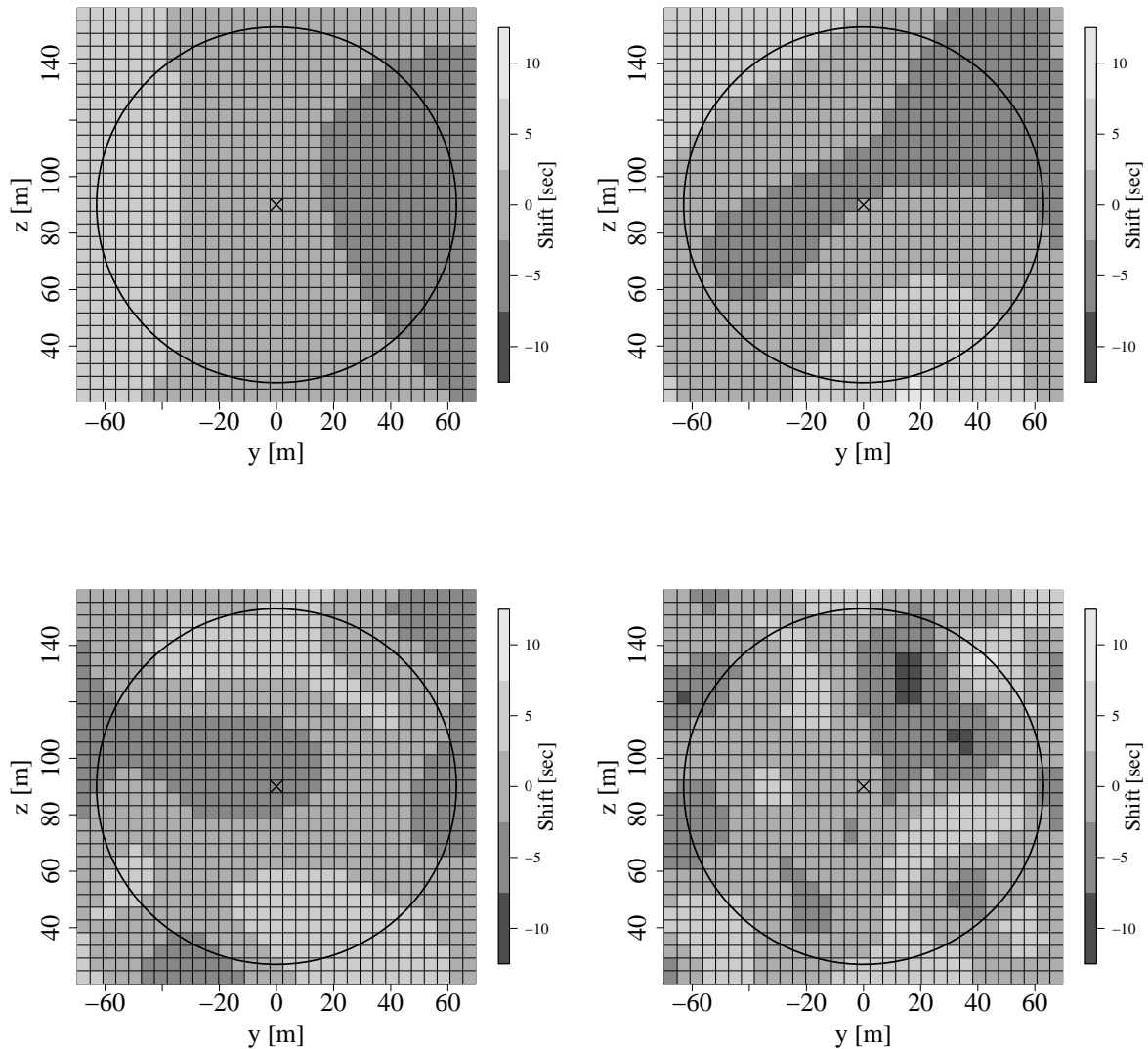


Figure 3.11: Exemplary visualizations of plains used for shifting the time series of fully correlated fields. Variograms feature $\tilde{s} = 10$ and $\tilde{n} = 10^{-4}$ and $d_r = \{\frac{1}{2}, \frac{1}{4}, \frac{1}{8}, \frac{1}{16}\}R$

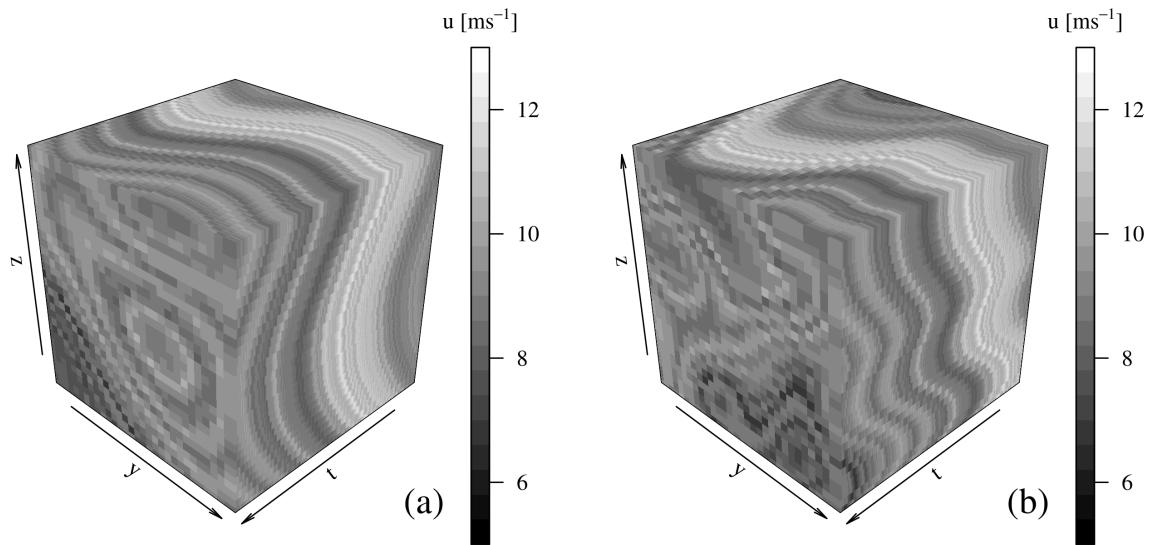


Figure 3.12: Visualization of exemplary flow fields obtained with the approach of stationary coherent structures. (a) $d_r = \frac{1}{4}$. (b) $d_r = \frac{1}{8}$.

The need for spatially varying correlations can be satisfied with the outlined model and model parametrization, as it delivers coherent velocity structures in the rotor plane. In contrast to standard wind models, the location and size of these structures do not change in this approach. If one would implement a movement of these structures (e.g. by interpolation between different shift matrices) the time history at a fixed observation point changes in a non-trivial way. Additionally, interpolation might alter the properties of the time series, which must be avoided in the context of this work. Lastly, due to the rather coarse spatial resolution of the wind field, non-Gaussian dynamics are not considered in the spatial dynamics. Therefore, intermittency is only modelled in the longitudinal wind dynamics.

Chapter 4

The intermittency effect for fully correlated wind fields

In this chapter wind turbine load responses to wind fields with Gaussian and non-Gaussian increment statistics are compared against each other. From Sec. 3.1 we recall that all wind fields are designed in a way, so that all differences between them can directly be attributed to the effect of intermittency. At the beginning of this discussion, the focus is on fully correlated wind fields, since a potential intermittency effect is assumed to be most evident in this scenario due to the synchronization of the longitudinal wind dynamics. At first the results obtained with the AERO model are analyzed. Several different aspects are discussed in order to investigate the results profoundly: Initially, standard fatigue loads by means of EFL values are presented in Sec. 4.1. The observed intermittency effect for this case is subsequently analyzed more deeply by an investigation into the underlying scales and load ranges in Sec. 4.2. Further approaches to analyze the load signals, namely spectral and increment analysis, are briefly discussed and compared in Sec. 4.3. The discussion of results obtained with the AERO model only take into account the aerodynamic response and exclude elastic deformations and controller dynamics. These results are rather fundamental, but necessary in order to understand how intermittency affects wind turbines. In order to examine whether the observed trends also hold for a more complex ASE model a, dedicated set of simulations has been carried out. The results are shown in Sec. 4.4. A summary of the conclusions that can be drawn from the presented results is given in Sec. 4.5.

4.1 Equivalent fatigue loads

The analysis of the results aims to be in accordance with industrial practice. Therefore Equivalent Fatigue Loads (EFLs) are calculated, see 2.3. Fig. 4.1 shows the EFL values for the rotor thrust. In Fig. 4.1a the absolute EFL values are plotted against the mean wind speed. Fig. 4.1b shows the relative EFL values, which have been normalized by the Gaussian results so that the ensemble mean EFL for the Gaussian results equals 100% at a given wind speed. The ensemble means are represented by dashed lines. As a rough trend, an overall increase in EFL in the order of 5% can be observed for the intermittent fields. The shaded regimes around the averages represents the corresponding ensemble standard deviation and give an indication of the amount

of scatter. A peak at $9 \frac{m}{s}$ is evident. Additional calculations indicate that this peak is related to unsteady aerodynamics and dynamic stall modeling in the inner part of the rotor blade. More details are given in a dedicated section below.

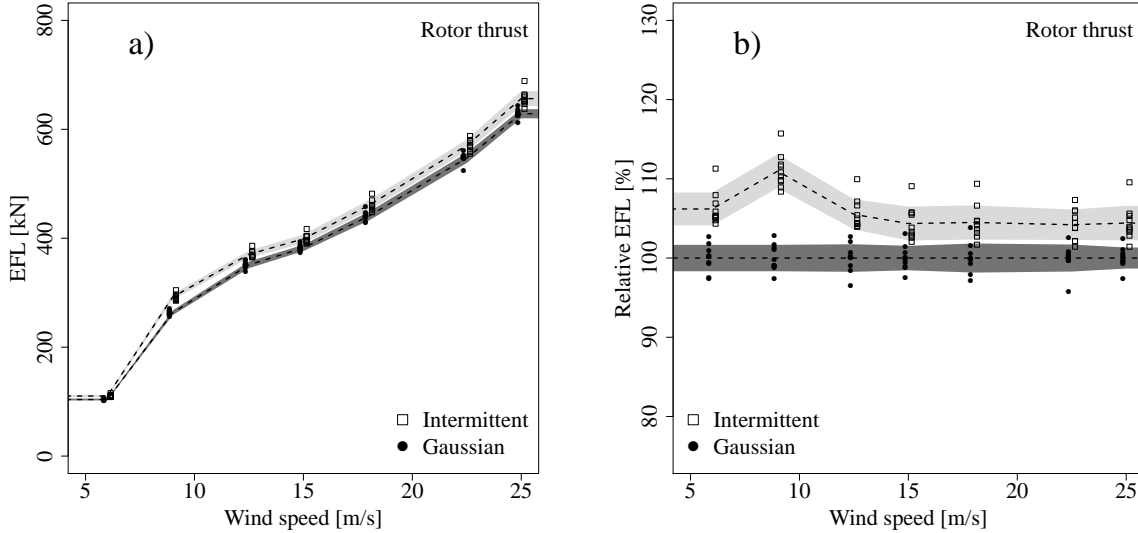


Figure 4.1: EFL (see Eq. (2.47)) for the rotor thrust for all realizations and all wind speeds for the *fully correlated* case with the AERO turbine model. The data points are shifted horizontally for a better discrimination between *intermittent* and *Gaussian* data. The dashed lines represent averages, the shaded area covers \pm one standard deviation around the average. (a) Standard representation. (b) Data normalized with the average of the *Gaussian* result (Gaussian averages correspond to 100%).

Fig. 4.2 shows the corresponding results for the rotor torque. For the most part, the results are comparable to those shown in Fig. 4.1. However the peak at $9 \frac{m}{s}$ is not evident, which is discussed below in a section dedicated to the impact of unsteady aerodynamic models. In summary the rotor torque results show an increase in fatigue loads comparable to the rotor thrust of approximately 5% and a comparable amount of scattering.

The results for the blade Root Bending Moment Out of the rotor Plain (RBMOP) are shown in Fig. 4.3. The dynamics of the RBMOP are different from all other three load sensors, since they stem from the rotational sampling with only one blade. All other load channels of interest (thrust, torque, tower bending moment) rely on rotational sampling based on all of the three blades. Due to the reduced amount wind field sampling done by an isolated blade, a less clear, more scattered picture could be expected for this sensor. This seems to agree with the results, as the scattering for the RBMOP is slightly larger as in other sensors, for instance at $15 \frac{m}{sec}$. Nevertheless, the general difference between intermittent and Gaussian dynamics is also evident.

The results for the Tower Base Bending Moment in Fore-Aft direction (TBMFA) are displayed in Fig. 4.4. They are – as expected – comparable to the results obtain for the rotor thrust in Fig. 4.1, since the thrust is the driving force behind the TBMFA.

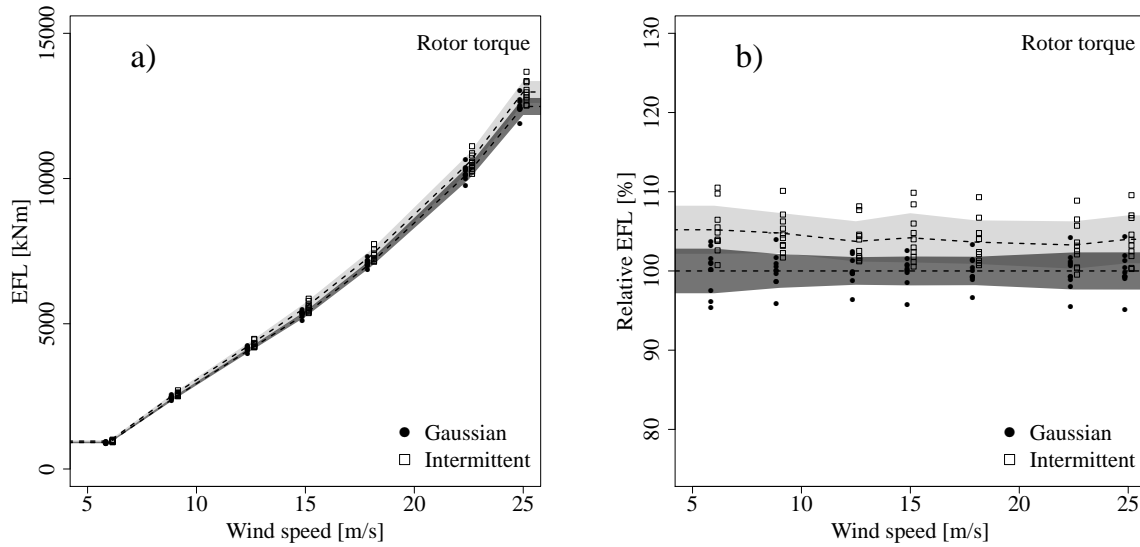


Figure 4.2: EFL for the rotor torque for the *fully correlated* case with the AERO turbine model. Analogous to Fig. 4.1.

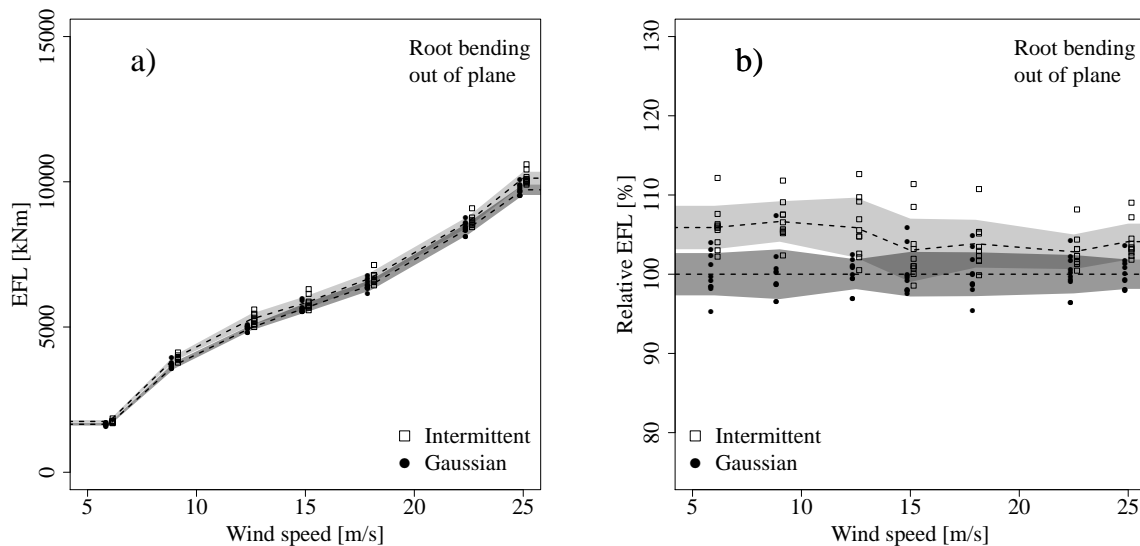


Figure 4.3: EFL for the Root Bending Moment Out of Plane (RBMOP) for the *fully correlated* case with the AERO turbine model. Analogous to Fig. 4.1.

Validation with moderately intermittent fields

So far it seems that the intermittent wind fields lead to increase EFL values in all load sensors. In order to support this conclusion additional wind fields with a weaker non-Gaussianity have been tested. The fields are designed to feature about half the non-Gaussianity of the intermittent fields. As mentioned in Sec. 2.1.3 the underlying value for the CTRW mainly responsible for the non-Gaussianity is α . For this case it has been set to $\alpha_{\text{mod.}} = 0.8$ so that $\alpha_{\text{int.}} = 0.65 < \alpha_{\text{mod.}} < \alpha_{\text{Gau.}} = 1$. For reference Fig. 4.5 shows a characterization of these moderately intermittent dynamics by means of λ^2 values.

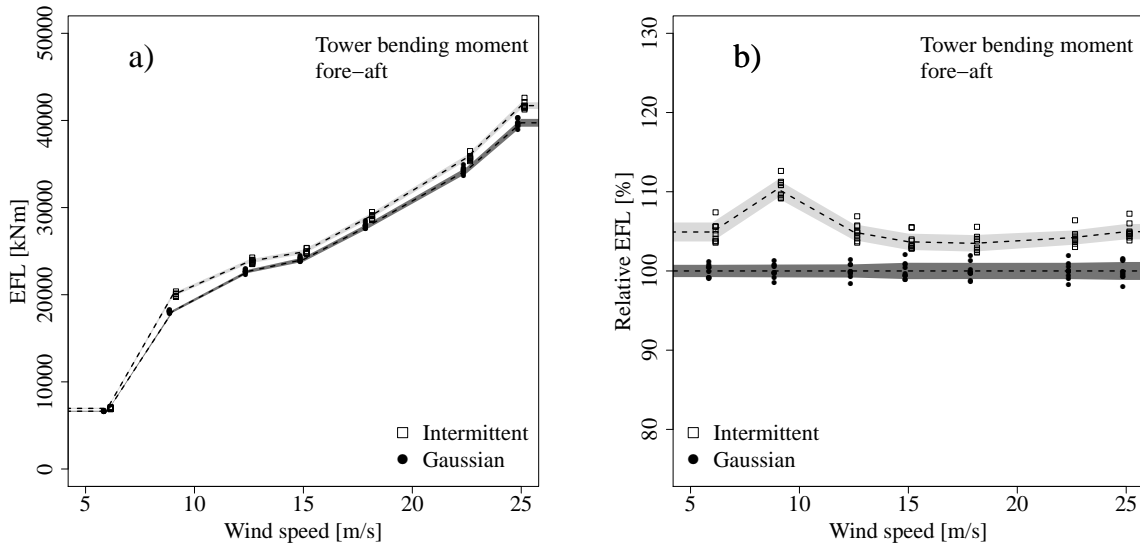


Figure 4.4: EFL for the Tower base Bending Moment Fore-Aft (TBMFA). Analogous to Fig. 4.1.

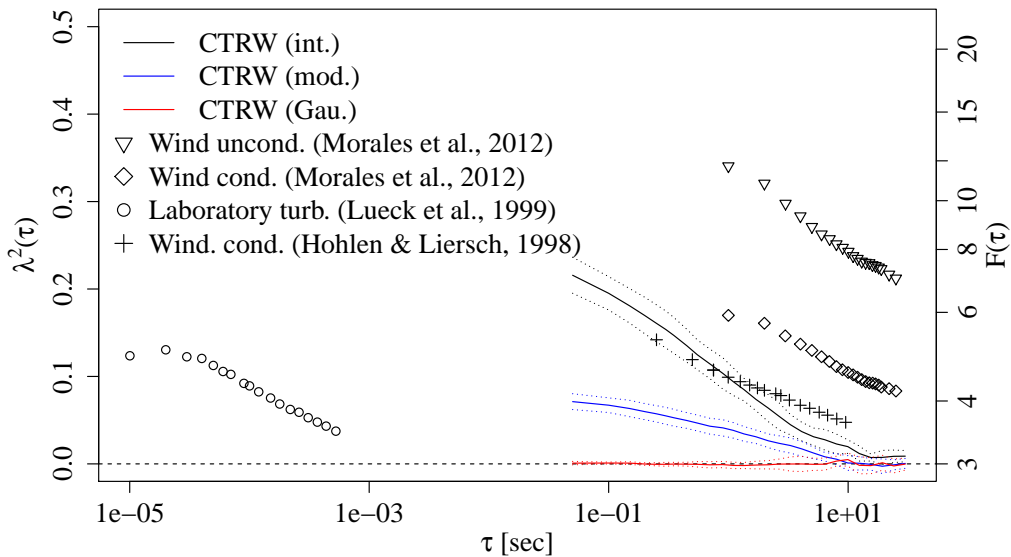


Figure 4.5: Scaling behavior of 2P statistics of different sources, including intermittent, moderately intermittent and Gaussian CTRW data. Analogous to Fig. 3.7.

Fig. 4.5 shows the results for these fields. The moderately intermittent data set lines up in between the Gaussian and intermittent results. For the sake of brevity, only the rotor thrust is shown here. The other load sensors showed similar findings. These results underline the relation between the non-Gaussianity of the wind velocity increments to the EFL values for the fully correlated wind fields.

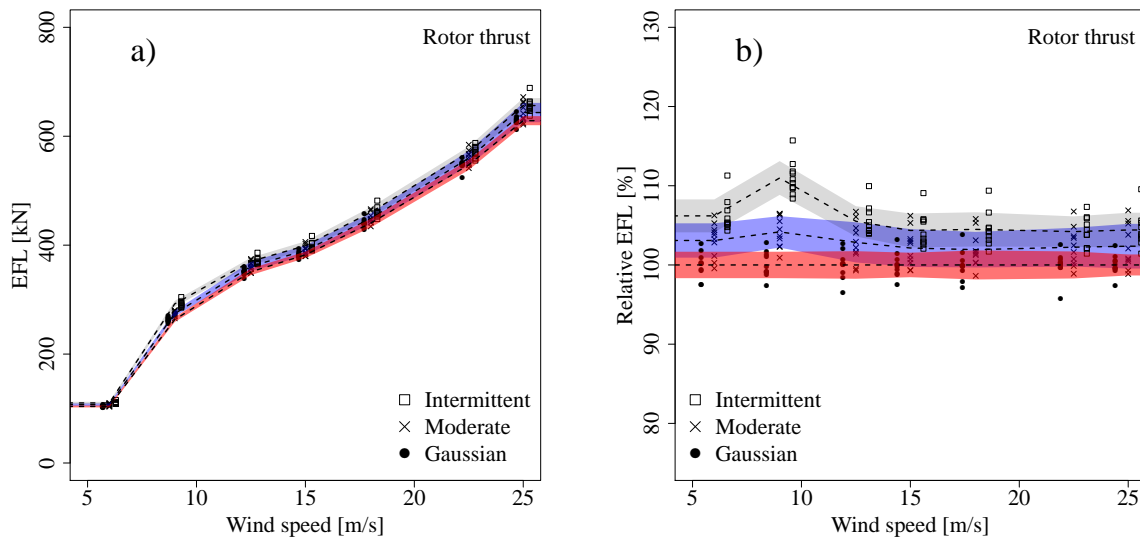


Figure 4.6: EFL for the rotor thrust including a moderately intermittent wind field type. Analogous to Fig. 4.1.

On the impact of unsteady aerodynamics

The results obtained at $9\frac{m}{s}$ for the rotor thrust, see Fig. 4.1, and the TBMFA, see Fig. 4.4 seem to stand out, as the difference between Gaussian and non-Gaussian fields seems to significantly larger. A deeper investigation gives evidence that this stems from unsteady airfoil responses and dynamic stall modeling in the blade root region.

Around a wind velocity of $9\frac{m}{s}$ the rotor operates in its most aggressive aerodynamic operation point so that the aerodynamic profiles are operating very next to their respective stall angles. These operations points are prone to perturbations like turbulence. Under turbulent inflow it is possible that flow separation may occur, which comes along with a drop in glide ratio (lift to drag ratio). Typically the root region is subject to high angles of attack and prone to stall.

The rotor thrust is the sum of all axial forces on the rotor blades. Under dynamic stall, large load hysteresis on both the axial and circumferential can occur. However, these are represented very differently in the selected load sensors: The rotor thrust is the sum of all axial forces on the rotor blades, wherefore a change in axial force at an arbitrary blade segment directly leads to a change in thrust. As mentioned above, the TBMFA is mainly driven by the thrust, wherefore its dynamics are similar. The rotor torque and the RBMOP however are calculated from sectional forces multiplied with the radius of the respective section. Therefore, dynamic force variations near the blade root (at a small radius) do not effect the torque or RBMOP profoundly. This explains, why a peak is evident for the thrust and TBMFA, but not for the torque and RBMOP.

To investigate the impact of unsteady aerodynamic models to the presented results, a comparison against another model is presented. We recall that a Beddoes-Leishman type unsteady airfoil model has been utilized in the presented results [47]. More precisely, the selected simulation tool applies a modified version following the work of Minema and Pierce; details maybe taken from Ref. [62]. Fig. 4.7 shows the very same simulation case with a different unsteady

aerodynamics model: The *DYSTOOL* model proposed by Gonzàles [63] has been deployed, which also bases on Ref. [47]. With the *DYSTOOL* model, the peak at $9 \frac{m}{s}$ increases up to roughly 15% and spreads out to neighboring pre-rated wind speeds in the range $6 - 12.5 \frac{m}{s}$.

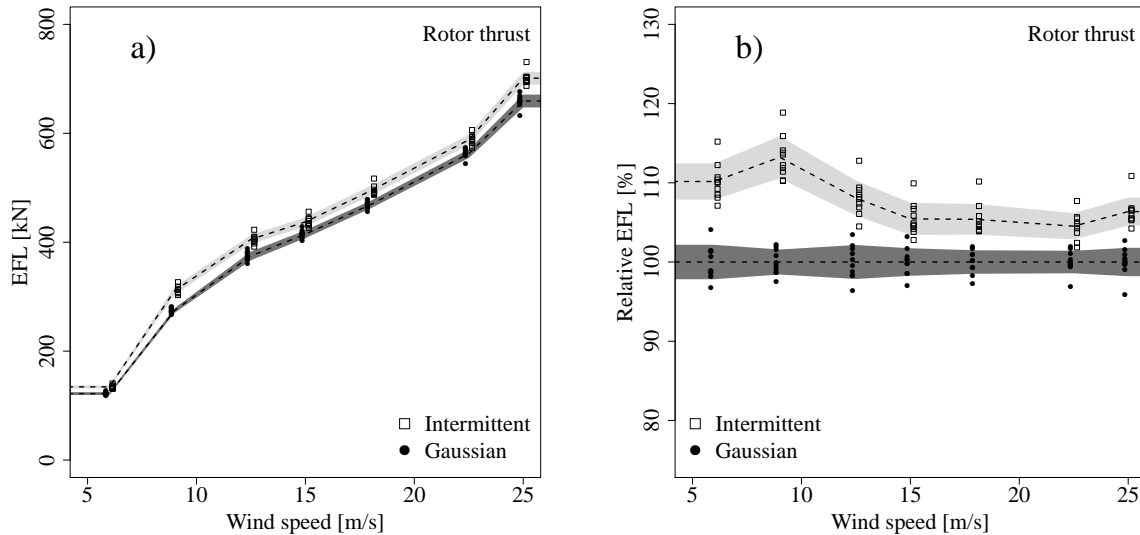


Figure 4.7: EFL for the rotor thrust based on the *DYSTOOL* model [63] for unsteady airfoil aerodynamics. Analogous to Fig. 4.1.

Fig. 4.8 shows the results obtained with no unsteady aerodynamics model, so that the calculation is strictly based on the stationary airfoil data. When unsteady airfoil aerodynamics are neglected the aforementioned peak vanishes and a level difference between intermittent and Gaussian wind fields in EFL is evident. These results clearly associate the peak at $9 \frac{m}{sec}$ with details of the unsteady aerodynamics modeling.

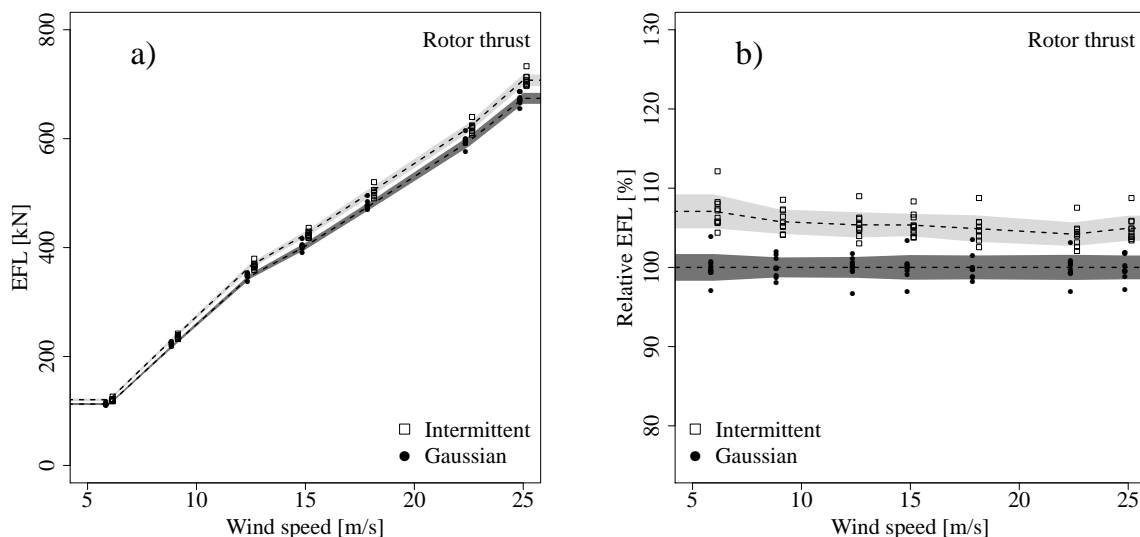


Figure 4.8: EFL for the rotor thrust based on steady airfoil aerodynamics. Analogous to Fig. 4.1.

4.2 A closer look at load ranges

In order to gain a deeper understanding of the EFL results presented in the previous section 4.1, the load (or stress) ranges S are investigated. We recall from Eq. (2.47) that the stress ranges S_i are the driver for the EFL values, as all other values are constants in the context of this study. The stress ranges are essentially temporal load increments $S_\tau = S_0(t + \tau) - S_0(t)$ on varying time scales τ from a given load time series $S_0(t)$. However within the RFC framework, the ranges are not calculated from load time series, but only from local load extrema of $S_0(t)$. As is evident from Eq. (2.47), the ranges are exponentiated with the Wöhler coefficient m and subsequently summed up. The resulting sum only needs to be normalized by a simulation time T and re-scaled to intuitive physical dimensions by exponentiation with $\frac{1}{m}$ in order to yield the EFL. In conclusion, the stress ranges S are of high interested and are therefore evaluated in the following.

At first, a scenario with well pronounced differences in the EFL result is analyzed: The focus is on one exemplary realization of the TBMFA at $9 \frac{m}{sec}$. The trends observed for this realization are representative for the entire ensemble. Fig. 4.9 shows the stress ranges S against the time scale τ they occur on. Note that the wind signal, which is the origin of these loads, becomes uncorrelated at approx. $\tau = 12$ sec, as discussed in Sec. 3.1. It is evident that the intermittent case features larger values of S over a wide range of τ . As a qualitative take-away from this form of presentation, it becomes evident that the spread of S at a given τ seems to be larger for the intermittent case.

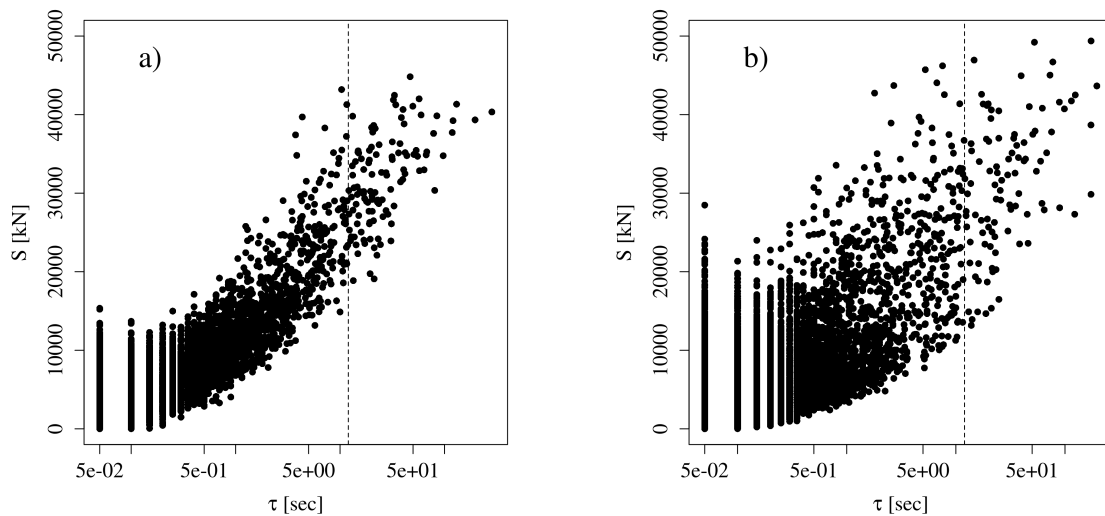


Figure 4.9: Stress ranges $S(\tau)$ for realization 001 of the TBM FA at $9 \frac{m}{sec}$. a): Gaussian, b): Intermittent. The dashed line from represents $t = 12$ sec.

The highest values of S are contributing most the EFL, since they are exponentiated with the Wöhler coefficient, see Eq. (2.47). From Fig. 4.9 it becomes evident that these largest values are found exclusively on large time scales. This can be explained as follows: As outlined in Sec. 2.3.3 within the RFC procedure range pairs are searched for and removed from the load

sequence. Peaks without a partner form the so called ‘residual’, a sequence of first diverging and then converging peaks. The residual is a left-over encountered in every RFC procedure after the range pair analysis. Commonly the residual features the largest local load extrema including the global extrema, since no partners for these data points are found in order to build range pairs. In conclusion the amplitude of the load ranges calculated from the residual are typically the ones with the largest amplitudes. Since these data points are uncorrelated they tend to appear on large time scales.

In the following, the analysis of the stress ranges is refined. We will take into account the Wöhler coefficient m and calculate S^m , in order to calculate the contribution of the load ranges to the EFL value. In addition, the time scales τ are binned in order to identify more clearly, on which time scales the differences between Gaussian and intermittent results occurs. In doing so, three groups are defined: The High Frequent (HF) range $\tau < 0.5$ sec, the Medium Frequent (MF) range $0.5 \text{ sec} \leq \tau < 12 \text{ sec}$ and the Low Frequent (LF) range $12 \text{ sec} \leq \tau$. Furthermore, we now discuss the ensemble of all ten realizations, in contrast to just one realization as above. At first the absolute damage accumulation per bin \hat{S}

$$\hat{S} = \sum_{i_{\text{bin}}} S_{i_{\text{bin}}}^m \quad (4.1)$$

is considered. Fig. 4.10a shows \hat{S} for the three different bins of time scales. It is evident that the intermittent results lead to higher damage accumulation in all three bins, but especially in the HF and MF range. We recall from the design of the time series (see Sec. 3.1) that the non-Gaussianity is only present on time scales approx. $\tau < 12 \text{ sec}$, which correspond to the HF and MF regime. The fact that the load elevation in these bins is most significant supports and explains how intermittency can increase fatigue loads.

In the following, it shall be analyzed if and how the composition of the EFL values is altered, when considering intermittency. Therefore, we calculate the contribution of each of the three time bins to the corresponding overall EFL value \tilde{S}

$$\tilde{S} = 100 \cdot \frac{\hat{S}}{T \cdot \text{EFL}^m}. \quad (4.2)$$

Fig. 4.10b shows \tilde{S} for the three frequency ranges. It becomes evident that contribution to the respective EFL value of each time bin is different between intermittent and Gaussian fields. When compared to Gaussian cases, the intermittent cases are less strongly driven by the very large time scales. Instead, the HF and MF regime contribute more to the EFL. In conclusion, not only the overall EFL values are increased due to intermittency, also the contribution – and thus importance – of each of the bins is changed. In other words, the composition of the EFL value is altered as a result of intermittency.

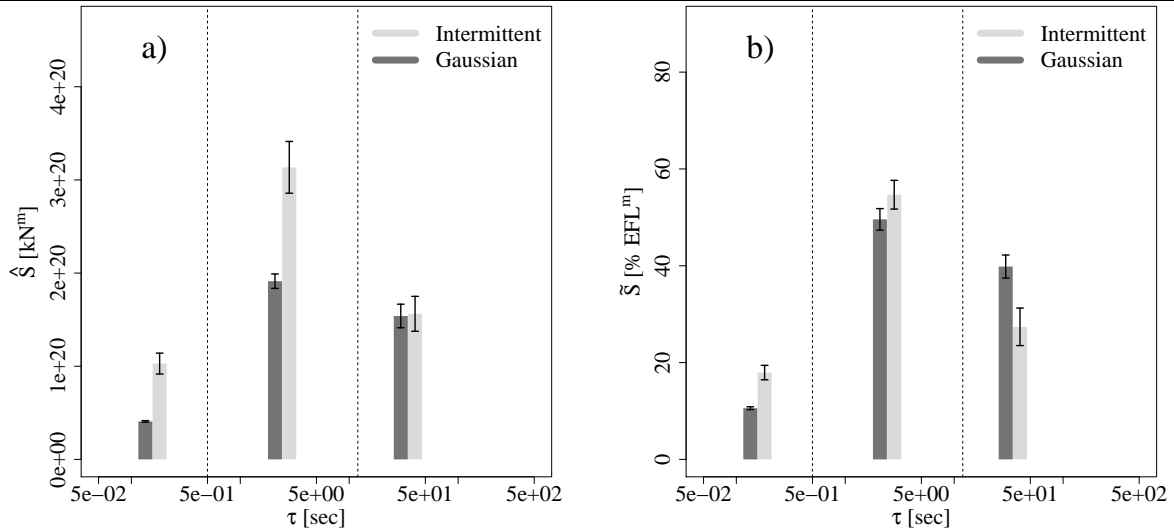


Figure 4.10: Advanced analysis of the stress ranges their time scales of the TBMFA at $9 \frac{m}{sec}$ for all ten realizations. a): Ensemble average of absolute damage accumulation \hat{S} per bin. b) Ensemble average of the percental contribution to the EFL \tilde{S} per bin. Dashed lines represent the bin breaks $t = \{0.5 \text{ sec}; 12 \text{ sec}\}$. The error bars correspond to ± 1 ensemble standard deviation around the respective ensemble average.

The observations related to Fig. 4.10 are representative throughout the entire data set, wherefore a second example is presented in the following. The load ranges of the rotor thrust at $12 \frac{m}{sec}$ is considered (compare with Fig. 4.1). The load range analysis for this case is shown in Fig. 4.11. As can be seen in Fig. 4.11a) the LF damage is only slightly different between intermittent and Gaussian fields. However the damage accumulated in the MF range is more than doubled in the intermittent case. Also the composition of the fatigue loads shown in Fig. 4.11b) changes noticeable in this case.

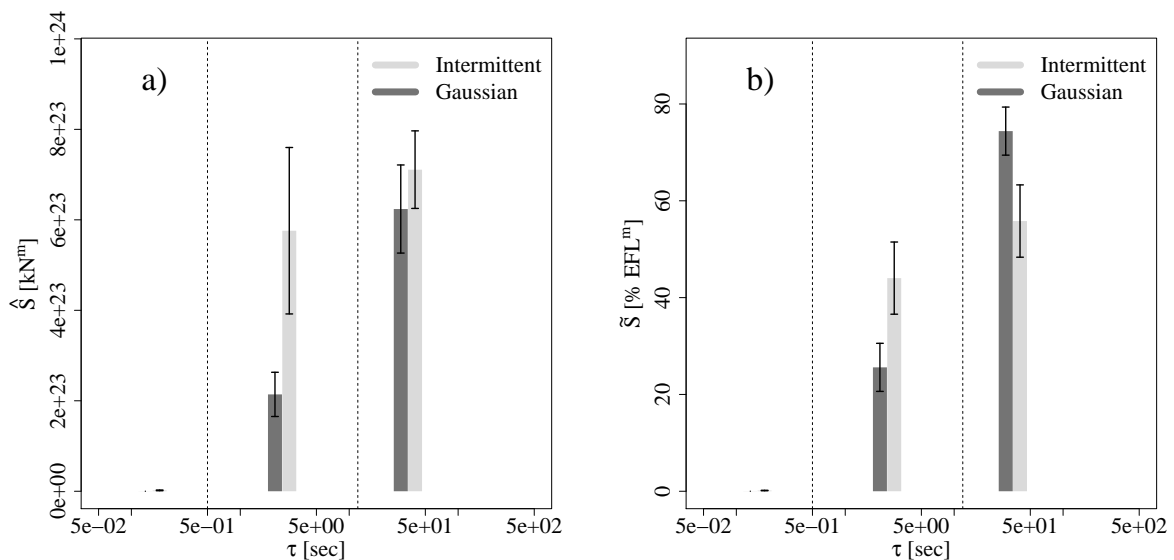


Figure 4.11: Advanced analysis of the stress ranges their time scales of the rotor thrust at $12 \frac{m}{sec}$ for all ten realizations. Analogous to Fig. 4.10.

The analysis of the stress ranges S can be summarized as follows: Firstly, it could be shown those load ranges, whose time scales are within the range of time scales that feature intermittency, showed significantly different behavior (between the Gaussian and intermittent fields). Generally the load ranges on these time scales showed an increase in accumulated damage for the intermittent wind fields. Lastly, it was shown that the contribution of load ranges on a given time scale changes, when intermittency is considered. Generally it was observed that the contribution of load ranges on intermittent time scales, was increased.

4.3 Evidence of intermittency in the load signal

In this section the load signals are investigated by other means as fatigue load analysis, namely spectral analysis and subsequently increment statistics.

Spectral analysis

Another common approach to analyze wind turbine load dynamics is spectral analysis. As mentioned previously and shown in Eq. (2.17) spectra are generally related to the auto-correlation function, which further classifies as the second moment of a two point statistic. Since intermittency in this study targets the fourth (and higher) order moments of two point statistics, the wind velocity spectra are ‘blind’ to the intermittency of the wind. This comparison between Gaussian and intermittent wind velocity spectra has been presented in Fig. 3.5. Here the focus is on the load response to these wind dynamics. An exemplary comparison between intermittent and Gaussian load spectra is presented in Fig. 4.12: The Power Spectral Density (PSD) of the rotor thrust dynamics at $9 \frac{m}{sec}$ for one realization is shown. As for the wind spectra, the load spectra of the intermittent and Gaussian wind fields do not show any significant differences. In conclusion, the intermittency effect is evident in the load ranges and the resulting EFL values, but cannot straightforwardly be represented by standard spectral analysis.

Increment analysis

Another approach is load increment analysis. As reported by Mücke et al. [21] increment statistics of wind turbine loads can be strongly related to the increment statistics of the wind. As discussed above, the differences in the load dynamics are evident in standard fatigue load calculations, but not in the spectral analysis. Here the two point statistics of the load signals are investigated. Fig. 4.13 shows the flatness of the increment time series for different values of τ for an intermittent and a Gaussian example. These observations are representative for the complete ensemble and also for other wind speeds. Evidently, the load increments follow the wind dynamics closely in both cases for the fully correlated case with an AERO wind turbine model.

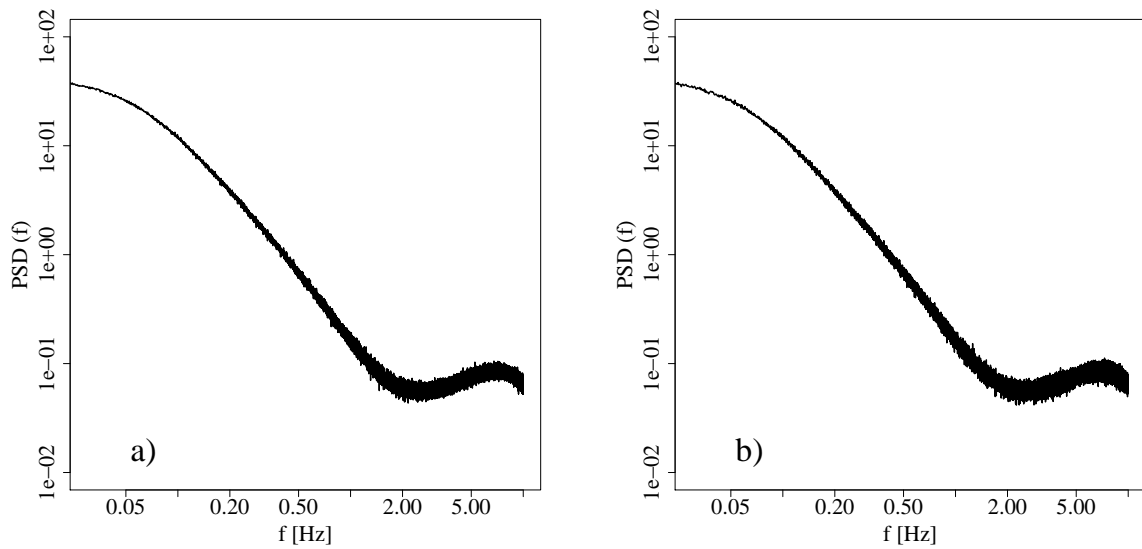


Figure 4.12: Spectral properties of the rotor thrust for one realization at $9 \frac{m}{sec}$. a) Gaussian. b) intermittent.

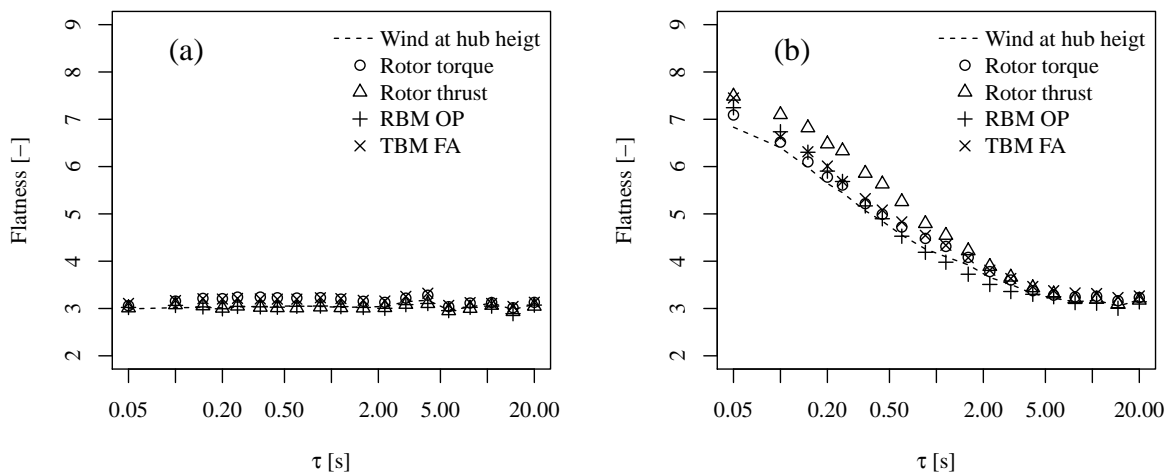


Figure 4.13: Flatness of increment distributions for different load sensors for an exemplary realization at $9 \frac{m}{sec}$ obtained with fully correlated wind fields. (a) For a Gaussian case. (b) For an intermittent case.

4.4 Aero-Servo-Elasticity

All the aforementioned results discussed in this chapter have been obtained with a purely AERodynamic (AERO) wind turbine model. In the AERO model servo-dynamics and elasticity are neglected. Therefore, one might argue that with increasing complexity the intermittency effect might vanish, for instance, when a control system is deployed. In order to test this hypothesis further calculations obtained with the ASE model have been conducted and will be discussed in this section. An overview over the differences between AERO and the ASE model is given in Tab. 2.1. The main differences are the variable rotor speed, the pitch control and the elasticity of blades and tower. Due to increased complexity of the ASE model, the results for each load sensor become more complex and feature individual characteristics. Therefore the interpretation also requires more a deeper analysis. For the sake of clear structure the load sensors are thus discussed individually in the following subsections.

Rotor thrust

Figs. 4.14 shows the EFL results for the rotor thrust obtained with an ASE turbine model. When compared against Fig. 4.1, differences in the details of the trends are evident (as expected). The intermittency effect is still clearly pronounced for the ASE model, at some wind speeds even more as for the AERO model.

Fig. 4.14a shows the absolute EFL value. In comparison to the purely aerodynamic results, cf. Fig. 4.1a, a small decrease in EFL can be observed in the pre-rated regime. In this regime, pitch control is not active, however the rotor speed is now enabled to vary based on inertial properties, aerodynamics and counter-torque by the generator. Especially inertia could lead to damped load dynamics, which would go along with a decrease in EFL.

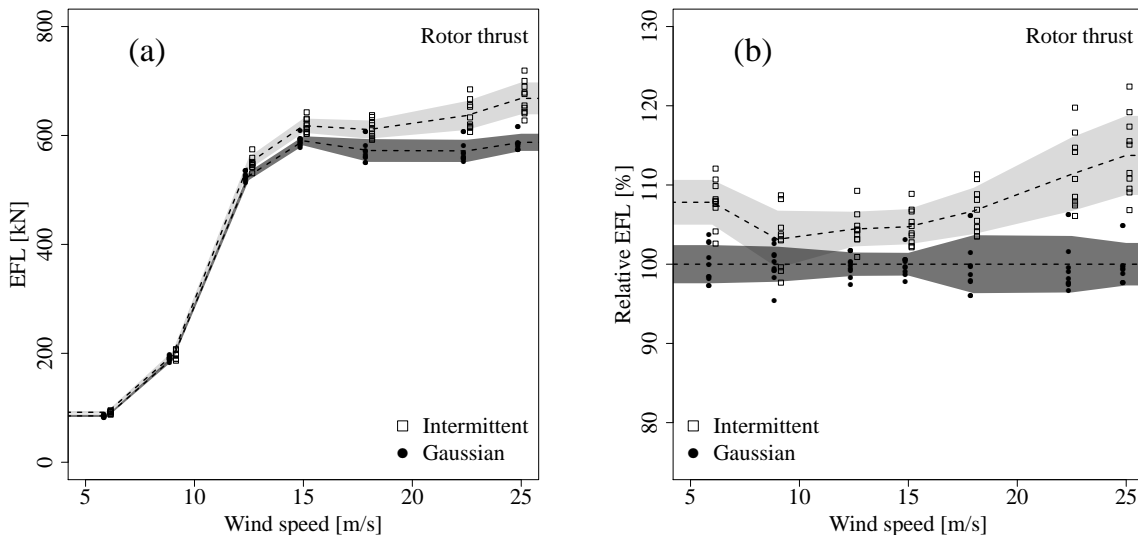


Figure 4.14: EFL (cf. Eq. (2.47)) for the rotor thrust obtained with an Aero-Servo-Dynamic (ASE) turbine model. Analogous to Fig. 4.1.

Continuing the comparison between Figs. 4.14a and 4.1a for the post rated regime shows a different picture: At higher wind speeds an almost constant level or slow increase of EFL is evident over a wide range of wind speeds. A plausible explanation for an increased EFL compared to the purely aerodynamic model is again the variable rotor speed and the pitch control system. Intuitively one would think that the addition of a regulative system featuring a pitch control would damp and decrease the loads. While this holds true for the ultimate loads, this is not true for the fatigue loads in this case. Due to the pitching, many load cycles are added, which is reflected in the increase of absolute EFL values.

These hypothesis can be validated when studying the differences in load dynamics between the AERO and the ASE model. These are exemplarily shown in Fig. 4.15. It is evident that load amplitudes are larger for the ASE model. Possibly the control system for this turbine can be refined in order to damp the load amplitudes. However this is out of scope for this work. Lastly, one must not forget that the wind field features elusively very large, fully correlated structures, which are an enormous challenge for the control system. Fig. 4.15 illustrates that a significant share of the load dynamics stem from servo-dynamic effects. Therefore the increase in EFL due to intermittency can be explained as follows: Intermittent dynamics are more erratic and irregular than Gaussian ones. This requires the control system to be more active, leading to larger load amplitudes.

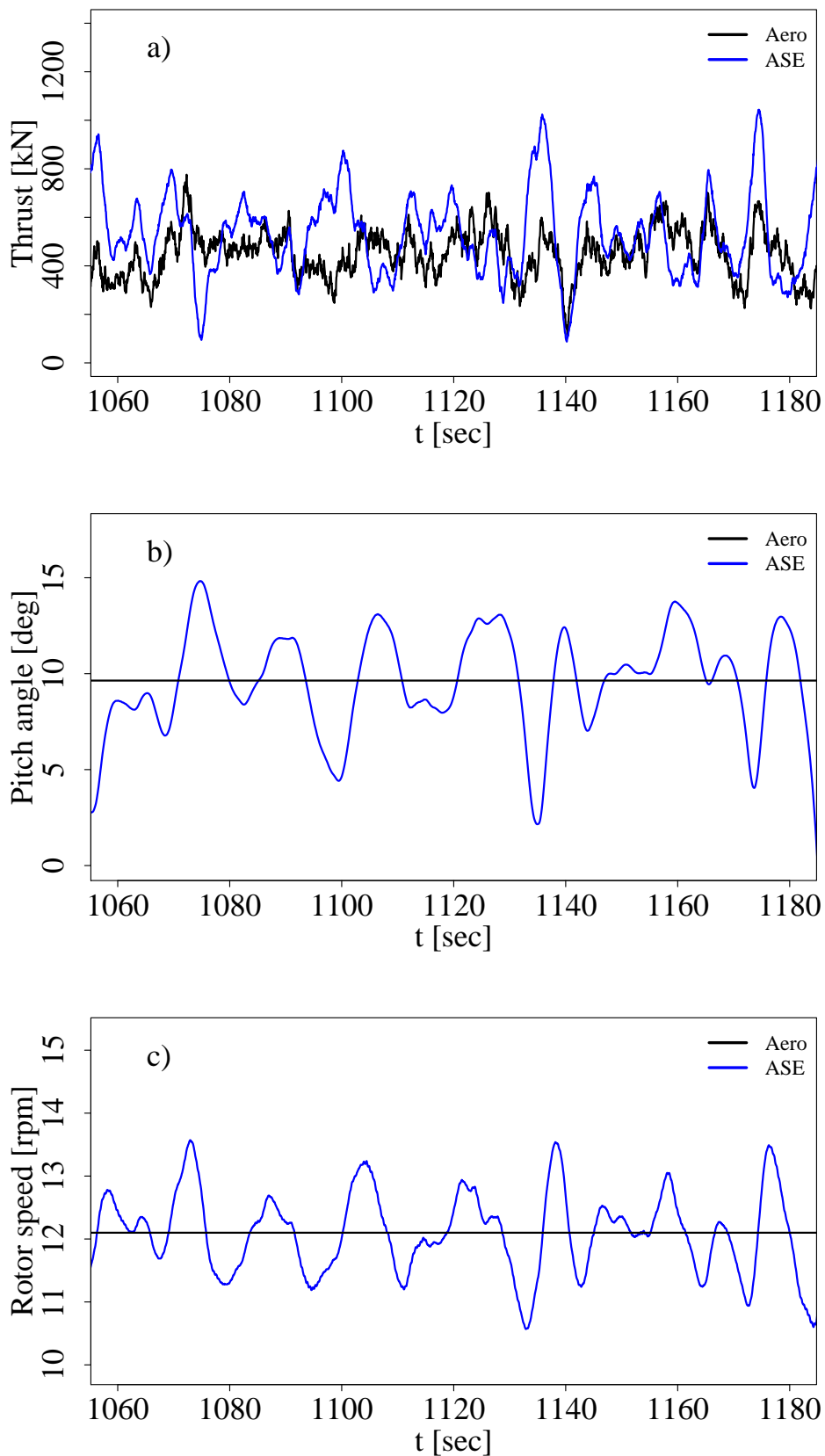


Figure 4.15: Wind turbine dynamics for a purely Aerodynamic (Aero) and an Aero-Servo-Elastic (ASE) model in the post-rated regime at $15 \frac{m}{sec}$. Excerpt of time series for a) rotor thrust, b) pitch angle and c) rotor speed.

Rotor torque

The results for the torque are shown in Fig. 4.16. For the post rated regime, the typical increase in EFL due to intermittency is evident. Additionally, increased scattering in the pre-rated regime at $6 \frac{m}{sec}$ and especially at $9 \frac{m}{sec}$ is evident for both types of wind fields, which is discussed in the following.

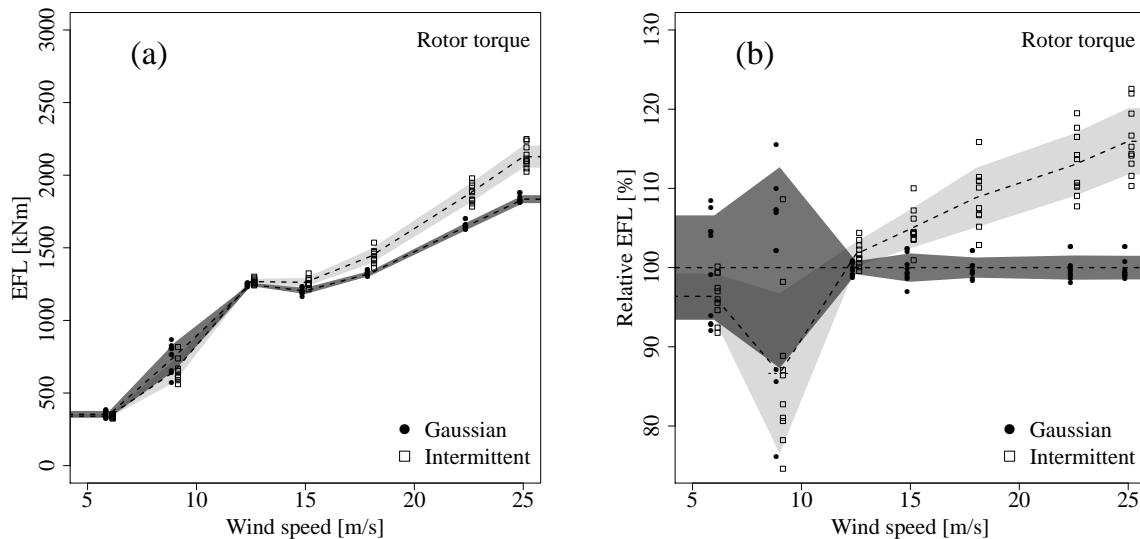


Figure 4.16: EFL for the rotor torque with an ASE model. Analogous to Fig. 4.14.

An investigation into the corresponding data yielded that steep load peaks in the order of five standard deviations and more occur in the torque time series. While these are a response to certain event in the wind and the turbine state, they are not an exclusive result to intermittency, since these peaks could be observed for both types of wind fields. An exemplary case for these observations is given in Fig. 4.17. It shows the rotor torque Q for both the ASE and the aerodynamic model at mean wind speed $\langle u_{HH} \rangle = 9 \frac{m}{sec}$. Due to rotational inertia, the dynamics for the ASE model are damped compared to the aerodynamic model, as shown in Fig. 4.17a. However, when the dynamics $Q' = Q - \langle Q \rangle$ are normalized by the corresponding standard deviation σ it is evident that the extreme load peaks in the ASE are larger, see Fig. 4.17b. An example for these events is given in Fig. 4.17c at $t \approx 100$ sec. It can be observed that the ASE model runs into an extreme torque peak in the order of five σ , while the aerodynamic model follows the wind dynamics perfectly due its enforced boundary conditions. It is not straightforward to formulate which wind event leads to his behavior. In the presented example the build up of the torque peak is associated with an over-speeding of the rotor (no pitch control, pre-rated regime). Afterwards the rotor is subjected to a steep drop in wind speed in the order of two σ , which leads to the steep drop in Q . As discussed in Sec. 4.2, extreme load ranges drive the EFL values the most due to the exponentiation with the Wöhler coefficient m . The extreme peaks in Q' dominate the resulting EFL. Whether e.g. two or three of these events occur in a given sample, makes a large and significant impact, wherefore the results for this sensor do not give a reliable answer with respect to the issue of intermittency.

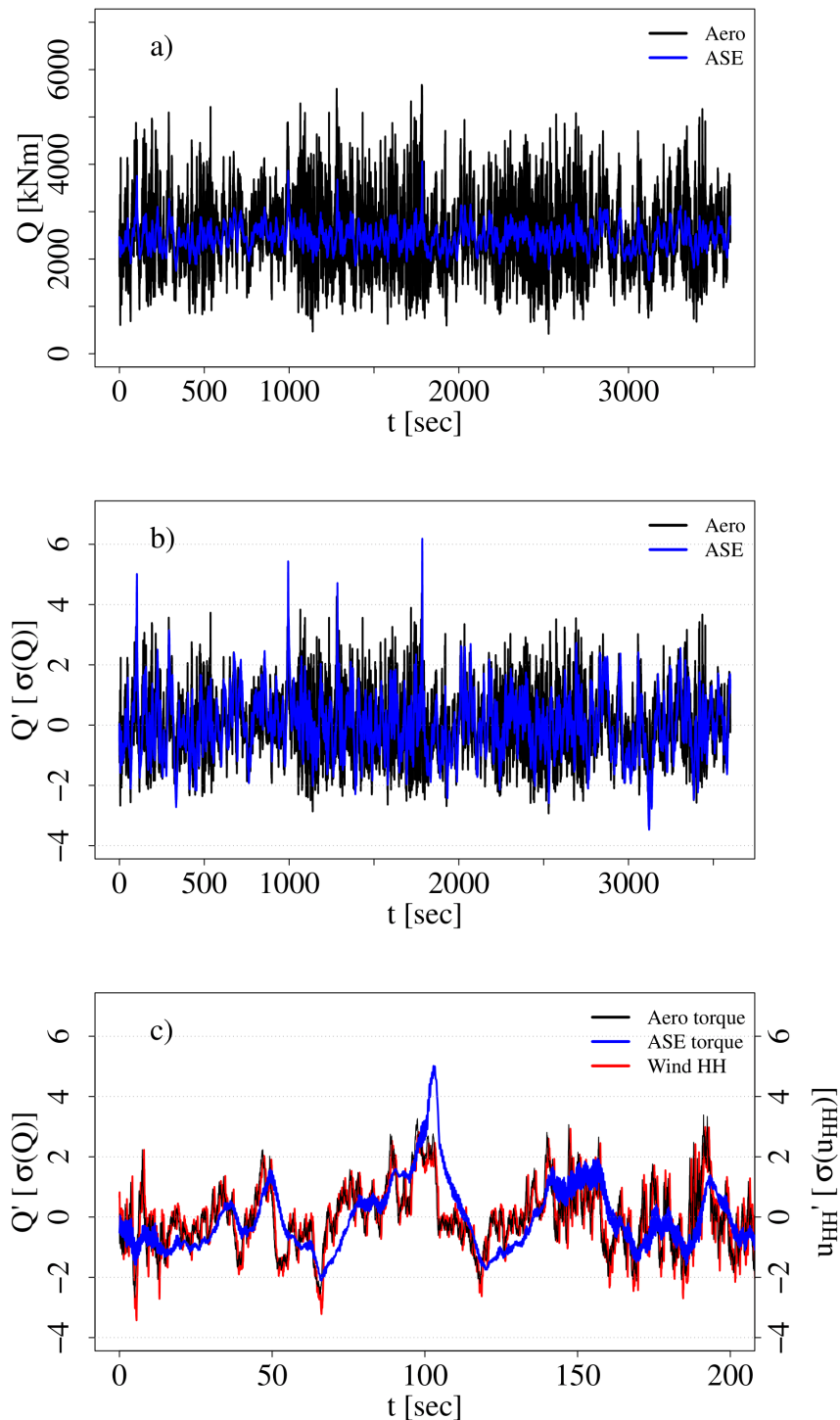


Figure 4.17: Rotor torque and wind dynamics for a purely Aerodynamic (Aero) and an Aero-Servo-Elastic (ASE) model in the pre-rated regime at $9 \frac{m}{sec}$. a) Absolute torque Q , b) Torque dynamics $Q' = Q - \langle Q \rangle$ represented in standard deviations c) An excerpt of Q' for the ASE and the aerodynamic model and the hub height wind velocity dynamics u'_{HH} normalized by standard deviation in the range $0 \leq t \leq 200$.

RBMOP and TBMFA

Similar observations made for the rotor thrust and torque are also found in the response of the blade Root Bending Moment Out of Plane (RBMOP), which are shown in Fig. 4.18. As mentioned before, the rotational sampling of the wind field for this load sensors takes place at a lower frequency than the other three load sensors, as it relies on one blade only. This in return is a plausible explanation for a less resolved and slightly different trend. The key aspect of this results is that there are still significant differences due to intermittency. The results obtained for Tower base Bending Moment Fore-Aft (TBMFA) are displayed in Fig. 4.19. A well pronounced difference between intermittent and Gaussian results is evident. As for AERO model, there are still similarities between the TBMFA result and the rotor thrust result shown in Fig. 4.14.

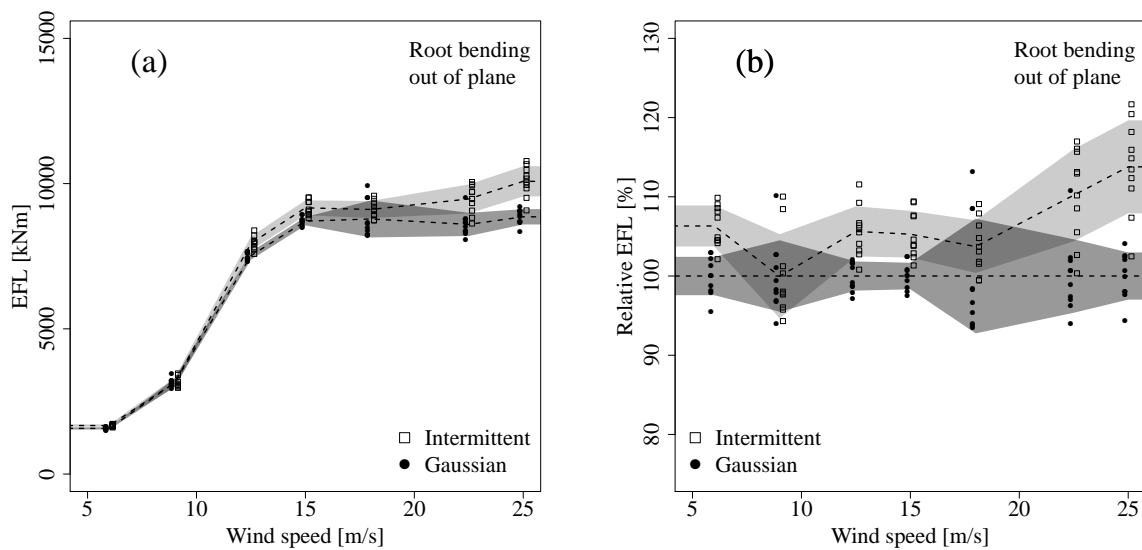


Figure 4.18: EFL for the RBMOP with an ASE model. Analogous to Fig. 4.14.

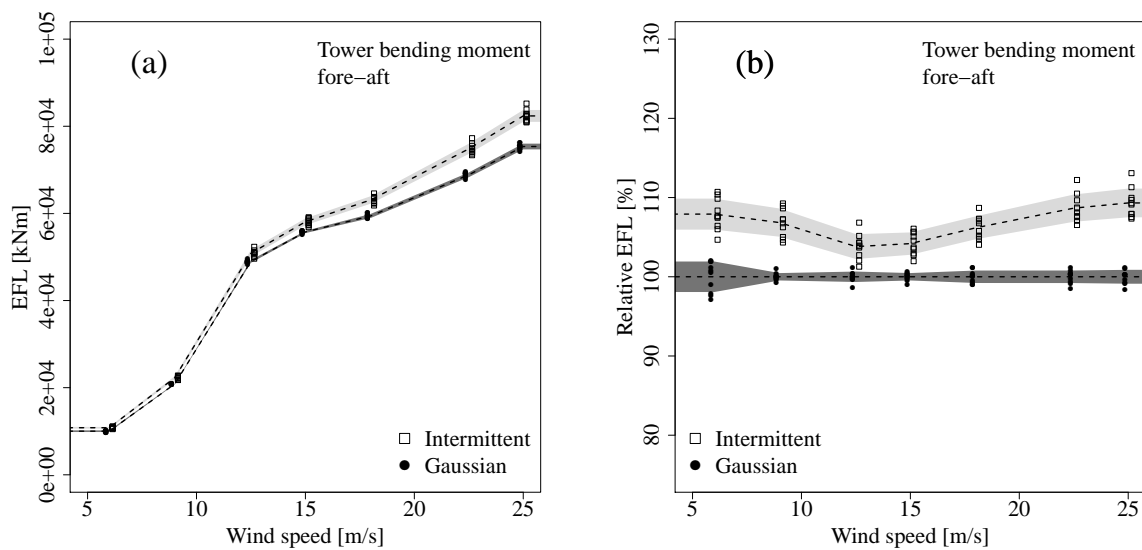


Figure 4.19: EFL for the TBM FA with an ASE model. Analogous to Fig. 4.14.

4.5 Summary

In this section the impact of intermittent wind dynamics on wind turbine loads were analyzed with fully correlated wind fields. An intermittency effect for fully correlated wind fields could be reported for several import load channels. An increase of fatigue loads for the presented set-up in the order of +5% (sometimes even higher) was evident. Due to the isolation of intermittency in the wind fields, these differences must stem from higher order statistics. This was also shown by a deeper analysis of the load dynamics. A difference of this magnitude is large enough to be relevant in the design process of a wind turbine. Thus, an incorporation of intermittency into standard wind models might be worth considering. This in return might legitimize a reduction of safety factors. The control system or inertia of the rotor did not filter out the intermittent dynamics, since the key conclusions drawn from results obtained with an AERO model also hold for true for an ASE model. The altered load dynamics are not straightforwardly detectable within a spectral analysis of the load signal, but they can be detected in an load increment analysis. Some of these findings have been published, see [64, 65].

The results presented in this chapter have to be understood as fundamental, since they are obtained with fully correlated wind fields, which neglect transversal dynamics and spatial variability related to the concept of ‘coherence’. In Chapter 5 the presented findings will be revisited, while wind fields including spatial variability are considered.

Chapter 5

The impact of spatial variability on the intermittency effect

The results presented in the previous chapter have been obtained with wind fields featuring highly simplified spatial dynamics. A clear intermittency effect in the fatigue loads in the order of 5% has been reported. However all results brought forward in Ch. 4 are based on the premise of fully correlated wind fields. In this chapter the intermittency effect is analyzed in a framework based on wind fields that include spatial variability. In doing so the dynamics of the wind system are becoming more complex. The main dynamic that is added to the system is the rotational sampling of the wind field: With spatially varying fields the blades will slice through different coherent structures while rotating. It is the key question how the intermittency effect will behave when the turbine faces more complex wind fields. Aside from different wind fields, this problem is approached within the same framework as in Ch. 4. The results are presented and discussed in the following. As outlined in Sec. 3.2 wind fields with subdivided $N \times N$ grids and fields with stationary coherent structures have been generated. A special case of the subdivided $N \times N$ grids is the delta correlated case, which features 31×31 uncorrelated time series. The results obtained for this delta correlated fields is discussed in Sec. 5.1. Subsequently fields with much coarser subdivided spatial dynamics are discussed in Sec. 5.2. The results obtained with fields featuring stationary coherent structures are presented in Sec. 5.3. Finally, the Chapter is rounded out by a summary of the main conclusions drawn from the presented results in Sec. 5.4.

5.1 Delta correlated fields

Chapter 4 featured results obtained with an extreme type of wind field: A spatially fully correlated wind field with spatially invariant wind dynamics. In this section the focus is on another extreme scenario, the delta correlated field type. An example for this field type is shown in Fig. 3.8a. In every of the 31×31 grid points a different, uncorrelated time series is prescribed. It is expected that this scenario delivers the weakest or no intermittency effect, since the dynamics of the wind time series are not synchronized at all. If however an intermittency effect was to be found the delta correlated fields this would be a strong argument that an intermittency effect is evident all kinds of spatial dynamics.

The EFL results for the rotor thrust based on delta correlated fields obtained with a AERO model are shown in Fig. 5.1. It is evident that the absolute EFL values (Fig. 5.1a) are much smaller compared to the fully correlated EFL results shown in Fig. 4.1a. The reason for this decrease can be explained with the features of the wind field: For the delta correlated the rotor is excited by a large number of Gaussian processes over the course of one revolution. In conclusion, the predominant effect of the wind field on the turbine is not due to its temporal dynamics, but rather due to its spatial variation (which is highly regular in this case). This manifold excitation of the wind turbine results in a rather smooth load dynamic, since none of the exciting time series has a huge influence and extremes are going to cancel each other out. As a result the excitation of this kind of wind field is very uniform and steady and features rather small EFL values. The same effect can also be seen in relative EFL results shown in Fig. 5.1b: Differences between Gaussian and intermittent results are not evident. There is no intermittency effect. This result holds also true for the remaining four load sensors, which are not discussed in detail here for the sake of brevity.

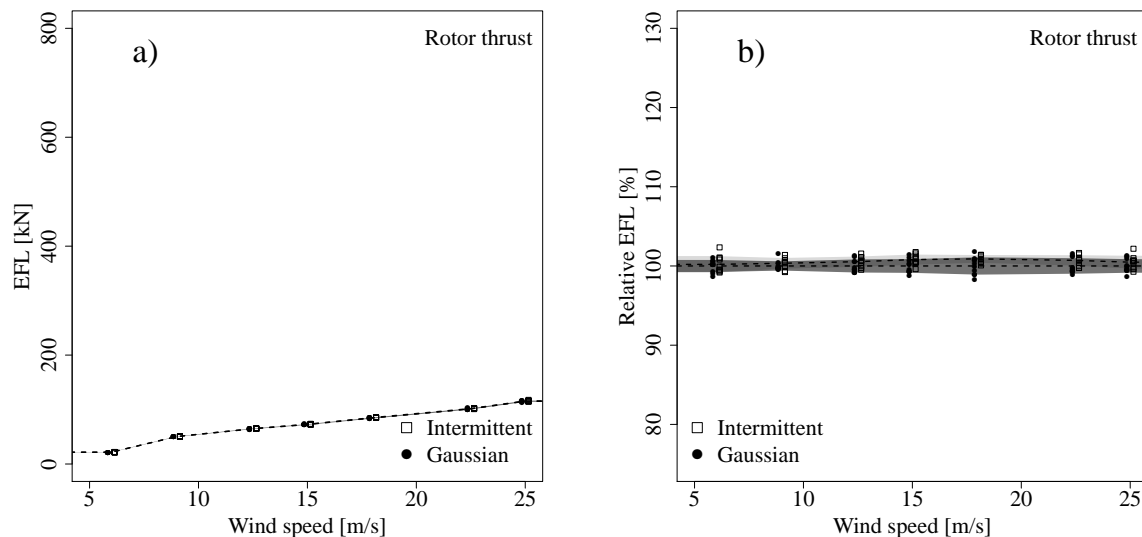


Figure 5.1: EFL for the rotor thrust with an aerodynamic model for a delta correlated field. Analogous to Fig. 4.1.

In order to gain a deeper insight into the load dynamics, a load increment analysis for all four load sensors was conducted. The results are shown displayed. Fig. 5.2. Evidently both the Gaussian and intermittent fields lead to Gaussian behaved load increments. The explanation for this is that the load increment statistics do not follow the temporal wind dynamics, but are highly Gaussianized due to the superposition of many wind time series (Central Limit Theorem).

The delta correlated wind fields were also tested with an Aero-Servo-Elastic (ASE) wind turbine model. However since the purely aerodynamic response was already found to Gaussianized the ASE results did not show any intermittency effect either. In conclusion there is no intermittency effect in the case of delta correlated wind fields.

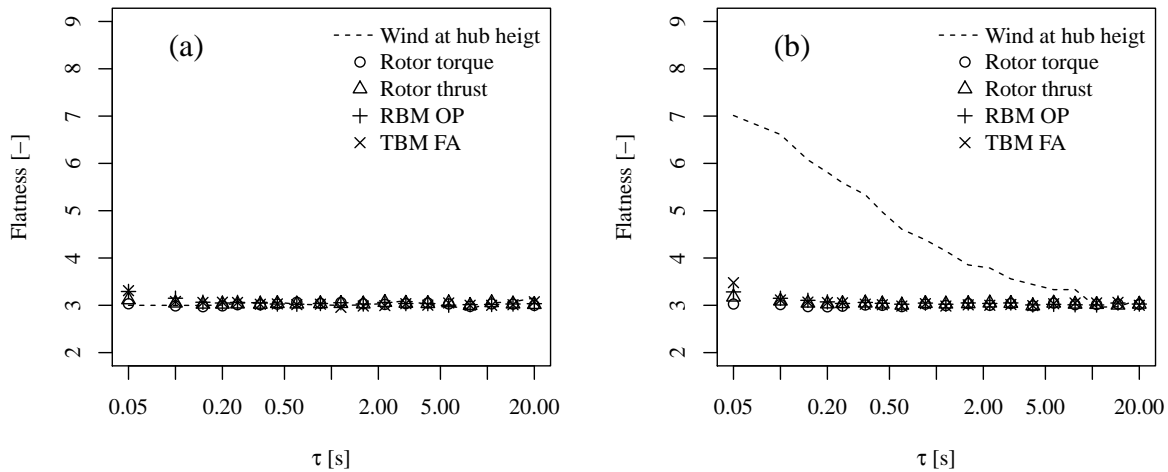


Figure 5.2: Flatness of increment distributions for different load sensors for an exemplary realization obtained with delta correlated wind fields. (a) For a Gaussian case. (b) For an intermittent case.

Recalling the result presented in Ch. 4, an intermittency effect is evident for the fully correlated fields. In combination with the results presented in this section the crucial dependence of the intermittency effect (and temporal wind dynamics in general) on the spatial variation of the wind field of the field is shown.

5.2 Subdivided fully correlated fields

In order to investigate the impact of the spatial dynamics further, wind fields with spatial dynamics that are neither fully nor delta correlated are considered. As outlined in Sec. 3.2 a straight forward approach to realize spatial variation within the wind fields is to subdivide the rotor plane into fully correlated regimes, which are uncorrelated with one another, as shown for instance in Fig. 3.9. This approach is easy to implement and the size of wind structures is easily assessable.

The most coarse subdivision is the 2×2 field (see Fig. 3.9a). Results obtained for such a field with the AERO model are displayed in Fig. 5.3. Compared to the results obtained for the fully correlated grid (Fig. 4.1a) the absolute EFL values decrease. A possible explanation is the following: Each rotor blade is excited by a different time series, wherefore extreme events are compensated. In doing so the excitation by the wind becomes more regular and steady. However an intermittency effect of roughly 3% is evident, as displayed in Fig. 4.1. The dynamics of the wind turbine system are now affected by both the rotational sampling of the 2×2 subdivision and the temporal dynamics of the wind time series. This result is representative for all other load channels.

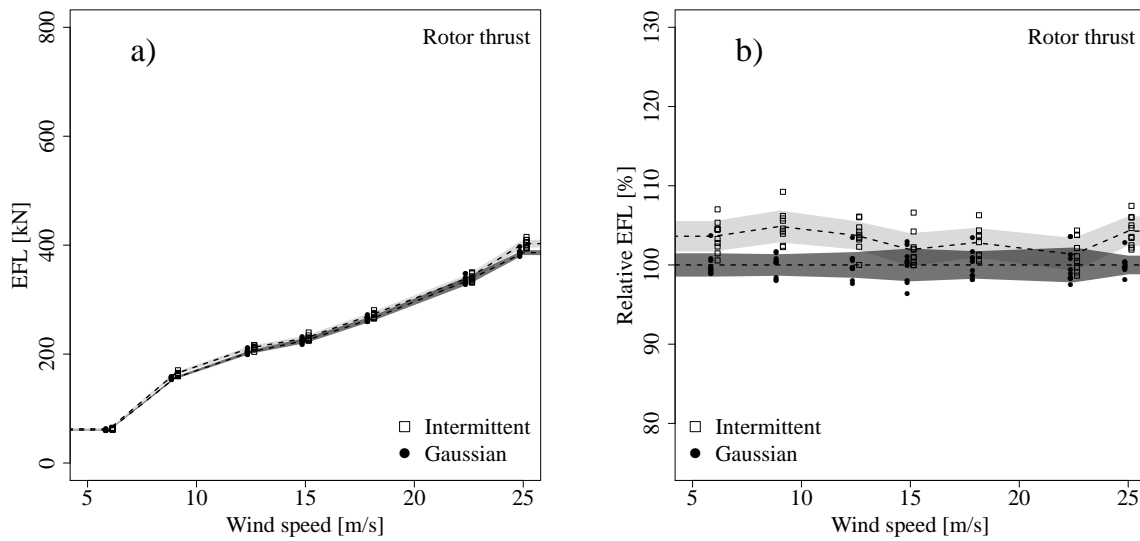


Figure 5.3: EFL for the rotor thrust for a 2×2 field obtained with an aerodynamic model. Analogous to Fig. 4.1

As observed for the previous cases the dynamics and complexity of the wind turbine system changes drastically when the ASE model is considered. As an example, Fig. 5.4 shows the corresponding EFL for the thrust for an ASE model. While details may vary from the AERO results, the magnitude of the intermittency effect is approx. constant in the order of 3%. In conclusion the results obtained for the 2×2 field still exhibit an intermittency effect.

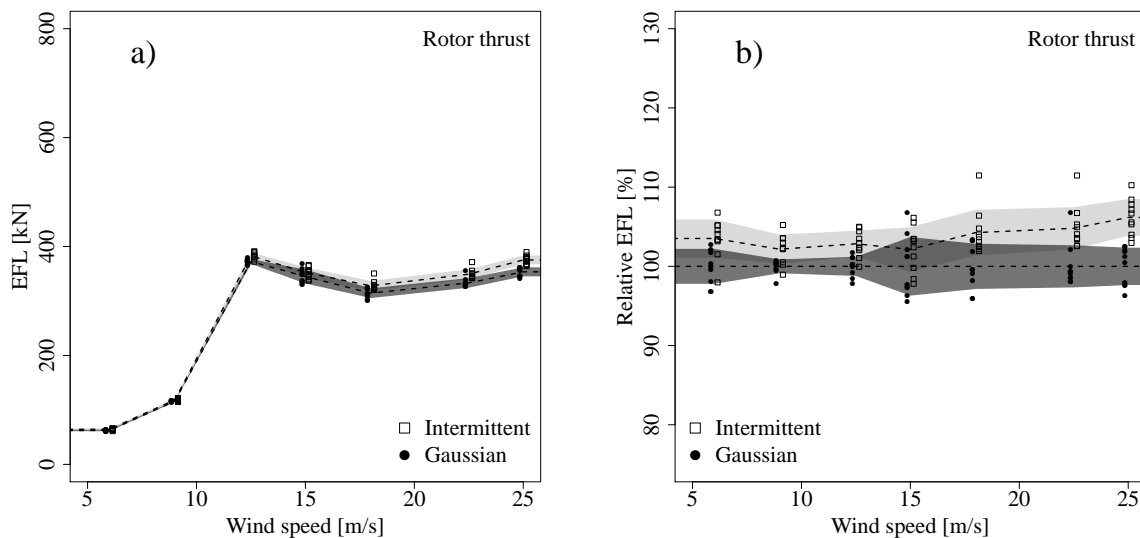


Figure 5.4: EFL for the rotor thrust for a 2×2 field obtained with an ASE model. Analogous to Fig. 4.1.

From these results above the question arises, how large spatial structures need to be in order for the intermittency effect still to be relevant. In order to answer this question, 3×3 , 4×4 and 5×5 fields have been evaluated. The corresponding results are shown in Figs. 5.5, 5.6 and 5.7, respectively. A clear trend is evident: A decay of the intermittency effect with decreasing structure sizes can be observed. At the latest for the 5×5 grid the intermittency effect vanishes completely. This indicates that the critical size of structures is in the order of approx. $\frac{1}{3}$ or $\frac{1}{4}$ rotor diameters. Comparable trends are evident in the remaining load sensors (not shown here).

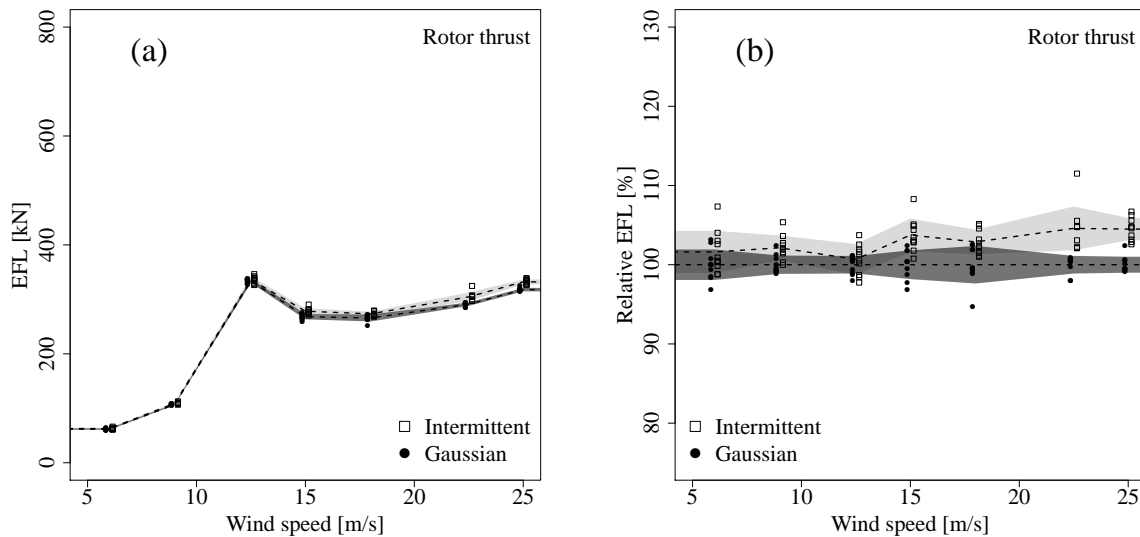


Figure 5.5: EFL for the rotor thrust for a 3×3 field obtained with an ASE model. Analogous to Fig. 4.1.

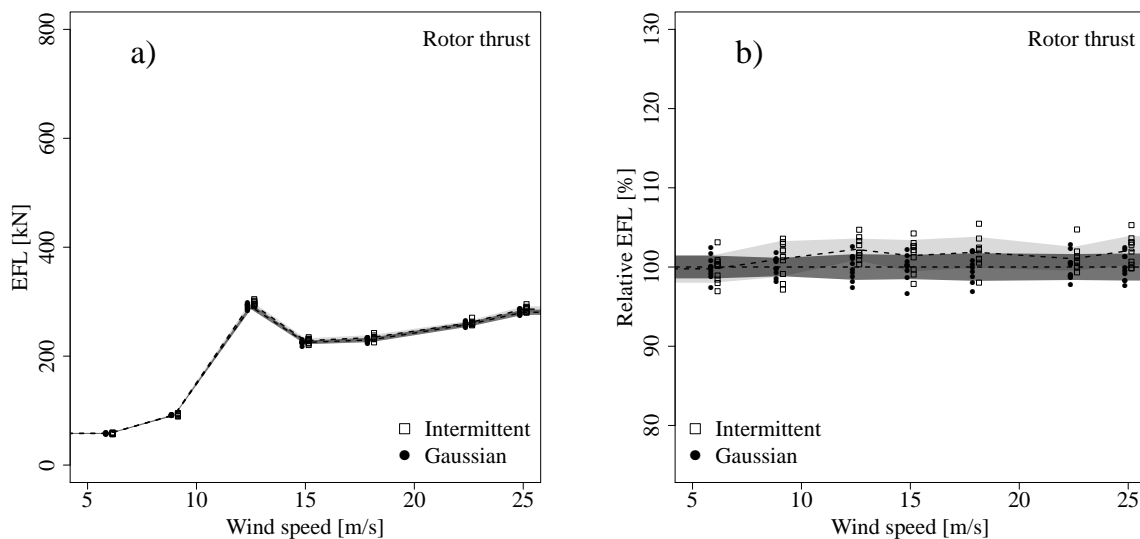


Figure 5.6: EFL for the rotor thrust for a 4×4 field obtained with an ASE model. Analogous to Fig. 4.1.

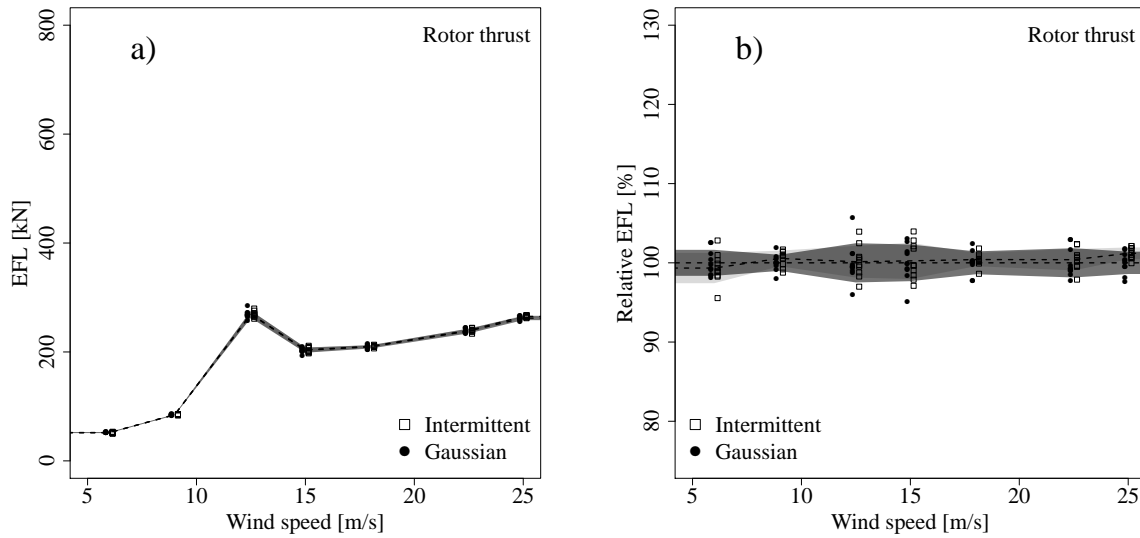


Figure 5.7: EFL for the rotor thrust for a 5×5 field obtained with an ASE model. Analogous to Fig. 4.1.

In order to underline the decreasing intermittency effect with decreasing structure sizes, the increment statistics of a given load time series $x(t)$ are calculated as $x_\tau = x(t + \tau) - x(t)$. Fig. 5.8 shows x_τ for one exemplary, intermittent realization at $9 \frac{m}{sec}$ both for the aerodynamic and the ASE model for different spatial variations. Note that 1×1 corresponds to the fully correlated case and 31×31 corresponds to the delta correlated case. It is evident that the signals become more and more Gaussian towards smaller scaled structures. Another observation in Fig. 5.8a is that the 3×3 field features more non-Gaussianity than the 2×2 field. This very likely stems from a combination of the particular spatial sub-division in combination with the turbine's operating point at $9 \frac{m}{sec}$, which seems to trigger non-linear dynamic stall effects. This observation is related to the observations made for the fully correlated case, cf. Fig. 4.1. It is evident that the signals become more and more Gaussian towards smaller scaled structures. An unexpected observation in Fig. 5.8a is that the 3×3 field features more non-Gaussianity than the 2×2 field. This possibly stems from a combination of the particular spatial sub-division in combination with the turbine's operating point at $9 \frac{m}{sec}$.

Some drawbacks are inherent to the approach of subdivided wind fields: Wind field of this kind do not contain a multitude of differently sized structures of random shape, but only regularized ones of the same scale. This might lead to unwanted periodicities in the load signal: Due to the regular pattern, the rotor is excited periodically over the course of a revolution when going over from one fully correlated regime to another. In a 2×2 case, this happens e.g. four times per a blade rotation. In order to test the load signal for such periodicities, the Power Spectral Densities (PSDs) S_{xx} of the rotor thrust signal for different subdivided wind fields are investigated. They are shown in Fig. 5.9. As can be seen from the AERO results in Fig. 5.9a, strong periodicities at the 3P frequency $f_P = 3$ and its harmonics are evident. With respect to the wind fields, the periodicity of the 3P harmonics clearly increases towards lower structure sizes. Also the spectrum becomes more flat, which indicates the the loss of the temporal wind dynamics.

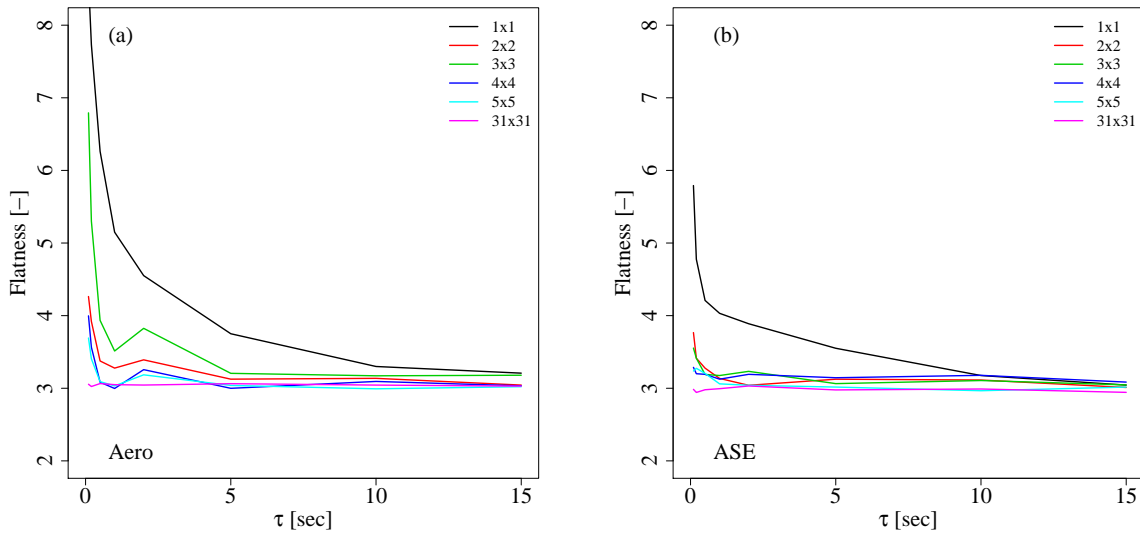


Figure 5.8: Flatness of the 2P statistics of the thrust signal for different subdivided grids for one exemplary intermittent realization at $9 \frac{m}{sec}$. (a) Purely aerodynamic model. (b) Aero-Servo-Elastic (ASE) model.

Obviously the spectra obtained with the ASE wind turbine model shown in Fig. 5.9b are fundamentally different from the purely aerodynamic response. The additional spikes in the spectra correspond to the Eigen-Frequencies of the ASE system, predominately to the tower bending Eigen-Modes and the collective flap-wise Eigen-Modes. Despite the differences, the observations regarding the periodic content in the spectra are the same for the AERO and the ASE model: With decreasing structure sizes an increase of periodicities and a decrease of temporal wind dynamics are evident in the load signal.

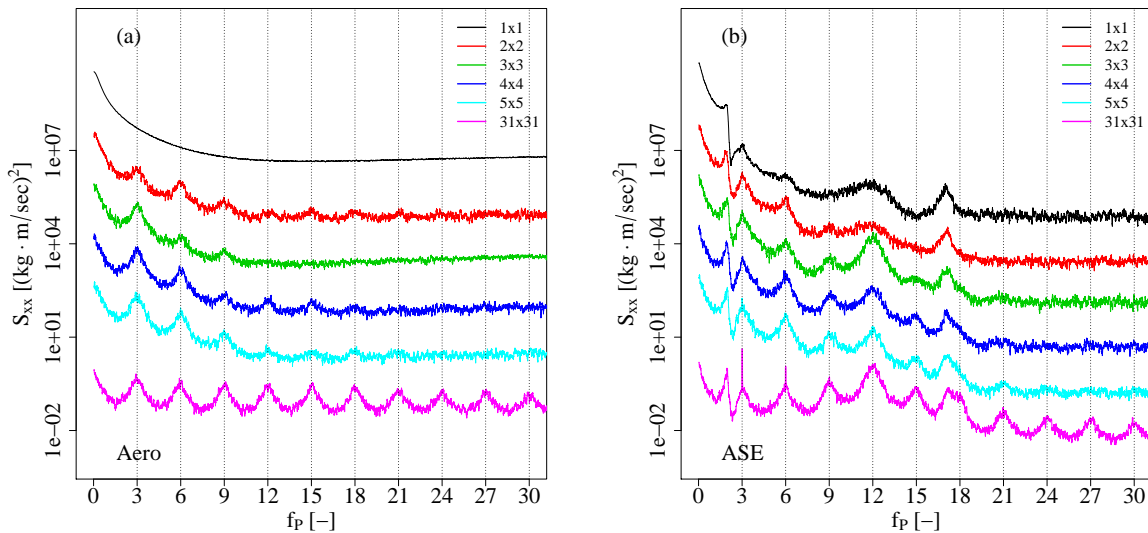


Figure 5.9: Power spectral densities against frequency $f_P = \frac{f}{2\pi(\omega(t))}$ of the thrust signal for different subdivided grids for one exemplary intermittent realization at $9 \frac{m}{sec}$. Spectra are vertically shifted for better representation. (a) Purely aerodynamic model. (b) Aero-Servo-Elastic (ASE) model.

Generally speaking, periodicities will occur in a realistic wind turbine load signals e.g. at the 1P and 3P frequencies and at Eigen-Frequencies of the system. However, in the discussed case the periodicities stem from the excitation of the spatial wind field characteristics. Since wind and atmospheric turbulence are non-periodic but stochastic, these periodicities are unphysically strong. This holds true especially for wind turbine models featuring constant rotor speed (AERO model).

In conclusion the results obtained with spatially sub-divided fields do not reflect all aspects of realistic wind fields. However they provide an insight into the impact of spatial variation on the load response. The results give evidence that with increased spatial variability the temporal dynamics in general become less important, as shown by the Gaussianization of the load increments and the decrease of the intermittency effect.also

5.3 Stationary coherent structures

Due to the limited physicality of the subdivided grids discussed in the previous section, a different approach towards spatially varying wind fields is considered. In order to achieve randomly shaped structures of different length scales, a stochastic approach for the spatial dynamics is chosen. The generation of these fields is outlined in Sec. 3.2. Exemplary visualizations are given in Figs. 3.11 and 3.12. For each type of wind field (Gaussian and intermittent) five realizations of spatial variations and five time series are considered resulting in $5 \times 5 = 25$ data points per wind speed. Only the wind speeds 9, 12.5 and $22.5 \frac{m}{sec}$ are considered due to the increased amount of cases per wind speed.

Results for the rotor thrust and a range $d_r = 2R = 1D$ obtained with the ASE model are shown in Fig. 5.10. Since the spatial correlation expands to length scales $2R$, one might expect results to be similar to the results obtained with fully correlated wind fields, see Chapter 4, for which a pronounced intermittency effect was evident. In general, differences between Gaussian and intermittent EFL values can be observed in Fig. 5.10. However, the data set is dominated by a large scatter, which is evident in all load sensors and prohibits to draw definite conclusions with respect to the intermittency effect.

As a second example Fig. 5.11 is given. It shows the corresponding results for $d_r = \frac{1}{2}R$. Again, scattering in the data set is present alongside differences between intermittent and Gaussian fields. The same observations in all load sensors were made for a wide range of cases.

While the scattering hampers to draw conclusions with respect to the intermittency effect directly, other interesting observations can be made: Data points in Figs. 5.10 and 5.11 have been arranged in a way so that data points that stem from the exact same realization of the model for spatial dynamics (variogram) are plotted in a vertical line on the exact same horizontal position. Note that intermittent and Gaussian fields are based on different variogram realizations! Data points obtained with a different variogram realization are slightly shifted horizontally. This representation allows to evaluate the impact of the spatial dynamics and further, to some degree, to compare it against the impact of the spatial dynamics. With this details in mind it can be seen that the spatial dynamics have a strong impact on the result, since the EFL values obtained

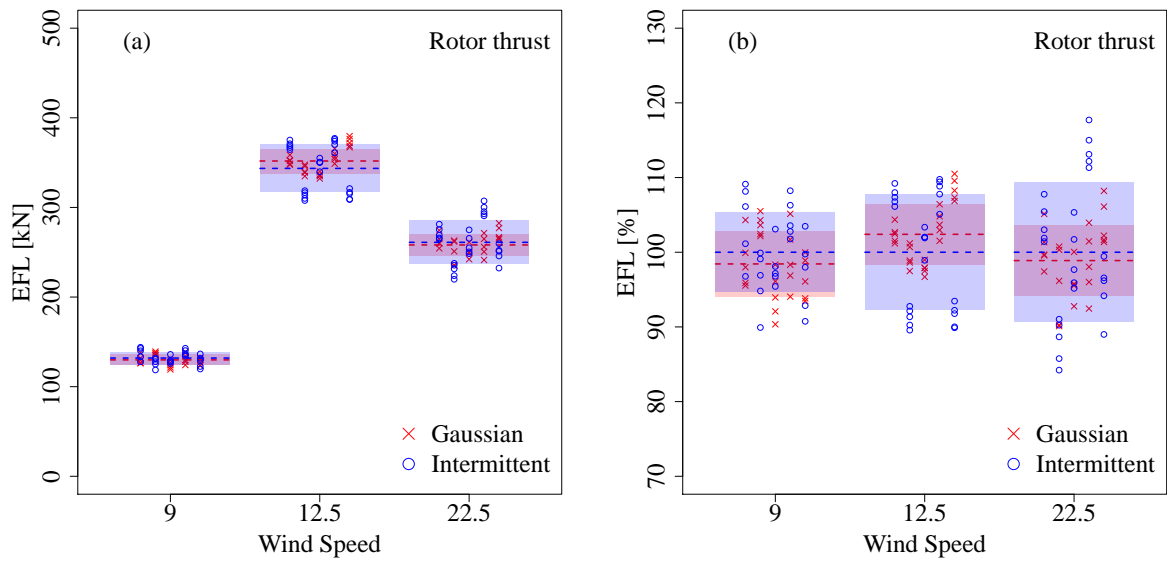


Figure 5.10: EFL for the rotor thrust for $d_r = 2R$. For better visualization data points are shifted horizontally. Data points stemming from the exact same spatial realization are plotted in a vertical line at the exact same horizontal position. Subplots (a) and (b) show absolute and relative values, respectively.

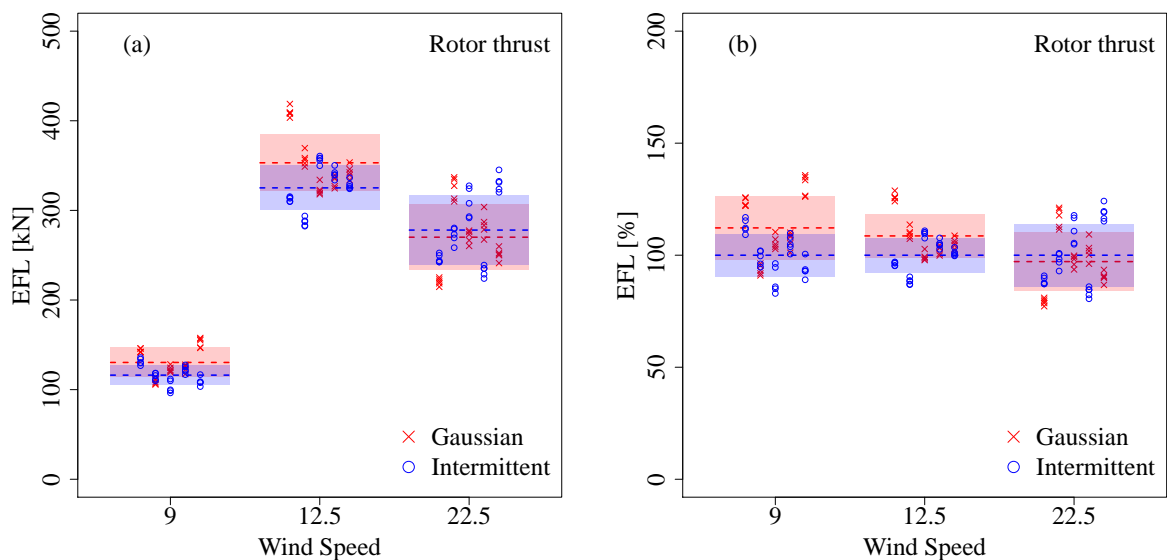


Figure 5.11: EFL for the rotor thrust for $d_r = \frac{1}{2}R$. Analogous to Fig. 5.10.

with the same variogram realizations are clustered. In other words: For this data set the EFL value is rather determined by the underlying spatial dynamics than the temporal dynamics. This can be supported mathematically by calculating the standard deviation of EFL values for different spatial realizations σ_s and compare it against the standard deviation for different temporal realizations σ_t . Within the presented framework such calculations clearly showed that $\sigma_s > \sigma_t$.

Possible explanations for this observation are the following: Firstly, very restrictive boundaries were formulated for the temporal dynamics, see Sec. 3.1. In contrast, the spatial dynamics were added in a rather simple approach. Possibly the spatial dynamics need to be more constrained. Secondly, the spatial discretization $d_y = d_z = 4.5m$ is rather coarse compared to the temporal discretization $d_t = 0.05 \text{ sec}$, see Sec. 3. Considering Taylor's hypothesis of frozen turbulence d_t can be related to spatial dimension when multiplied with the mean flow velocity u_0 resulting in length scales 0.3 to 1.25m, depending on u_0 . Hence, the coarse resolution of the spatial dynamics could be source for the strong variation due to the spatial dynamics. Thirdly, it is possible that the spatial dynamics are principally more relevant than the temporal aspects.

Future work might focus on more accurate spatial characterization and a finer spatial resolution to overcome these issues. However, the underlying BEM approach has its limits as well, wherefore one might also think about a higher order aerodynamic model, e.g. a vortex code. Following this approach one might also consider the implementation of intermittency into the spatial dynamics, since it is not exclusively a temporal phenomenon, see. Sec. 2.1.1.

5.4 Summary

Here the findings presented in this chapter are summarized. Different wind fields were constructed and tested with respect to the impact of intermittency. Based on subdivided fully correlated grids an intermittency effect was evident until structure sizes in the order of $\frac{1}{2}R$, corresponding to the 4×4 case. In other words, the critical length scale of eddies for the intermittency effect is expected to be in the order of half a rotor radius. However the dynamics obtained from the subdivided fully correlated grids include strong periodicities due to the rotational sampling of the regularized wind field structures. This is not expected for real wind fields. For the results obtained with stationary coherent structures, immense scattering was observed. No clear conclusion with respect to the intermittency effect could be drawn. In huge part this scattering stems from the spatial dynamics, which seem to dominate the load dynamics compared to the temporal dynamics. In general it is known that wind velocity variations in the rotor plane is introduced, a dynamic known as 'rotational sampling' or 'eddy slicing' is introduced into the wind turbine dynamics. Depending on the field properties, this effect can be so dominant that the intermittency effect, documented in Chapter 4 was not detectable anymore. From this, it can be concluded that the intermittency effect in the fatigue loads (and more generally the impact of the temporal wind dynamics) strongly depend on other spatio-temporal wind field characteristics like the coherence.

Chapter 6

Conclusions

This thesis is about the incorporation of advanced statistical features of turbulence into wind models for wind energy applications. More precisely, it analyzes the impact of non-Gaussian distributed wind velocity increments, related to the concept of intermittent turbulence, on wind turbine fatigue loads.

The work contains two minor and two major achievements: A comprehensive literature review on this topic and related studies is given, which also points out strengths and weaknesses of these. It provides a suitable starting point and can be of assistance for future researchers, who are interested in a similar project. Secondly, the concept of isolating the statistics of interest is explicitly addressed and explained in this work, so that wind field requirements are more clear. In some previous studies this aspect has been overlooked. The key aspect of this work and a novelty in this field is the documentation of the fact that the consideration of intermittency in wind fields can alter the fatigue loading of wind turbines. This could be shown with industry-like calculation tools for generic, extremely coherent wind fields. Secondly, it was shown that this intermittency effect decreases with decreasing coherence in the wind field. This explains contradicting conclusions between related works: The intermittency effect is not filtered out of the load dynamics, however the load dynamics due to the rotational sampling of the wind variation in the rotor plane, has the potential to outweigh the intermittency effect, depending on spatial variability. This could be shown, when load responses to wind fields with lesser coherence were analyzed. Some of these findings have been published [64, 65].

Since an intermittency effect has been documented, one might consider implementing intermittency into wind models in the future. In doing so, wind models would be improved, since more knowledge would be incorporated into them and they would represent the wind dynamics even better. This in return might justify for a reduction of safety factors due to the decrease in uncertainty.

However, further research is necessary in order to reach these goals. This work might serve as a suitable starting point as follows: The wind fields of this work are generic and theoretical. Most notably they lack a realistic coherence model. The reason lies in the fact that coherence is typically achieved as correlation in Fourier space. Following this approach the very demanding requirements that were formulated for the time series of this work, could not be preserved. Thus, future projects might consider other ways to implement coherence into wind fields or alternative how to preserve intermittency within the common coherence modeling approach. In doing so, one might investigate if and how intermittency can be characterized in Fourier space. Since the spectrum alone does not capture intermittency, a formulation including both the spectrum and the phase information is probably required.

Other wind field features like shear or veer have been sporadically tested. The corresponding results do not contribute a new aspect, wherefore they are left out in this thesis for the sake of brevity. However, these may be taken into consideration in future approaches, too since such features are an integral part of a comprehensive representation of a wind field.

Lastly, this work only targets intermittency in the time domain. Future work might focus on properly implementing intermittency into both the temporal and spatial domain. Within the scope of this work this could not be achieved. Further, it is questionable whether the typical spatial resolution of the selected wind turbine simulation method is suitable to resolve intermittency in the spatial domain.

Bibliography

- [1] D. Kleinhans. *Stochastische Modellierung komplexer Systeme*. PhD thesis, Westfälische Wilhlems-Universität Münster, 2008.
- [2] A. N. Kolmogorov. A refinement of previous hypotheses concerning the local structure of turbulence in a viscous incompressible fluid at high reynolds number. *Dokl. Akad. Nauk SSSR*, 1962.
- [3] A. N. Kolmogorov. Dissipation of energy in the locally isotropic turbulence. *Dokl. Akad. Nauk SSSR*, 1941.
- [4] Website of German Wind Energy Association (Bundesverband Windenergie). <https://www.wind-energie.de/themen/zahlen-und-fakten/>, October 2018.
- [5] Website of International Renewable Energy Agency. www.irena.org/publications/2018/Jul/Renewable-Energy-Statistics-2018, January 2020.
- [6] International Electrotechnical Commission. International standard 61400: Wind turbines. Technical report, International Electrotechnical Commission, 2005.
- [7] T. von Kármán. On the statistical theory of turbulence. *Proceedings of the National Academy of Sciences of the United States of America*, 23(2):98–105, 02 1937.
- [8] J. C. Kaimal, J. C. Wyngaard, Y. Izumi, and O. R. Cote. Spectral characteristics of surface-layer turbulence. *Q.J.R. Meteorol. Soc.*, pages 563–598, 1972.
- [9] J. Mann. The spatial structure of neutral atmospheric surface-layer turbulence. *Journal of Fluid Mechanics*, pages 141–168, 1994.
- [10] W. Frost, B. H. Long, and R. E. Turner. Engineering handbook on the atmospheric environmental guidelines for use in wind turbine generator development. Technical Report NASA-TP-1359, M-267, NASA, 1978.
- [11] F. Böttcher, C. Renner, H.P. Waldl, and J. Peinke. On the statistics of wind gusts. *Boundary Layer Metereology*, 108:163–173, July 2003.
- [12] J. A. Dutton and J. Højstrup. A model for the probability structure of atmospheric turbulence. In Pacific northwest laboratory, editor, *Proceedings of the conference and workshop on wind energy characteristics and wind energy siting 1979*, June 1979.

- [13] F. Böttcher, C. Renner, H. P. Waldl, and J. Peinke. Problematik der Windböen. *DEWI Magazin*, 19:58–62, August 2001.
- [14] H. Hohlen and J. Liersch. Synchrone Meßkampagnen von Wind- und Windkraftanlagen-Daten am Standort FH Ostfriesland, Emden. *DEWI Magazin*, 12:66–74, February 1998.
- [15] B. Castaing, Y. Gagne, and E.J. Hopfinger. Velocity probability density functions of high reynolds number turbulence. *Physica D: Nonlinear Phenomena*, 46(2):177 – 200, 1990.
- [16] M. Wächter, H. Heißelmann, M. Hölling, M. Morales, P. Milan, T. Mücke, J. Peinke, N. Reinke, and P. Rinn. Wind energy and the turbulent nature of the atmospheric boundary layer. *Journal of Turbulence*, 13:N26, 2012.
- [17] P. Milan, M. Wächter, and J. Peinke. Turbulent character of wind energy. *Physical Review Letters*, 110, March 2013.
- [18] H. Hähne, J. Schottler, M. Wächter, J. Peinke, and O. Kamps. The footprint of atmospheric turbulence in power grid frequency measurements. *Europhysics Letters*, 121(3):30001, 2018.
- [19] D. Kleinhans, R. Friedrich, H. Gontier, and A. P. Schaffarczyk. Simulation of intermittent wind fields: A new approach. *Proceedings of DEWEK 2006*, 08 2008.
- [20] H. Gontier, A. P. Schaffarczyk, D. Kleinhans, and R. Friedrich. A comparison of fatigue loads of wind turbine resulting from a non-Gaussian turbulence model vs. standard ones. *Journal of Physics: Conference Series*, 2007.
- [21] T. Mücke, D. Kleinhans, and J. Peinke. Atmospheric turbulence and its influence on the alternating loads on wind turbines. *Wind Energy*, 14:301–316, 2011.
- [22] F. Körber, G. Besel, and H. Reinhold. Meßprogramm an der 3 MW-Windkraftanlage GROWIAN: Schlußbericht. Technical Report 03-E-4512-A, Große-Windenergieanlage-Bau- und Betriebsgesellschaft, Hamburg, 1988.
- [23] M. Matsuishi and T. Endo. Fatigue of metals subjected to varying stress. *Proc. Japan Society of Mechanical Engineers*, pages 37–40, 1968.
- [24] J. Berg, A. Natarajan, J. Mann, and G. Patton. Gaussian vs non-Gaussian turbulence: impact on wind turbine loads. *Wind Energy*, 2016.
- [25] J. Schottler, N. Reinke, A. Hölling, J. Whale, J. Peinke, and M. Hölling. On the impact of non-Gaussian wind statistics on wind turbines – an experimental approach. *Wind Energy Science*, 2(1):1–13, 2017.
- [26] P. Thomas, M. Wächter, A. Antoniou, and T. Jersch. InterWiLa Schlussbericht: Berechnung und Validierung von Lasten an Windenergieanlagen aufgrund intermittenter Windfelder. Technical Report 0325798A, 0325798B, 01158023, Fraunhofer IWES, 2018.
- [27] M. Nelkin. Universality and scaling in fully developed turbulence. *Advances in Physics*, 43(2):143–181, 1994.

- [28] S. B. Pope. *Turbulent Flows*. Cambridge University Press, 2000.
- [29] L. F. Richardson. *Weather Prediction by Numerical Process*. Cambridge University Press, 1922.
- [30] S. G. Saddoughi and S. V. Veeravalli. Local isotropy in turbulent boundary layers at high reynolds number. *Journal of Fluid Mechanics*, 268:333–372, 1994.
- [31] G. I. Taylor. The spectrum of turbulence. *Proceedings of the Royal Society of London. Series A - Mathematical and Physical Sciences*, 164(919):476–490, 1938.
- [32] F. Anselmet, Y. Gagne, E. J. Hopfinger, and R. A. Antonia. High-order velocity structure functions in turbulent shear flows. *Journal of Fluid Mechanics*, 140:63–89, 1984.
- [33] F. Chillà, J. Peinke, and B. Castaing. Multiplicative process in turbulent velocity statistics: A simplified analysis. *J. Phys. II France*, 6(4):455–460, 1996.
- [34] A. Morales, M. Wächter, and J. Peinke. Characterization of wind turbulence by higher-order statistics. *Wind Energy*, 2012.
- [35] Website of research platforms in the North Sea and Baltic Sea (germ. abr. FINO). <http://www.fino-offshore.de/de/>, August 2016.
- [36] B. Jonkman and K. Kilcher. TurbSim User’s Guide: Version 1.06.00. Technical report, National Renewable Energy Laboratory, Colorado, 2012.
- [37] D. C. Powell and J. R. Connell. Review of wind simulation methods for horizontal-axis wind turbine analysis. Technical Report PNL-5903, Pacific Northwest Laboratory, June 1986.
- [38] M. Shinozuka and C.-M. Jan. Digital simulation of random processes and its applications. *Journal of Sound and Vibration*, 25(1):111 – 128, 1972.
- [39] P. Veers. Three-dimensional wind simulation. Technical report, Sandia National Laboratories, 01 1988.
- [40] R. Kutner and J. Masoliver. The continuous time random walk, still trendy: fifty-year history, state of art and outlook. *The European Physical Journal B*, 90(3):50, 2017.
- [41] J. G. Schepers. *Engineering models in wind energy aerodynamics*. PhD thesis, Technische Universiteit Delft, 2012.
- [42] J. N. Sørensen. Blade-element/momentum theory. In *General Momentum Theory for Horizontal Axis Wind Turbines*, volume 4, pages 99–121. Springer, 2016.
- [43] H. Glauert. *Airplane Propellers*. Springer, Berlin, Heidelberg, 1935.
- [44] Z. Du and M. S. Selig. The effect of rotation on the boundary layer of a wind turbine blade. *Renewable Energy*, 20(2):167 – 181, 2000.

- [45] D. Pitt and D. Peters. Theoretical Prediction of Dynamic Inflow Derivatives. *Vertica*, 5:21–34, 1981.
- [46] H. Rahimi, A. Martinez Garcia, B. Stoevesandt, J. Peinke, and G. Schepers. An engineering model for wind turbines under yawed conditions derived from high fidelity models. *Wind Energy*, 2018.
- [47] J. G. Leishman and T. S. Beddoes. A Semi-Empirical Model for Dynamic Stall. *Journal of the American Helicopter Society*, 34:3–17, 1989.
- [48] A. Björck. *Dynamic Stall and Three-dimensional Effects: Final Report for the EC DGXII Joule II Project JOU2-CT93-0345*. FFA TN.: Flygtekniska Försöksanstalten. Flygtekniska Försöksanstalten, 1996.
- [49] H. Madsen, N. Sørensen, C. Bak, N. Troldborg, and G. Pirrung. Measured aerodynamic forces on a full scale 2MW turbine in comparison with EllipSys3D and HAWC2 simulations. *Journal of Physics: Conference Series*, 1037(2):022011, 2018.
- [50] J. Jonkman and M. L. Buhl. FAST User’s Guide. Technical Report EL-500-38230, National Renewable Energy Laboratory, Colorado, August 2005.
- [51] B. Jonkman and J. Jonkman. Fast v8.16.00a-bjj. Technical report, NREL, 2016.
- [52] J. Jonkman, G. J. Hayman, B. Jonkman, and R.R. Damian. AeroDyn v15 User’s Guide and Theory Manual (draft version). Technical report, NREL, July 2016.
- [53] J. Jonkman, S. Butterfield, W. Musial, and G. Scott. Definition of a 5-MW reference wind turbine for offshore system development. Technical Report TP-500-38060, National Renewable Energy Laboratory, 15013 Denver W Pkwy, Golden, CO 80401, USA, February 2009.
- [54] L. A. Viterna and R. D. Corrigan. Fixed pitch rotor performance of large horizontal axis wind turbines. Technical report, NASA Lewis Research Center, 1982.
- [55] P. J. Moriarty and A. C. Hansen. AeroDyn Theory Manual. Technical Report NREL/TP-500-36881, National Renewable Energy Laboratory, 2005.
- [56] American Society for Metals. *Case histories in failure analysis*. Metals Park, Ohio: American Society for Metals, 1979.
- [57] M. A. Miner. Cumulative damage in fatigue. *Journal of Applied Mechanics*, pages A159–A164, 1945.
- [58] P. H. Madsen, J. W. M. Dekker, S. E. Thor, K. McAnulty, H. Matthies, and R. W. Thresher. Expert Group Study on Recommended Practices for Wind Turbine Testing and Evaluation, 3. Fatigue Loads. Technical report, Submitted to the Executive Committee of the International Energy Agency Programme, 1990.

- [59] S. Lück, J. Peinke, and R. Friedrich. Uniform statistical description of the transition between near and far field turbulence in a wake flow. *Physical Review Letters*, 83:5495–5498, 12 1999.
- [60] K. Träumner, Th. Damian, Ch. Stawiarski, and A. Wieser. Turbulent structures and coherence in the atmospheric surface layer. *Boundary-Layer Meteorology*, 154(1):1–25, Jan 2015.
- [61] G. Matheron. Principles of geostatistics. *Economic Geology*, 58:1246–1266, 1963.
- [62] R. Damiani and G. Hayman. The dynamic stall module for fast 8. Technical report, National Renewable Energy Laboratory, April 2016.
- [63] A. Gonzáles. DYSTOOL Stability Aerodynamic Tool for 2D Airfoil Based on the Beddoes-Leishman Model. Technical Report IN-523/069-en, Centro Nacional de Energías Renovables, 2014.
- [64] C. M. Schwarz, S. Ehrich, R. Martín, and J. Peinke. Fatigue load estimations of intermittent wind dynamics based on a blade element momentum method. *Journal of Physics: Conference Series*, 1037, 2018.
- [65] C. M. Schwarz, S. Ehrich, and J. Peinke. Wind turbine load dynamics in the context of turbulence intermittency. *Wind Energy Science*, 4:581–594, 2019.

List of publications

Peer-reviewed publications

- C. M. SCHWARZ, S. EHRICH, J. PEINKE: Wind turbine load dynamics in the context of turbulence intermittency, *Wind Energy Science*, 2019
- S. EHRICH, C. M. SCHWARZ, H. RAHIMI, B. STOEVE SANDT, J. PEINKE: Investigation of the validity of the Blade Element Momentum Theory for wind turbine simulations in turbulent inflow by means of Computational Fluid Dynamics, *Journal of Physics: Conference Series*, 2018
- C. M. SCHWARZ, S. EHRICH, R. MARTÍN, J. PEINKE: Fatigue load estimations of intermittent wind dynamics based on a Blade Element Momentum method, *The Science of Making Torque from Wind*, Milano, Italy, 2018
- O. CEYHAN, O. PIRES, X. MUNDUATE, N. SORENSEN, T. REICHSTEIN, A. P. SCHAF-FARCZYK, K. DIAKAKIS, G. PAPADIKIS, E. DANIELE, C. M. SCHWARZ, T. LUTZ, R. PRIETO: Summary of the Blind Test Campaign to predict the High Reynolds number performance of DU00-W-210 airfoil, *AIAA SciTech*, Grapevine, Texas (US), 2017

Further Conferences Contributions

- C. M. SCHWARZ, S. EHRICH, J. PEINKE: Super-Gaussian wind velocity increments and their impact on fatigue loads, *Wind Energy Science Conference*, Copenhagen, Denmark, 2017
- C. M. SCHWARZ, B. STOEVE SANDT, J. PEINKE: Hybrid aerodynamic analysis of wind turbines, *Proceedings of 10th PhD Seminar on Wind Energy in Europe*, Orleans, France, 2014.

Additional publications

- C. M. SCHWARZ, S. EHRICH, P. THOMAS: Turbulence Intermittency (AVATAR Report D4.7), 2016.
- C. M. SCHWARZ, M. APARICIO-SANCHEZ, D. ASTRAIN JUANGARCIA, A. GONZALEZ-SALCEDEO, N. RAMOS-GARCIA, M. SESSAREGO, N. SORENSEN, M. SCHRAMM, P. THOMAS, P. CHASAPOGIANNIS, T. CHAVIAROPOULOS, M. MANOLEOS, G. SIEROS: Effect of blade solidity and thickness on performance and loads (AVATAR Report D4.10), 2017.
- J. HEINZ, N. SORENSEN, V. RIZIOTIS, C. M. SCHWARZ, S. GOMEZ IRADI, M. STETTNER: Aerodynamics of large rotors (AVATAR Report D4.5), 2016.
- P. CHASAPOGIANNIS, A. GONZÁLEZ, A. IRISARRI, H. MADSEN, T. J. LARSEN, K. BOORSMA, C. M. SCHWARZ, M. REIJERKERK, D. MANOLAS: Comparison of models with respect to Load analysis in extreme yaw of the INNWIND.EU and AVATAR RWT's (AVATAR Report D4.3), 2016.

Acknowledgements

Firstly I want to thank Prof. Joachim Peinke for accepting me as his PhD student for his help, for pushing me and for making all of this possible. Thank you! I would like to thank Prof. Laura Lukassen accepting for being an examiner of this work. It is highly appreciated. To Prof. Ivàn Herraéz, thank you as well for helping me with my project since the very first days and now ironically again towards the end. I would also like to thank to Prof. Schaffarczyk who had a big influence on my studying career. Thanks to the entire international research community of wind energy, especially the AVATAR people. The research on wind energy is in good hands.

Thanks to all the people that made everything around us work: Agnes, Frauke, Dagmar, Irene, Elke and Stephan. Thanks to the experimental co-workers Jannik, Nico, Gerrit mit seiner Prokatnase, Mike, Hendrik, the o-founder of WP7, Lars Krögermann and Stani. Thanks to the stochastic co-workers Phillip, Hauke, Christian, David and Matthias. Thanks to my simulation people Wided, Carlos, Bernhard, Elia, Jonas, Matthias, Cherif and Hassan. Thank you Lena ‘Commanderin’ Vorspel for the good vibes in the office and for organizing everything around me and all of us and for helping me to set up the printer every single time. Leo, thank you for the invention of the Zwischenwasser. Thank you Emma for warming my feet and entering and leaving the office so excited everyday. May you rest in peace with your head placed on a nice bag and with an endless supply of cucumbers. Thanks to Hamid Rahimi for the elevator meetings, for pointing out the importance of integration and the equality of 61 and 62 – after all, it could be worse. Special thanks to you, Basti ‘Dose’ Dose. Without you I would not have ended up in Oldenburg. Thanks for your friendship and all the good memories including coming from upstairs. A very special and enormous ‘thank you’ goes to Sebastian ‘Officer’ Ehrich. This work is a result of both of our efforts. While both of us would have liked to achieve even more, I think we gave it our best. I will never forget your ergonomic sitting posture and what Tschebyscheff said.

Thanks to the game of basketball for all it has done for me. Also, it goes without saying that I would have not achieved this without the support of my mother, father, my sister and my friends Basti and Jonas. Thank you for being there. Last but not least: Kheli mam’noon, jooni. Dooset daram.

Finally, to whom it may concern: I learned a lot about life, relationships and myself while doing this PhD project. I could easily write another thesis about it, but this is not the place. If I had to boil it down to a minimum I would tell you:

Anything can be learned.

Curriculum vitae

Personal information:

Name Carl Michael Schwarz
Birthday November 18th, 1987
Place of birth Kiel, Germany
Citizenship German

Education:

since 04/2014 PhD Student of Prof. Dr. Joachim Peinke
AG TWiSt (Turbulence, Wind energy and Stochastics)
University of Oldenburg

09/2011 – 03/2014 M.Sc. Wind Engineering, FH Kiel

09/2008 – 07/2011 B.Eng. Mechanical Engineering, FH Kiel

Professional experience:

11/2018 – 02/2020 Development Engineer, Enercon, Aurich, Germany

04/2014 – 08/2018 Research Fellow, ForWind, Institute of Physics, C.v.O. University of Oldenburg

03/2013 – 01/2014 Research Assistant, Fraunhofer IWES, Germany

Erklärung

Ich erkläre hiermit, dass

- (a) eine Promotion zum Dr.-Ing. angestrebt wird,
- (b) ich diese Arbeit selbständig verfasst und nur die angegebenen Hilfsmittel benutzt habe, und dass die Arbeit in Teilen bereits veröffentlicht bzw. zur Veröffentlichung eingereicht wurde,
- (c) diese Dissertation weder in ihrer Gesamtheit noch in Teilen einer anderen Hochschule zur Begutachtung in einem Promotionsverfahren vorgelegen hat.

July 2, 2020, Oldenburg

.....
(Name)

